Fermilab Library
0 1160 0020068 7

E-760

UNIVERSITY OF CALIFORNIA

IRVINE

Study of the χ_1 and χ_2 States Produced in $\bar{p}p$ Annihilations in Fermilab Experiment 760

DISSERTATION

submitted in partial satisfaction of the requirements for the degree of

DOCTOR OF PHILOSOPHY

in Physics

by

Jose Laurencio Marques

Dissertation Committee:

Professor Mark A. Mandelkern, Chair

Professor Jonas Schultz

Professor Herbert Hamber

1992

FERMI
LIBOFFCE
THESIS

© 1992 by Jose Laurencio Marques

All rights reserved.

The dissertation of Jose Laurencio Marques is
approved, and is acceptable in quality
and form for publication on microfilm:

Committee Chair

University of California, Irvine

1992

AAL 5049

To

my skeptical father,

my wonderful mother,

and

my loving wife.

Contents

List of Figures vii

List of Tables x

Acknowledgements xii

Curriculum Vitae xiii

Abstract of the Dissertation xv

Introduction 1

1 Background and Motivation 4
- 1.1 Previous Experiments . . . 4
  - 1.1.1 Crystal Ball . . . 4
  - 1.1.2 R704 . . . 6
- 1.2 Experimental Methods in E760 . . . 9
- 1.3 Nonrelativistic Potential Models . . . 10
  - 1.3.1 Relativistic Effects . . . 13
- 1.4 The $\chi_{1,2}$ Radiative Decays . . . 15
  - 1.4.1 The Helicity and Multipole Amplitudes . . . 16

2 The E760 Apparatus 24
- 2.1 The $\bar{p}$ Source . . . 24
  - 2.1.1 $\bar{p}$ Production and Deceleration . . . 27
  - 2.1.2 $\bar{p}$ Energy Measurement . . . 28
- 2.2 The H_2 gas jet target . . . 34
- 2.3 The Luminosity Monitor . . . 34
- 2.4 The E760 Detector . . . 38
  - 2.4.1 Hodoscopes H1 and H2 . . . 39
  - 2.4.2 The Čerenkov . . . 41
  - 2.4.3 The Forward Calorimeter . . . 44

3 The Central Calorimeter 46
- 3.1 Design and Construction . . . 46
  - 3.1.1 Construction . . . 54
- 3.2 Initial Testing and Calibration . . . 59

3.2.1 Photomultiplier Tube Gain Curves 59
3.2.2 Initial Calibration with Muons 60
3.3 *In Situ* Calibration 65
3.4 Gain Monitoring System 67
3.5 Clusterization and Resolution 74
3.6 CCAL Logic and Timing Information 77

4 The Trigger and Data Aquisition 84
4.1 The Hardware Triggers 84
4.1.1 The Level 2 Triggers 87
4.1.2 MLU1 - The Charged Trigger 87
4.1.3 MLU4 - The Neutral Trigger 88
4.2 The Overall Charged Trigger Efficiency 89
4.2.1 Cracks in H1 and H2 89
4.2.2 Hodoscope Multiplicity 91
4.2.3 The PBG1 and COPL Requirements 93
4.2.4 The Čerenkov Septum 94
4.2.5 Efficiencies of the Various Subtriggers 97
4.3 The Level 3 "ACP" Trigger 99
4.3.1 Data Readout Hardware 100

5 The $\chi_{1,2}$ Angular Distributions 103
5.1 Selection of the Sample 104
5.1.1 Estimate of Background Contamination 106
5.2 Likelihood Fit to the Data 107
5.2.1 Čerenkov Correction 115
5.2.2 The Acceptance Constants 117
5.3 Results and Goodness of Fits 118

6 Resonance Parameters for the χ_1 and χ_2 127
6.1 Event Selection 127
6.1.1 Selection Efficiency 130
6.1.2 Estimate of Backgrounds 133
6.1.3 Acceptance 136
6.2 Fitting the Excitation Curves 136
6.3 Results and Goodness of Fits 137

7 Conclusions 143
7.1 Branching Ratios and Partial Widths 143
7.1.1 Branching Ratio to $\bar{p}p$ 144
7.1.2 Radiative Widths 145
7.2 Production Helicities 147
7.3 Multipole Amplitudes 148
7.3.1 The Charm Quark Magnetic Moment 150
7.4 Hadronic Widths 151

7.4.1 Determination of α_s 152
7.5 Final Comments 153

Bibliography **155**

List of Figures

.1 Charmonium spectrum below the $D\bar{D}$ threshold. 3

1.1 The Crystal Ball Detector. 5
1.2 The Crystal Ball ψ' inclusive photon spectrum. 6
1.3 The R704 experimental apparatus. 7
1.4 The angular definitions for $\bar{p}p \rightarrow \chi_{1,2} \rightarrow J/\psi + \gamma \rightarrow e^+e^- + \gamma$. 17

2.1 The Fermi National Laboratory accelerator complex. 25
2.2 The $\bar{p}$ Source. 26
2.3 A typical beam frequency spectrum. 31
2.4 Schematic of the gas jet target. 35
2.5 Schematic of the luminosity monitor. 36
2.6 A typical luminosity monitor pulse height spectrum. 37
2.7 The E760 detector. 40
2.8 H2 pulse height in normalized mip units for electrons from J/ψ decays. 42
2.9 Schematic of the Čerenkov. 43
2.10 Beam view of the 144 module forward calorimeter. 45
2.11 Schematic of a forward calorimeter module. 45

3.1 Mean pulse height distributions for the five lead glasses tested at UINPL. 49
3.2 The CCAL showing the θ segmentation. 52
3.3 The CCAL showing the ϕ segmentation. 52
3.4 Base diagram for the 2.5 and 3.0 *in* PMTs. 55
3.5 A cut-out view of a wedge. 57
3.6 Diagram of the calorimeter and its support structure. 58
3.7 Diagram of the μ testing apparatus. 63
3.8 A typical spectrum from cosmic ray μs. 64
3.9 Diagram of the gain monitoring system. 68
3.10 Flashlamp spectrum as seen by a PMT in the CCAL 70
3.11 ^{207}Bi pulser spectrum as seen by one of the monitor tubes. 71
3.12 Flashlamp pulse height spectrum as seen by one of the monitor tubes. 71
3.13 Comparison of the calibration with and without the gain monitor. . . 73
3.14 Difference between θ_{lab} as determined by the CCAL and that determined by the charged tracking for a sample of J/ψ events. 78

3.15 Difference between ϕ_{lab} as determined by the CCAL and that determined by the charged tracking for a sample of J/ψ events. 79
3.16 Average calorimeter energy resolution. 80
3.17 Monte Carlo simulation for the reaction $\bar{p}p \rightarrow J/\psi \rightarrow e^+e^-$. 81

4.1 Coincidence between H1, H2, and the Čerenkov required to form the charged track tags *h and e*. 86
4.2 The efficiency of hadron tag for 1991 data set. 91
4.3 Distribution of electrons from J/ψ decays. 95
4.4 Čerenkov efficiency as a function $\cos(\theta_{cm})$ from a 1991 sample of J/ψ events. 96
4.5 Schematic of the E760 read out system. 102

5.1 Results of 300 Monte Carlo experiments for the χ_1 angular distribution where the input value was $a_2 = -0.14$. 110
5.2 Results of 300 Monte Carlo experiments for the χ_2 angular distribution where the input values for the parameters were $a_2 = -0.15$, $a_3 = 0.0$, and $B_0^2 = 0.02$. 111
5.3 ln(L) plot for a fit to a Monte Carlo simulation of the χ_1, no acceptance restrictions were imposed and $a_2 = -0.14$. 112
5.4 ln(L) plot for a fit to a Monte Carlo simulation of the χ_1 where the acceptance for electrons was restricted to $15° < \theta_{lab} < 60°$ and $a_2 = -0.14$. 112
5.5 Contour plots of ln(L) for a fit to a Monte Carlo simulation of the χ_2, no acceptance restrictions were imposed and $B_0^2 = 0.02$, $a_2 = -0.14$, $a_3 = 0.0$. 113
5.6 Contour plots of ln(L) for a fit to a Monte Carlo simulation of the χ_2 where the acceptance for electrons was restricted to $15° < \theta_{lab} < 60°$ and $B_0^2 = 0.02$, $a_2 = -0.14$, $a_3 = 0.0$. 114
5.7 Detection efficiency as a function of θ_{lab} for electrons in the Čerenkov. 117
5.8 Comparison of the 1990 χ_1 data with the theoretical angular distribution function. 121
5.9 Comparison of the 1990 χ_2 data with the theoretical angular distribution function. 122
5.10 Comparison of the 1991 χ_2 data with the theoretical angular distribution function. 123
5.11 ln(L) plot for the fit to the 1990 χ_1 angular distribution. 124
5.12 Contour plots of ln(L) from the fit to the 1990 χ_2 angular distribution. 125
5.13 Contour plots of ln(L) from the fit to the 1991 χ_2 angular distribution. 126

6.1 Plot of confidence level from the kinematic fit for the $\chi_{1,2}$ events in the final event sample. 130
6.2 The shaded histogram shows the cluster mass for a clean sample of electron showers, the unshaded histogram shows the cluster mass for a sample of π^0 events. 131

6.3 1990 $\chi_{1,2}$ sample after selection with kinematic fit, the open area is the data while the shaded area is the luminosity scaled background. . 134
6.4 1990 $\chi_{1,2}$ sample after selection with π^0 cuts, the open area is the data while the shaded area is the luminosity scaled background. . . . 134
6.5 1990 $\chi_{1,2}$ sample after selection with J/ψ invariant mass cut, the open area is the data while the shaded area is the luminosity scaled background. 135
6.6 1990 clean J/ψ sample, shown for comparison. 135
6.7 Measusured cross section for the χ_1. 141
6.8 Measusured cross section for the χ_2. 142

List of Tables

1.1 Previous results for the χ_1. 7
1.2 Previous results for the χ_2. 8
1.3 Angular distribution functions for χ_2. 21
1.4 Angular distribution functions for χ_1. 23

2.1 Charmonium states and the corresponding $\bar{p}$ beam energy threshold for resonant $\bar{p}p$ production. 29
2.2 η as measured by three methods in 1990. 33

3.1 Characteristics of the lead glass used in the E760 central calorimeter, Schott F2 lead glass. 50
3.2 Dimensions and positions of the lead glass blocks in a wedge. 51
3.3 Characteristics of the Hamamatsu photomultiplier tubes used in the E760 central calorimeter. 53
3.4 $\frac{\mu}{e^-}$ as determined at BNL. 62
3.5 Values of clustering algorithms empirically determined constants. . . 76

4.1 Efficiencies for $(\#H2 = 2) \otimes (\#H1 = 2)$ requirements for the $1\check{C}$ trigger. 92
4.2 Efficiencies for $(\#H2 = 2) \otimes (\#H1 = 2) \otimes (\overline{FCHOR})$ requirements for the $0\check{C}$ trigger. 92
4.3 Occupancy of the hodoscope H1 and H2 93
4.4 Efficiency of the COPL requirement. 94
4.5 Efficiencies for the various charged level 2 triggers averaged over all angles. 98

5.1 Number of events in the final sample of $\chi_{1,2}$ events used to fit the angular distributions. 106
5.2 Number of events in the background sample taken off resonance. . . . 107
5.3 Background estimate for the angular distribution samples. 107
5.4 Efficiency for detection of electrons for $\chi_{1,2}$ decays as a function of θ_{lab} using both the $1\check{C}$ and $2\check{C}$ triggers. 116
5.5 Acceptance constants for the $\chi_{1,2}$. 118
5.6 Results of the angular distribution fits. 119
5.7 The error matrix for the angular distribution fits. 120

6.1 Events and luminosity for the final sample used to fit for resonance parameters. 130

6.2 Events used to determine the selection efficiency. 132
6.3 Estimate of background contamination. 133
6.4 Summary of the data used to fit the χ_1 resonance. 138
6.5 Summary of the data used to fit the χ_2 resonance. 139
6.6 Results of the fits to the resonance curves for the $\chi_{1,2}$ 140
6.7 The error matrix for the fits to the resonance curves. 141
6.8 Final results for $\chi_{1,2}$ resonance parameters. 142

7.1 Calulated branching ratios and partial widths for the $\chi_{1,2}$ 144
7.2 Comparison of predicted and measured $BR(\chi_{1,2} \rightarrow \bar{p}p)$ in units of 10^{-4}. 145
7.3 $\chi_{1,2}$ E1 transition rates calculated from Cornell Model. 147
7.4 Comparison between measured and predicted multipole amplitudes. . 149
7.5 Comparison between measured and predicted hadronic widths for the $\chi_{1,2}$. 152

Acknowledgements

I am most grateful to Professors Mark A. Mandelkern and Jonas Schultz not only for their counsel and guidance throughout my graduate career but also for their unwavering confidence in me. I would also like to thank Dr. Alan Hahn for his encouragement and guidance early in my career.

I am grateful the Dr. Petros Rapidis and Dr. Stephen Pordes for their seemingly never ending concern for the plight of graduate students at Fermilab. They also deserve a great deal credit for the success of E760. Without their enormous efforts during the design and construction phase, E760 may never have happened. Dr. Petros Rapidis deserves a special thanks for his gargantuan efforts in the commissioning and maintenance of the gas target system. I would also like to thank Dr. Michael Church not only for his efforts in creating a data aquisition system and for providing the best $\bar{p}$ beam in the world, but also for the motivation that his untiring efforts provided. Also deserving special mention are Dr. Flavio Marchetto and Dr. Augusto Ceccucci for their tremendous contributions to the preparation and execution of E760 as well as their contributions to the development of the offline code and eventual analysis of data.

A very special thanks must be given to Professor Rosanna Cester of the University of Turin. As spokesperson, she is easily the hardest working person in the E760 collaboration. Without her patient guidance we would have certainly been lost.

My thanks go to all the members of the E760 collaboration who are too numerous to mention here but without which, this work could not have happened. A further thanks must go to all the graduate students and the post doctoral researchers that worked so hard to make E760 a success. A special mention must go to Dr. James E. Fast and Dr. Giorgos Zioulas not only for their help but also for their friendship.

I am grateful to all the technical and support staff from Fermilab that made E760 possible.

Lastly and most importantly, I would like to thank my loving wife for her unending concern and support.

This work was funded by the US Department of Energy under grant DE-FG03-91ER40679 task B.

Curriculum Vitae

1987	B.S. in Physics, University of California, Irvine
1987–1990	Research Assistant, Department of Physics, University of California, Irvine
1990	M.S. in Physics, University of California, Irvine
1990–1992	Research Assistant, Department of Physics, University of California, Irvine
1992	Teaching Assistant, Department of Physics, University of California, Irvine
1992	Ph.D. Physics, University of California, Irvine Dissertation: *Study of the χ_1 and χ_2 States Produced in $\bar{p}p$ Annihilations in Fermilab Experiment 760.* Professor Mark A. Mandelkern, Chair

Publications

L. Bartoszek et al., The E-760 Lead-glass Central Calorimeter: Design and Initial Test Results, Nucl. Instr. and Meth. **A301** (1991) 47-60.

T.A. Armstrong et al., Study of the χ_1 and χ_2 Charmonium states Formed in $\bar{p}p$ Annihilations, Nucl. Phys. **B373** (1992) 35.

T.A. Armstrong et al., Precision Measurements of Charmonium States Formed in $\bar{p}p$ Annihilation, Phys. Rev. Lett. **68** (1992) 1468-1471.

E-760 Collaboration, Observation of the $^1P_1$ State of Charmonium, submitted to Phys. Rev. Lett., Fermilab-Pub-92/186-E.

E-760 Collaboration, Observation of a 1515 MeV $2\pi^0$ Meson in Antiproton-Proton Annihilation at $\sqrt{s} = 2980$ and 3097 MeV, submitted to Phys. Rev. Lett.

E-760 Collaboration, Measurement of the $\gamma\gamma$ Partial Width of the χ_2 Charmonium Resonance, Phys. Rev. Lett., to be submitted.

E-760 Collaboration, Measurement of the J/ψ and ψ' Resonance Parameters in $\bar{p}p$ Annihilation, Phys. Rev., to be submitted.

E-760 Collaboration, Measurement of Proton Electromagnetic Form Factors for Time-like High Momentum Transfer, Phys. Rev. Lett., to be submitted.

E-760 Collaboration, Two Photon Decays of the $^1s_0$ Charmonium Resonances Formed in $\bar{p}p$ Annihilations, Phys. Rev. D, to be submitted.

E-760 Collaboration, Measurement of the Angular Distributions from the Radiative Decay of the χ_2 State of Charmonium Formed in $\bar{p}p$ Annihilations, Phys. Rev. D, to be submitted.

Abstract of the Dissertation

Study of the χ_1 and χ_2 States Produced in $\bar{p}p$ Annihilations in Fermilab Experiment 760

by

Jose Laurencio Marques

Doctor of Philosophy in Physics

University of California, Irvine, 1992

Professor Mark A. Mandelkern, Chair

A study of the $\chi_1(^3P_1)$ and the $\chi_2(^3P_2)$ states of charmonium formed in antiproton-proton annihilations is reported in this dissertation. Performed at Fermi National Accelerator Laboratory, Experiment 760 used an internal molecular hydrogen jet target and circulating beam of momentum cooled antiprotons to conduct energy scans of the two resonances. The small momentum spread of the antiproton beam allowed very precise measurements of both the resonance mass and total width to be made.

From a sample of 483 χ_1 and 556 χ_2 events the following resonance parameters have been determined: $\Gamma_{\chi_1} = (0.86 \pm 0.14)\ MeV$, $\Gamma_{\chi_2} = (2.01 \pm 0.18)\ MeV$, $M_{\chi_1} = (3510.51 \pm 0.13)\ MeV/c^2$, $M_{\chi_2} = (3556.03 \pm 0.14)\ MeV/c^2$, $\Gamma(\chi_1 \rightarrow \bar{p}p) \times BR(\chi_1 \rightarrow J/\psi\gamma) \times BR(J/\psi \rightarrow e^+e^-) = (1.22 \pm 0.15)\ eV$, and $\Gamma(\chi_2 \rightarrow \bar{p}p) \times BR(\chi_2 \rightarrow J/\psi\gamma) \times BR(J/\psi \rightarrow e^+e^-) = (1.68 \pm 0.16)\ eV$.

The angular distribution for the reaction $\chi_{1,2} \rightarrow J/\psi + \gamma \rightarrow e^+e^- + \gamma$ was also studied. For the χ_1 resonance, from a sample of 360 events, the radiative decay quadupole amplitude has been found to be $a_2 = -0.14 \pm 0.06$. For the χ_2, from a sample of 1904 events, the radiative decay quadrupole and octupole amplitudes have been found to be $a_2 = -0.15 \pm 0.07$ and $a_3 = 0.00 \pm 0.05$ respectively. The contribution from helicity zero in the formation process of the χ_2 has also been measured, $B_0^2 = 0.02^{+0.13}_{-0.02}$.

Introduction

On Monday, the 11th of November 1974, the simultaneous discovery of the J/ψ by groups at Stanford Linear Accelerator Center (SLAC) and Brookhaven National Laboratory (BNL) ushered in what has become known as the "November Revolution." The Brookhaven group, headed by S.C.C. Ting, studied the reaction $p + Be \rightarrow e^+e^- + X$ using the Brookhaven AGS. The Brookhaven group observed a large number of e^+e^- events at a mass of $\sim$ 3.1 GeV/c^2 which they ascribed to the production and decay of a new vector meson called the "J." Meanwhile at SLAC, the Stanford-LBL group headed by B. Richter, was looking at roughly the inverse process where electron and positrons annihilated to form hadrons. As the Stanford-LBL group tuned the SPEAR center-of-mass energy through 3.1 GeV, they observed a $\sim$ 2000 fold increase in the cross section for $e^+e^- \rightarrow$ ***hadrons***. The 3.1 GeV meson discovered at SPEAR was named the "ψ." We now know that the two groups had both discovered the same narrow resonance dubbed the J/ψ.

Two weeks after the initial discovery of the ψ, the SPEAR group discovered a second narrow resonance, the ψ', at $\sim$ 3.7 GeV. In the months that followed it became apparent that these new particles were probably the manifestations of a new quark flavor. Charm had been proposed in 1970 by Glashow, Maiani, and Iliopoulos to explain the absence of strangeness changing weak neutral currents.

When the D meson was discovered and found to have the properties predicted by the charm model, the ψ and ψ' could be confidently identified as excitations of a bound charm-anticharm quark pair. It was immediately realized that the $c\bar{c}$ system, dubbed charmonium in analogy with positronium, would provide a fertile testing ground for the theory of strong interactions.

Due to the relatively large mass of the charm quark ($\sim 1.5\ GeV/c^2$), its motion within a charmonium state could be treated nonrelativistically. This allowed one to use the apparatus of potential models to predict the masses of the other charmonium resonances. Early models used simple Coulomb-like potentials while later models attempted to include quark confining terms. As more charmonium states were discovered the phenomenological, models were refined further.

In the 18 years since the discovery of the J/ψ, a great deal has been learned about charmonium and the strong interaction that describes it. Figure .1 shows the charmonium spectrum below the $D\bar{D}$ threshold. Although six of the eight predicted resonances had been observed before E760 was conceived, precise measurements these resonances (which serve to constrain QCD) were lacking. E760 has been designed to conduct a high precision study of all the lowlying charmonium resonances.

This dissertation describes in detail the study of the $\chi_1(^3P_1)$ and the $\chi_2(^3P_2)$ states of charmonium as observed through the reaction $\bar{p}p \rightarrow \chi_{1,2} \rightarrow J/\psi + \gamma \rightarrow e^+e^- + \gamma$. Precise measurements of the resonance masses and widths are reported, as well as a study of the angular distributions.

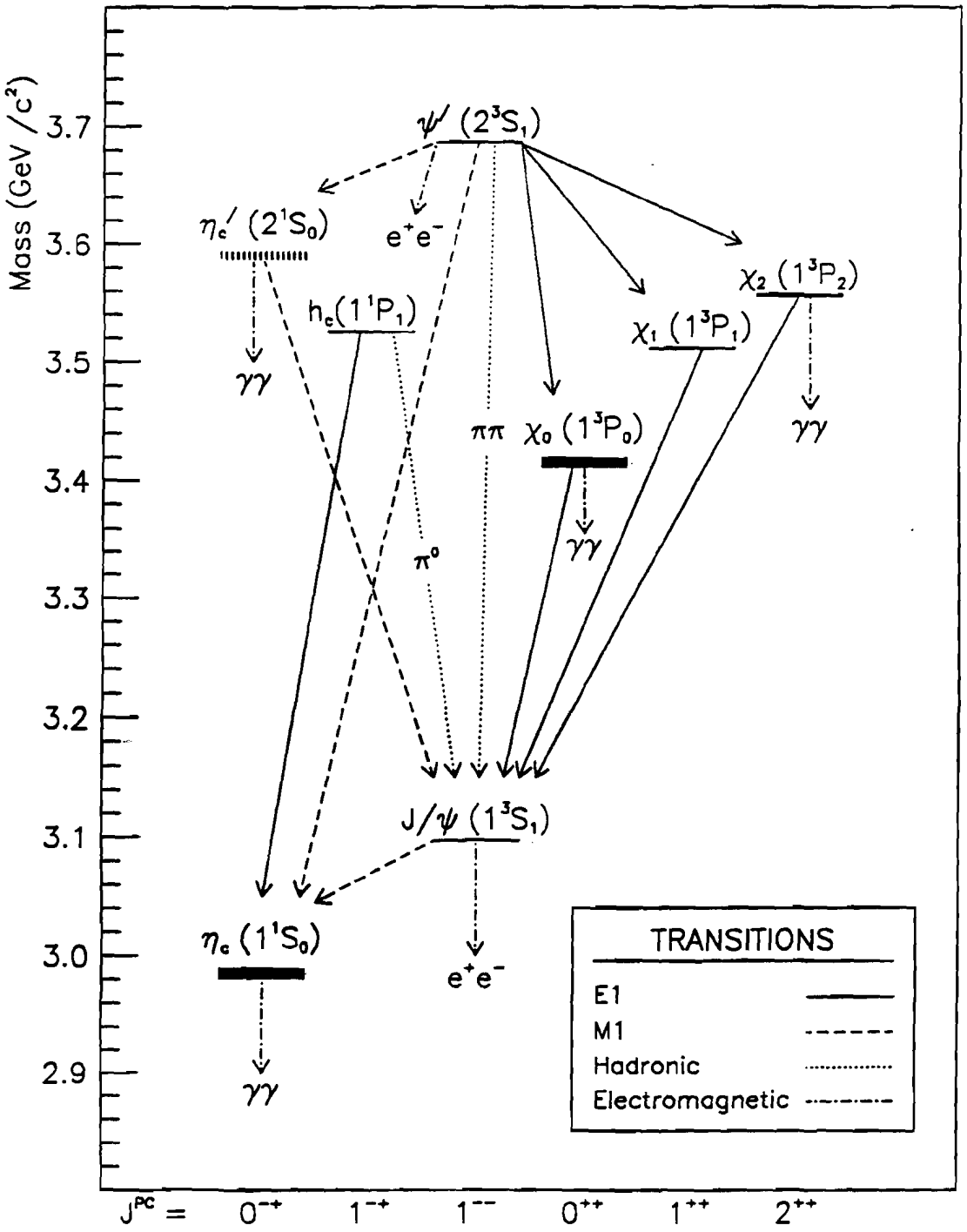

Figure .1: Charmonium spectrum below the $D\bar{D}$ threshold.

Chapter 1

Background and Motivation

1.1 Previous Experiments

Since 1974 there have been many experiments to study the charmonium spectrum and the decay channels of specific states. Most of the data on charmonium comes from e^+e^- annihilations to form the the $J^{PC} = 1^{--}$ resonances (J/ψ and ψ') which then undergo radiative transitions to the lower lying states. The $\chi_{0,1,2}$ were first observed by this method. Some contributions have been made with experiments that collide high energy protons with a variety of target materials. A fairly recent advance has been made with the advent of cooled antiproton beams. Experiment R704 at CERN pioneered a technique whereby antiprotons are brought into collision with a hydrogen jet target, allowing the direct production of all the charmonium resonances regardless of J^{PC}.

1.1.1 Crystal Ball

The Crystal Ball [1] experiment is a good recent example (of the e^+e^- annihilation type) of a charmonium experiment with particular relevance to the material

presented in this dissertation. The Crystal Ball apparatus shown in figure 1.1 is a large solid angle, high resolution, non-magnetic detector located at SPEAR. The key idea behind Crystal Ball was to make high resolution measurements of the radiative photons produced in the double transition $\psi' \rightarrow \chi_{0,1,2} + \gamma \rightarrow J/\psi + \gamma + \gamma$. If one looks at the inclusive ψ' photon spectrum (see figure 1.2), observed at Crystal Ball, the χ states are quite prominent. Figure 1.2 highlights the biggest difficulty with experiments like Crystal Ball. Since the detector resolution is about 5 MeV and the $\chi_{1,2}$ have line widths in the $1-2$ MeV range, direct measurements of the resonance width are difficult. The results of Crystal Ball's study of the $\chi_{1,2}$ resonances are summarized in tables 1.1 and 1.2.

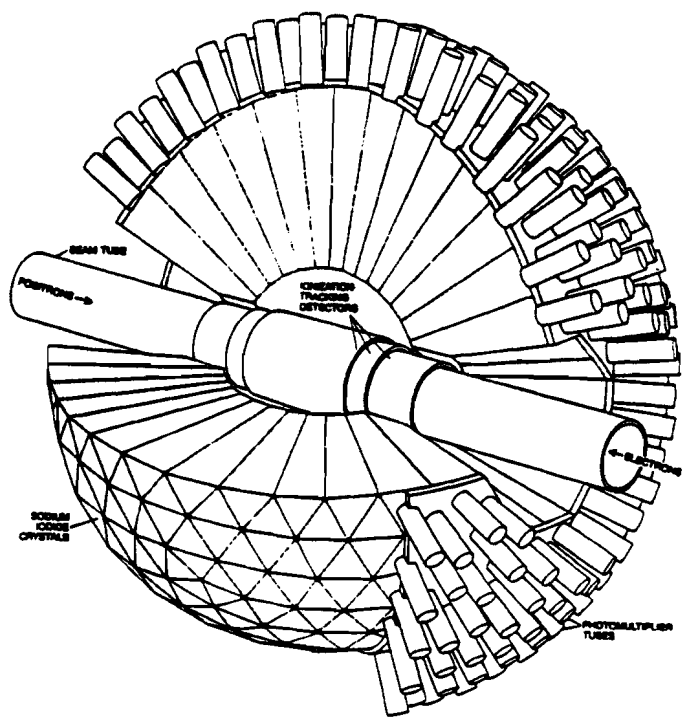

Figure 1.1: The Crystal Ball Detector.

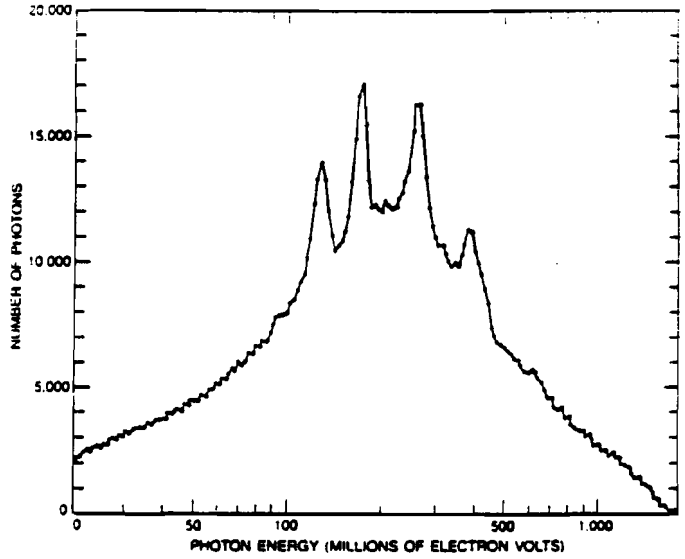

Figure 1.2: The Crystal Ball ψ' inclusive photon spectrum.

1.1.2 R704

The R704 experiment [2], conducted at the CERN ISR, was the first to study charmonium through the annihilation of protons and anti-protons. R704 used a two arm, non-magnetic spectrometer (shown in figure 1.3) designed to detect e^+e^-, $e^+e^-\gamma$, and $\gamma\gamma$ final states. By using stochastically cooled antiprotons interacting with a molecular hydrogen target, R704 was able to attempt the first direct measurements of the $\chi_{1,2}$ resonance widths. The results of R704's study of the $\chi_{1,2}$ resonances are summarized in tables 1.1 and 1.2.

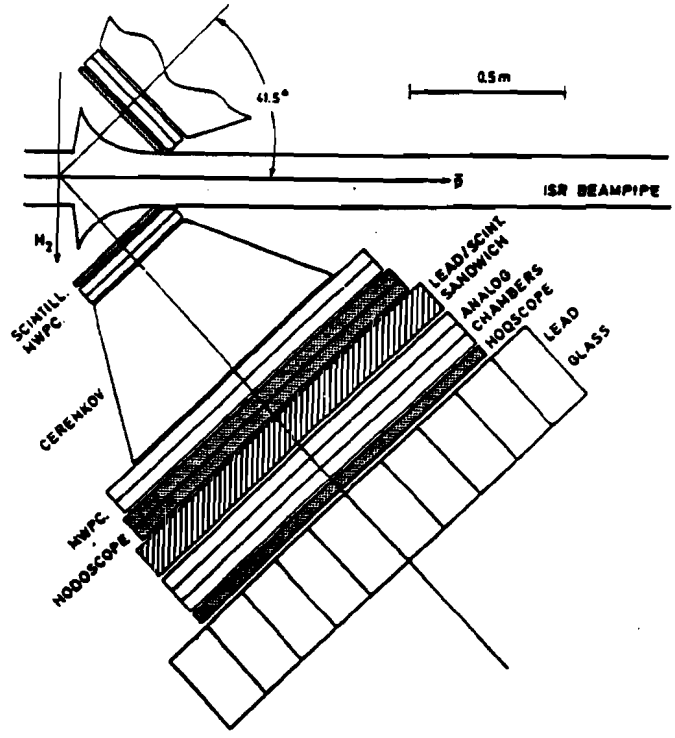

Figure 1.3: The R704 experimental apparatus.

	Crystal Ball χ_1	R704 χ_1
Mass (MeV/c^2)	$3512.3 \pm 0.3 \pm 4.0$	$3511.3 \pm 0.4 \pm 0.4$
Width (MeV)	< 3.8 (90% CL)	< 1.3 (95% CL)
$BR(R \to \bar{p}p) \times 10^{-4}$	—	> 0.54 (95% CL)
$BR(R \to J/\psi)$	0.284 ± 0.021	—
a_2	$-0.002^{+0.020}_{-0.008}$	-0.13 ± 0.19

Table 1.1: Previous results for the χ_1.

	Crystal Ball χ_2	R704 χ_2
Mass (MeV/c^2)	$3557.8 \pm 0.2 \pm 4.0$	$3556.9 \pm 0.4 \pm 0.5$
Width (MeV)	$2.8^{+2.1}_{-2.0}$	$2.6^{+1.4}_{-1.0}$
$BR(R \rightarrow \bar{p}p) \times 10^{-4}$	—	$0.90^{0.41}_{0.26} \pm 0.19$
$BR(R \rightarrow J/\psi)$	0.124 ± 0.015	—
a_2	$-0.333^{+0.292}_{-0.116}$	0.47 ± 0.26
a_3	—	0.09 ± 0.2
B_0^2	—	< 0.08

Table 1.2: Previous results for the χ_2.

1.2 Experimental Methods in E760

E760 uses the Fermilab $\bar{p}$ Source to provide $\bar{p}s$ for collision with protons from the internal hydrogen gas jet target. The cooled $\bar{p}$ beam continuously collides with the gas jet to produce high luminosities ($\sim 10^{31}\ cm^{-2}s^{-1}$) from a small interaction region ($1\ cm^3$). The initial state energy is completely determined by the $\bar{p}$ momentum which is determined to a high accuracy from measurements of the beam revolution frequency and knowledge of the Accumulator's circumference.

The E760 detector is a large acceptance non-magnetic spectrometer with cylindrical symmetry and full azimuthal coverage. As will be discussed in detail later, the most important function of the E760 detector is to select out the small number of resonant charmonium events from a background cross section that is $\sim 10^6$ times larger. The E760 detector has been optimized to look for the electromagnetic decays of charmonium states.

E760 extracts $\chi_{1,2}$ resonance parameters from an analysis of excitation curves which are produced by plotting the observed cross section for the reaction $\bar{p}p \rightarrow \chi_{1,2} \rightarrow J/\psi + \gamma \rightarrow e^+e^- + \gamma$ versus the center-of-mass energy. The observed excitation curve is the convolution of the Breit-Wigner resonance line shape and the energy profile of the beam. As will be discussed later, the high precision of E760's measurements come from an accurate knowledge of the center-of-mass energy distribution. Since the center-of-mass energy spread is typically 3 to 6 times smaller than the resonance widths being examined, the deconvolution of the resonance profile and the beam profile is straightforward. In the analysis of the resonance parameters, the

E760 detector functions as a very selective counting device while the Accumulator is the spectrometer; here is the key difference between the method employed by E760 and Crystal Ball. Unlike Crystal Ball which tries to measure the energy of the final state and is thus limited by detector resolution, E760's measurements of the resonance widths depend on knowledge of the initial state energy which is very well known.

The data used in this dissertation were collected during the period June to September of 1990 (the "1990 run") and June to December of 1991 (the "1991 run"). Although not discussed in this dissertation, E760 has produced a multitude of results relating to charmonium as well as non-charmonium physics. The combination of a precisely known initial state energy, a small interaction point, and a high resolution spectrometer has been very successful.

1.3 Nonrelativistic Potential Models

In this section and the remaining ones in this chapter, I will try to motivate the measurements described in this dissertation by reviewing some of the salient topics in the potential model description of the charmonium system. The discussion below is certainly not exhaustive and reflects a considerable amount of personal bias. The literature on charmonium is extremely rich and I will attempt to reference some relevant works. Some good reviews on charmonium can be found in survey papers by V.A. Novikov et al. [3], by L. Bugge [4], W. Kwong et al. [5], and C. Quigg [6]. The references to the literature could not possibly be complete but are sufficient

to provide a starting point for further study. The last chapter of this dissertation will discuss some specific theoretical predictions and compare them to the measured results.

Soon after the discovery of the J/ψ it was realized that if the J/ψ really was a bound $c\bar{c}$ pair, then the interaction between them might be described by some sort of effective potential. If the form of the potential could be guessed (or derived from physical knowledge) and the system were approximately nonrelativistic, then all the tools developed to study the hydrogen atom could be brought to bear on charmonium. In particular, once the potential $V(r)$ has been chosen (to parameterize the effective quark-antiquark interaction) then the Schrödinger equation

$$[-\frac{\Delta^2}{2\mu} + (V(r) - E)]\Psi(\vec{r}) = 0 \tag{1.1}$$

can be solved to reproduce the charmonium spectrum (see figure .1).

Two kinds of potentials have been proposed, those that are QCD inspired and those that are purely phenomenological. The QCD inspired potentials are derived from the QCD ideas of quark confinement and asymptotic freedom. Quark confinement leads to the notion that the potential rises with increasing inter-quark separation r (say linearly) while asymptotic freedom demands that the color force weakens for small inter-quark separations. One specific example of a QCD inspired potential is the "Cornell Potential" [7]:

$$V(r) = -\frac{4}{3}\frac{\alpha_s}{r} + ar. \tag{1.2}$$

The Cornell Potential incorporates a confinement term proportional to r and a Coulomb-like term which is expected to dominate at small separations due to single

gluon exchange. The purely phenomenological potentials have functional forms that are not directly related to any physical principles. One example of a purely phenomenological potential is the power law potential [8]:

$$V(r) = Ar^{\nu} + B. \tag{1.3}$$

It turns out that both the QCD motivated and purely phenomenological potentials are very successful at predicting the spin averaged charmonium spectrum. The reason for the success of the various models is that all the potentials have roughly the same r dependance in the range 0.1 fm to 1.0 fm [9] (which is the relevant interquark separation for the charmonium system). In order to calculate the fine structure (i.e. ^3P_J level spacings), and hyperfine structure (i.e. ^3S-^1S and ^3P-^1P spacings) one must incorporate into the potential the spin-orbit, spin-spin, and spin-tensor interactions. Once spin is incorporated into the potential, the purely non-relativistic approach is given up. The spin dependent terms in the potential can be obtained from a nonrelativistic approximation to the Breit-Fermi Hamiltonian [10]:

$$V_{LS}(r) = (\vec{L}\cdot\vec{S})\frac{1}{2m^2 r}\left[3\frac{dV_v}{dr} - \frac{dV_s}{dr}\right] \tag{1.4}$$

$$V_{SS}(r) = \frac{(2\vec{\sigma_1}\cdot\vec{\sigma_2} - 3)}{6m^2}\nabla^2 V_v(r) \tag{1.5}$$

$$V_{tensor}(r) = \frac{3(\vec{\sigma_1}\cdot\hat{r})(\vec{\sigma_2}\cdot\hat{r}) - (\vec{\sigma_1}\cdot\vec{\sigma_2})}{12m^2}\left[\frac{1}{r}\frac{dV_v}{dr} - \frac{d^2V_v}{dr^2}\right] \tag{1.6}$$

where $V_v(r)$ and $V_s(r)$ are the vector and scalar parts of the potential, respectively, $\vec{L}$ is the total angular momentum of the $c\bar{c}$ system, $\vec{s_1} = \vec{\sigma_1}/2$ and $\vec{s_2} = \vec{\sigma_2}/2$ are the quark spins, $\vec{S} = \vec{s_1} + \vec{s_2}$, and m is the charmed quark mass.

The charmonium potential as described in equations 1.2, 1.4, 1.5, and 1.6 has several unspecified parameters that determine the relative importance of the individual parts of the interaction. Most authors determine these parameters by conducting fits to the charmonium mass spectrum. Precise measurements of the charmonium masses are then important inputs to most models. Since the triplet P states would be degenerate without spin dependent forces, the P state masses are very interesting. The success of the charmonium models can be evaluated by comparing experimentally measured quantities with their predicted values. Such comparisons are conducted in chapter 7.

1.3.1 Relativistic Effects

While the non-relativistic treatment of the charmonium system has been reasonably successful (possibly more than one should have expected), the effects of relativity should be examined. Using the virial theorem it is possible to get an idea of the importance of relativistic effects. The virial theorem can be written as

$$2\langle T\rangle = \langle \vec{r}\cdot\vec{\nabla}V(\vec{r})\rangle \tag{1.7}$$

where T is the kinetic energy and $\langle\ \rangle$ denotes expectation value [8]. If we assume that the potential, at the mean radius of the charmonium system, is dominated by the confinement term

$$V = ar \tag{1.8}$$

it then follows that

$$2\langle T\rangle = \langle V\rangle. \tag{1.9}$$

If we use the relation for the binding energy $E = \langle T \rangle + \langle V \rangle$ and the non-relativistic expression for $\langle T \rangle = 2(1/2)m_c\langle v^2 \rangle$ then we get

$$\langle v^2 \rangle = \frac{E}{3m_c} \tag{1.10}$$

where m_c is the mass of the charm quark and $\langle v^2 \rangle$ is the expectation value of the squared quark velocity. One can make a crude estimate by taking the charm quark mass as $m_c = 1.5\ GeV/c^2$ and the binding energy as the mass difference between J/ψ and ψ', $E = 673\ MeV$. The resulting estimate of $\langle v^2 \rangle$ for the charmonium system is that $\langle v^2 \rangle_{\bar{c}c} \approx 0.15$. While this is only a rough estimate, it does imply that relativistic effects might be significant and should be explored.

There are two approaches to deal with relativistic effects in the charmonium system (see [11,12,13,14,15,16] for example). The first method is to calculate some corrections to the nonrelativistic treatment by expanding the Hamiltonian H. Many authors have pursued this approach and have conducted calculations that are valid to order v^2/c^2. The second method is to abandon the non-relativistic treatment altogether and adopt a completely relativistic approach. Specific model dependent predictions for the relativistic effects are discussed in chapter 7 where predictions for the radiative widths are compared to the measurements presented in this dissertation.

1.4 The $\chi_{1,2}$ Radiative Decays

As mentioned earlier the extreme narrowness of the charmonium resonances is due to OZI suppression of states that lie below the open charm threshold. It is this suppression of OZI diagrams that allows the easy observation of radiative transitions between charmonium resonances.

In the non-relativistic limit only the dipole operator contributes significantly to the radiative transition rates of the $\chi_{1,2}$ states to J/ψ. The dipole approximation of the transition rate is given by the simple form

$$\Gamma(^3P_J \rightarrow ^3S_1 + \gamma) = \frac{4\alpha e_c^2 E_\gamma^3}{9} |\langle f|r|i\rangle|^2 \tag{1.11}$$

where the matrix element involves normalized radial wave functions and e_c is the electric charge of the charm quark in units of $|e|$. When relativistic effects are considered, the pure dipole transition is replaced by an admixture of $J+1$ multipole transitions. Each multipole has a definite parity and angular momentum. As is discussed in chapter 7 the lowest allowed multipole dominates the radiative rate. For the angular distributions however, even small contributions from higher multipoles greatly changes the shape.

In the next section the angular distributions for the $\chi_{1,2}$ will be derived in terms of the initial state helicities and radiative decay multipoles. As is discussed in chapter 7, the relative size of the initial state helicity amplitudes allows study of the χ formation process while determination of the radiative decay multipole amplitudes provides insight into the interquark potential.

1.4.1 The Helicity and Multipole Amplitudes

The angular distribution function can be derived in terms of the helicity formalism as described by Jacob and Wick [17]. Since the helicity operator $h = \vec{S} \cdot \hat{p}$ is invariant under both rotations and boosts along $\hat{p}$, it is possible to construct relativistic basis vectors that are eigenstates of either total angular momentum and helicity or of linear momentum and helicity. This property makes the helicity formalism a convenient method for obtaining the angular distributions for relativistic scattering and decay processes.

The χ_1 and χ_2 radiative angular distributions have been derived using the helicity formalism by several authors [18,19,20]. Since the angular distributions described by [18] and [19] both suffer from typographical errors and an ambiguity in the definition of the angle θ' (defined below), I have recalculated them and found them consistent with the distributions quoted by reference [20]. Below is an outline of the helicity formalism calculation for the $\chi_{1,2}$ radiative angular distributions; the notation employed follows closely that used in reference [20].

The angular distribution for the $\bar{p}p \rightarrow \chi_{1,2} \rightarrow J/\psi + \gamma \rightarrow e^+e^- + \gamma$ can be described in terms of three angles θ, θ' and ϕ', which are defined as follows (see figure 1.4.1)

- θ: the polar angle of the J/ψ with respect to the antiproton beam, in the center-of-mass system;
- θ': the polar angle of the positron with respect to the J/ψ line of flight, defined in the J/ψ rest frame;

- ϕ': the azimuthal angle of the positron in the J/ψ rest frame, where the X' axis is in the plane containing the photon and the antiproton, and $\phi' = 0$ for the antiproton.

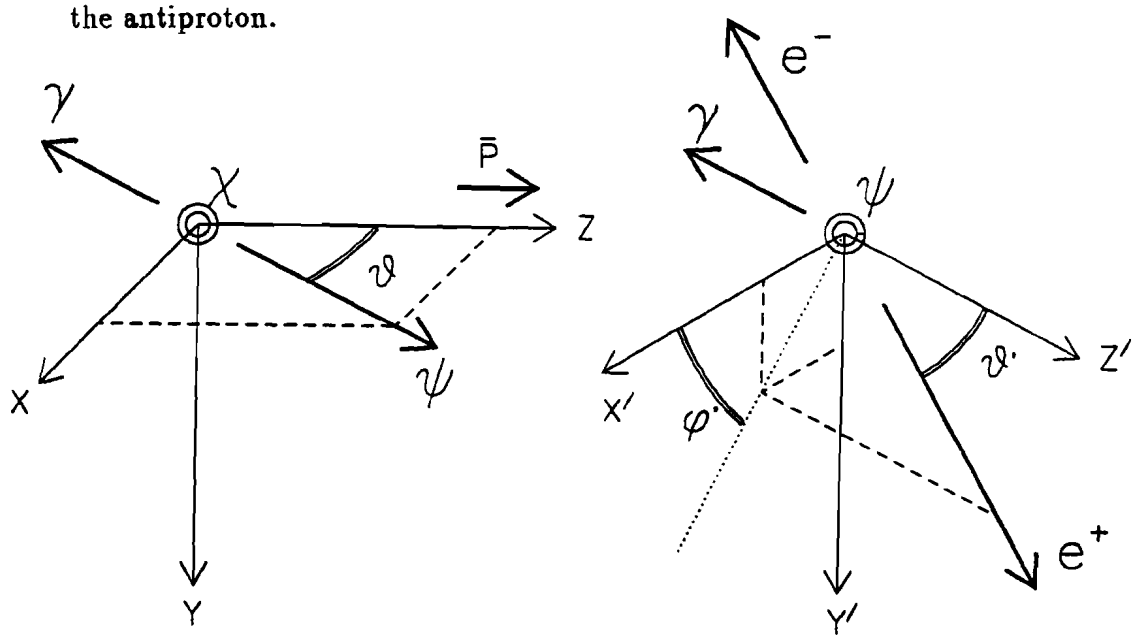

Figure 1.4: The angular definitions for $\bar{p}p \to \chi_{1,2} \to J/\psi + \gamma \to e^+e^- + \gamma$.

The probability amplitude for the process

$$\bar{p}(\lambda_1)p(\lambda_2) \to \chi_J(\nu) \to J/\psi(\sigma) + \gamma(\mu) \to e^-(\kappa_1) + e^+(\kappa_2) + \gamma(\mu) \qquad (1.12)$$

where λ_1, λ_2, ν, σ, μ, κ_1, and κ_2 are the particle helicities, can be written as the product of the sequential processes where the χ_J is produced from $\bar{p}p$, decays radiatively to a J/ψ, and then followed by the decay of the J/ψ to e^+e^-. Using the notation of Jacob and Wick, one can write the two particle plane wave helicity states in terms of angular momentum states as:

$$|p, \theta, \phi; \lambda_1\lambda_2\rangle = \sum_{J,M} \left[\frac{2J+1}{4\pi}\right]^{1/2} D^J_{M\lambda}(\phi, \theta, -\phi)|pJM; \lambda_1\lambda_2\rangle, \qquad (1.13)$$

where ϕ, θ, and $-\phi$ are the three Euler angles and the D functions use the sign convention defined by Rose [21]. In the rest frame of the χ_J one obtains the amplitude for the process $\bar{p}(\lambda_1)p(\lambda_2) \rightarrow \chi_J(\nu)$ as

$$\langle J\nu|B|\theta 0, \lambda_1\lambda_2\rangle = \left[\frac{2J+1}{4\pi}\right]^{1/2} B^J_{\lambda_1\lambda_2} D^J_{\nu\lambda}(0,\theta,0), \tag{1.14}$$

where $\lambda = \lambda_1 - \lambda_2$, B is a transition operator, and $B^J_{\lambda_1\lambda_2}$ represents the partial wave amplitude. Similarly the amplitude for the process $\chi_J(\nu) \rightarrow J/\psi(\sigma) + \gamma(\mu)$ (where the J/ψ is moving along the $+\hat{z}$ direction and the γ along the $-\hat{z}$) is given by

$$\langle 00, \sigma\mu|A|J\nu\rangle = \left[\frac{2J+1}{4\pi}\right]^{1/2} A^{J*}_{\sigma\mu} D^{J*}_{\nu\nu'}(0,0,0), \tag{1.15}$$

where $\nu' = \sigma - \mu$. In the rest frame of the J/ψ, the amplitude for the process $J/\psi(\sigma) \rightarrow e^-(\kappa_1) + e^+(\kappa_2)$ is given by

$$\langle \theta'\phi'; \kappa_1\kappa_2|C|1\sigma\rangle = \left[\frac{3}{4\pi}\right]^{1/2} C_{\kappa_1\kappa_2} D^{1*}_{\sigma\kappa}(\phi',\theta',-\phi'), \tag{1.16}$$

where $\kappa = \kappa_1 - \kappa_2$.

The amplitude for the sequential process $\bar{p}p \rightarrow \chi_{1,2} \rightarrow J/\psi + \gamma \rightarrow e^+e^- + \gamma$ through all possible intermediate helicity states ν and σ is given by the sum of the product of amplitudes 1.14, 1.15, and 1.16 and can be expressed as

$$T^J_{\lambda_1,\lambda_2,\kappa_1,\kappa_2} = \left[\frac{3(2J+1)^2}{(4\pi)^3}\right]^{1/2} B^J_{\lambda_1\lambda_2} C_{\kappa_1\kappa_2} \sum_{\nu(\mu)} A^J_{\nu\mu} D^{1*}_{\nu+\mu,\kappa}(\phi',\theta',-\phi') d^J_{\nu\mu}(\theta), \tag{1.17}$$

where the relations $D^J_{\nu\lambda}(0,\theta,0) = d^J_{\nu\lambda}$ and $D^J_{\nu\nu'}(0,0,0) = \delta_{\nu\nu'}$ have been used. In equation 1.17 the photon polarization index μ can only take the values -1 and +1 while the summation index ν takes values 0 to $+J$ for $\mu = -1$ and $-J$ to 0 for $\mu = +1$. By squaring the absolute magnitude of equation 1.17, summing over final

helicities (κ_1, κ_2, and μ), and averaging over the intial helicities (λ_1 and λ_2) one then obtains the unnormalized joint angular distribution for the cascade process when the initial $\bar{p}$ and p are unpolarized and the final state polarizations are not measured.

If we employ the symmetry properties of the helicity amplitudes for two body processes [22] then charge conjugation invariance leads to:

$$B^J_{\lambda_1\lambda_2} = (-1)^{L+S}(-1)^J B^J_{\lambda_2\lambda_1} \tag{1.18}$$

and

$$C_{\kappa_1\kappa_2} = (-1)^{L+S}(-1)^1 C_{\kappa_2\kappa_1}, \tag{1.19}$$

while parity invariance leads to:

$$A^J_{\nu\mu} = (-1)^{L+1}(-1)^J A^J_{-\nu-\mu}, \tag{1.20}$$

$$B^J_{\lambda_1\lambda_2} = (-1)^{L+1}(-1)^J B^J_{-\lambda_1-\lambda_2}, \tag{1.21}$$

and

$$C_{\kappa_1\kappa_2} = (-1)^{L+1}(-1)^J C_{-\kappa_1-\kappa_2}. \tag{1.22}$$

Now using equations 1.18 through 1.22 one gets the following relations:

$$\begin{aligned}
A_{\nu,-1} &= +A_{-\nu,1} \equiv A^J_\nu \quad for\ J=2 \\
A_{\nu,-1} &= -A_{-\nu,1} \equiv A^J_\nu \quad for\ J=1 \\
|B^J_{+-}|^2 &= |B^J_{-+}|^2 \equiv B_1^2 \\
|B^J_{++}|^2 &= |B^J_{--}|^2 \equiv \frac{1}{2}B_0^2 \\
|C^J_{++}|^2 &= |C^J_{--}|^2 \equiv \frac{1}{2}C_0^2 \\
|C^J_{+-}|^2 &= |C^J_{-+}|^2 \equiv C_1^2.
\end{aligned} \tag{1.23}$$

The normalization conditions used are:

$$\sum_{\nu}^{J} |A_{\nu}^{J}|^2 = 1.$$

$$\sum_{\nu}^{J} |B_{\lambda_1\lambda_2}^{J}|^2 = 2B_1^2 + B_0^2 = 1, \tag{1.24}$$

$$\sum_{\nu}^{J} |C_{\kappa_1\kappa_2}|^2 = 2C_1^2 + C_0^2 = 1 \approx 2C_1^2, \tag{1.25}$$

The decay of the J/ψ to e^+e^- proceeds through a photon, so the approximation that $C_1^2 >> C_0^2$ is justified since $m/E \simeq 3.3 \times 10^{-4}$.

Now using the normalization condition that the integral over all space of the angular distribution function is one and relations 1.17 through 1.25, one can write the normalized angular distribution as

$$\begin{aligned} W(\theta,\theta',\phi') &= \frac{3(2J+1)^2}{64\pi^2} \sum_{\lambda=\pm1,0} |B_{|\lambda|}^{J}|^2 \sum_{\mu=\pm1} \sum_{\nu(\mu)\nu'(\mu)} A_{|\nu'|}^{*} A_{|\nu|} d_{\nu'\lambda}^{J}(\theta) \\ & d_{\nu\lambda}^{J}(\theta) \sum_{\kappa=\pm1} D_{\nu'+\mu,\kappa}^{1}(\phi',\theta',-\phi') D_{\nu+\mu,\kappa}^{1*}(\phi',\theta',-\phi'). \end{aligned} \tag{1.26}$$

Notice that the constant $2C_1^2$ has been absorbed into the overall normalization of the angular distribution function and that the helicities $A_{|\nu|}$ no longer depend on the parity of the $\chi_{1,2}$. Also the angular distribution function depends on $|B_{|\lambda|}^{J}|^2$ and not $B_{|\lambda|}^{J}$. This last point is relevant in chapter 4 when the fits to the data are conducted.

The relation between the helicity amplitudes $A_{|\nu|}$ and the multipole amplitudes a_k is given by the linear transformation [19]

$$A_{|\nu|} = \sum_{k} a_k \left[\frac{2k+1}{2J+1}\right]^{1/2} \langle k,1;1,\nu-1|J,\nu\rangle. \tag{1.27}$$

The χ_2 Angular Distribution

The normalized angular distribution for the χ_2 radiative decay can be derived from equation 1.26 and is written as a sum over the functions T_i which involve only the helicity amplitudes and the functions K_i which involve only the angles θ, θ', and ϕ'. For the χ_2 the result is

$$W(\theta,\theta',\phi';R,A_0,A_1,A_2) = \frac{15}{64\pi^2}\sum_{i=1,11} T_i(\theta,\theta',\phi')\cdot K_i(R,A_0,A_1,A_2), \qquad (1.28)$$

where $T_i(\theta,\theta',\phi')$ and $K_i(R,A_0,A_1,A_2)$ are defined in table 1.3. By convention the ratio R is defined as

$$R \equiv \frac{2B_1^2}{B_0^2+2B_1^2} = 2B_1^2 \qquad (1.29)$$

where I have used the normalization condition from equation 1.25.

i	$T_i(\theta,\theta',\phi')$	$K_i(R,A_0,A_1,A_2)$
1	1	$\frac{1}{8}(2A_0^2+3A_2^2-R(2A_0^2-4A_1^2+A_2^2))$
2	$\cos^2\theta$	$\frac{3}{4}(-2A_0^2+4A_1^2-A_2^2+R(4A_0^2-6A_1^2+A_2^2))$
3	$\cos^4\theta$	$\frac{1}{8}(6A_0^2-8A_1^2+A_2^2)(3-5R)$
4	$\cos^2\theta'$	$\frac{1}{8}(2A_0^2+3A_2^2-R(2A_0^2+4A_1^2+A_2^2))$
5	$\cos^2\theta'\cos^2\theta$	$\frac{3}{4}(-2A_0^2-4A_1^2-A_2^2+R(4A_0^2+6A_1^2+A_2^2))$
6	$\cos^2\theta'\cos^4\theta$	$\frac{1}{8}(6A_0^2+8A_1^2+A_2^2)(3-5R)$
7	$\sin^2\theta'\cos^2\phi'$	$\frac{\sqrt{6}}{4}(R-1)A_0A_2$
8	$\cos^2\theta\sin^2\theta'\cos^2\phi'$	$\frac{\sqrt{6}}{4}(4-6R)A_0A_2$
9	$\cos^4\theta\sin^2\theta'\cos^2\phi'$	$\frac{\sqrt{6}}{4}(5R-3)A_0A_2$
10	$\sin 2\theta\sin 2\theta'\cos\phi'$	$\frac{\sqrt{3}}{4}(A_0A_1+\sqrt{\frac{3}{2}}A_1A_2-R(2A_0A_1+\sqrt{\frac{3}{2}}A_1A_2))$
11	$\cos^2\theta\sin 2\theta\sin 2\theta'\cos\phi'$	$\frac{-1}{4\sqrt{3}}(5R-3)(3A_0A_1+\sqrt{\frac{3}{2}}A_1A_2)$

Table 1.3: Angular distribution functions for χ_2.

Using equation 1.27 the helicity amplitudes A_i for the χ_2 radiative decay process

can be written in terms of the radiative multipole amplitudes:

$$\begin{aligned} A_0 &= \sqrt{\frac{1}{10}}a_1 + \sqrt{\frac{1}{2}}a_2 + \sqrt{\frac{2}{5}}a_3, \\ A_1 &= \sqrt{\frac{3}{10}}a_1 + \sqrt{\frac{1}{6}}a_2 - \sqrt{\frac{8}{15}}a_3, \\ A_2 &= \sqrt{\frac{3}{5}}a_1 - \sqrt{\frac{1}{3}}a_2 + \sqrt{\frac{1}{15}}a_3. \end{aligned} \tag{1.30}$$

The χ_1 Angular Distribution

The normalized angular distribution for the χ_1 radiative decay can also be derived from equation 1.26 and is written as a sum over the functions T_i which involve only the helicity amplitudes and the functions K_i which involve only the angles θ, θ', and ϕ'. For the χ_1 the result is

$$W(\theta, \theta', \phi'; R, A_0, A_1, A_2) = \frac{9}{64\pi^2} \sum_{i=1,5} T_i(\theta, \theta', \phi') \cdot K_i(R, A_0, A_1, A_2), \tag{1.31}$$

where $T_i(\theta, \theta', \phi')$ and $K_i(R, A_0, A_1, A_2)$ are defined in table 1.4. The ratio R is defined in the previous section. However, recall from equation 1.21 that charge conjugation invariance leads to

$$B^1_{++} = -B^1_{++} = 0 \tag{1.32}$$

and

$$B^1_{--} = -B^1_{--} = 0 \tag{1.33}$$

for $J = 1$. So now from equation 1.23 we see that

$$B^2_0 = 2|B^1_{++}|^2 = 2|B^1_{--}|^2 = 0, \tag{1.34}$$

which gives the result that

$$R \equiv \frac{2B_1^2}{B_0^2 + 2B_1^2} = 1. \tag{1.35}$$

This result then implies that the χ_1 angular distribution is not sensitive to the initial state helicities.

i	$T_i(\theta, \theta', \phi')$	$K_i(A_0, A_1, A_2)$
1	1	$(A_1^2 + \frac{1}{2}(A_0^2 - A_1^2))$
2	$\cos^2\theta$	$-\frac{1}{2}(A_0^2 - A_1^2)$
3	$\cos^2\theta'$	$(\frac{1}{2} - A_1^2)$
4	$\cos^2\theta'\cos^2\theta$	$-\frac{1}{2}$
5	$\sin 2\theta \sin 2\theta' \cos\phi'$	$-(\frac{1}{4})A_1A_0$

Table 1.4: Angular distribution functions for χ_1.

Using equation 1.27 the helicity amplitudes A_i for the χ_1 radiative decay process can be written in terms of the radiative multipole amplitudes:

$$A_0 = \sqrt{\frac{1}{2}}(a_1 + a_2),$$
$$A_1 = \sqrt{\frac{1}{2}}(a_1 - a_2). \tag{1.36}$$

Chapter 2

The E760 Apparatus

The E760 apparatus is composed of four distinct parts: the Accumulator, the gas jet target, the luminosity monitor, and the detector. As will be discussed later, the Accumulator is responsible for the accuracy of E760's measurements of charmonium resonance parameters. The Accumulator completely and precisely determines the initial state energy. The gas jet provides the point-like interaction region that allows E760 to trigger in a high rate environment, while the luminosity monitor is able to accurately record the interaction rate by measuring elastic scattering of $\bar{p}p$. The E760 detector's biggest job is to be a highly selective event counting device.

2.1 The $\bar{p}$ Source

The $\bar{p}$ Source is part of a much larger accelerator complex (see figure 2.1) originally designed to conduct $\bar{p}p$ collisions at center of mass energy of 2 (TeV) using the Fermilab Tevatron. Fermilab has two modes of operation, the Collider Mode and the Fixed Target Mode. During collider operations the $\bar{p}$ source and related facilities are completely dedicated to providing $\bar{p}s$ for collisions in the Tevatron. During the

Fixed Target operations however, the $\bar{p}$ source is almost exclusively dedicated to the operation of E760.

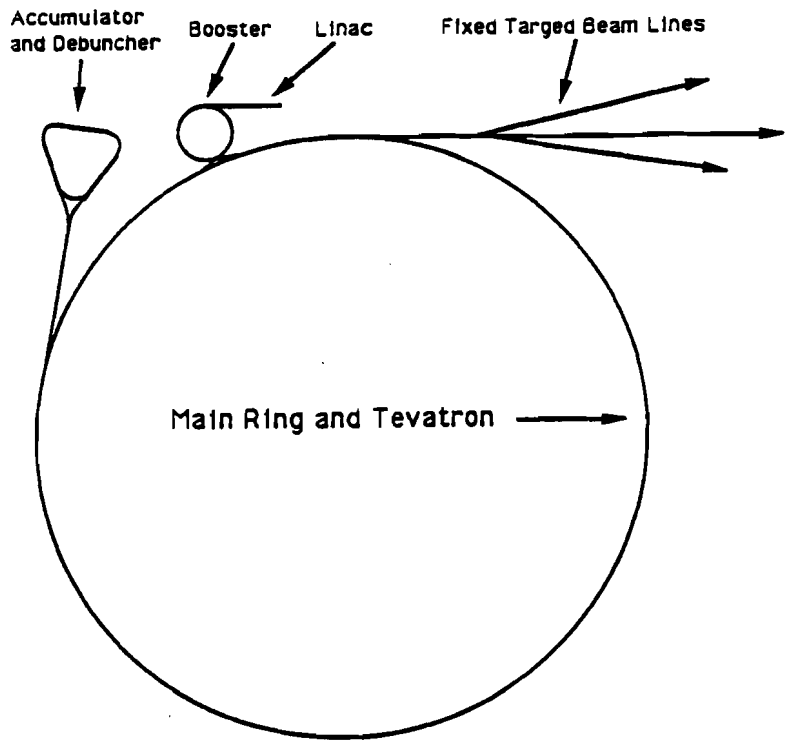

Figure 2.1: The Fermi National Laboratory accelerator complex.

The $\bar{p}$ Source [23] (see figure 2.2) is composed of three parts: the Target Station, the Debuncher ring, and the Accumulator ring. Protons from the Main Ring strike the target to produce $\bar{p}s$ which travel down a transfer line to be injected into the Debuncher. Only negatively charged particles with a momentum of about 8.9 (GeV/c) are accepted into the Debuncher. The $\bar{p}s$ spend about 2 seconds being manipulated in the Debuncher before they are transferred to the Accumulator for storage. It is interesting that the Accumulator, which was not designed for E760, is almost an ideal machine for such an experiment. The Accumulator contains three low dispersion straight sections, two of which are occupied by RF and cooling sys-

tems. The third straight section (AP-50) is occupied by the E760 detector. The 8.9 (GeV) stacking energy, which was chosen to maximize the $\bar{p}$ yield from 120 (GeV) Main Ring protons, is just above that needed to form all of the charmonium resonances of interest to this experiment. Also fortuitous for E760 is the existence of a very good stochastic cooling [24] system that provides the narrow beam widths required in order to scan sub-MeV wide resonances. The Accumulator's 300 hour beam lifetime and ability to store large stacks (10^{12}) of $\bar{p}s$ allowed E760 to collect over $30pb^{-1}$ of data in 8 months of running time.

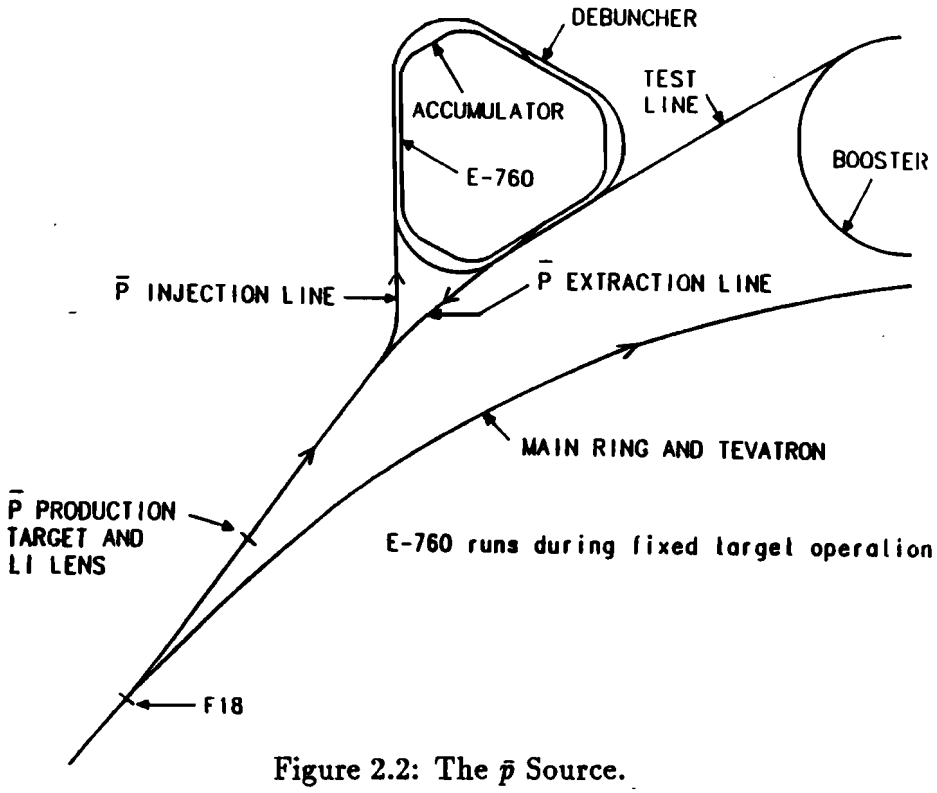

Figure 2.2: The $\bar{p}$ Source.

2.1.1 $\bar{p}$ Production and Deceleration

$\bar{p}$ production begins with acceleration of negative hydrogen ions in an 800 KeV Cockroft-Walton generator which are then passed into the Linac, a 200 MeV linear accelerator. The hydrogen ions are stripped of their electrons as they pass from the Linac into the 8 GeV Booster synchrotron. As often as every two seconds, a Booster batch containing 2×10^{12} protons in 82 rf bunches is injected into the Main Ring where it is accelerated to 120 GeV. After acceleration in the Main Ring, a series of rf manipulations are carried out in order to reduce the energy spread to about 185 MeV and a bunch width of 0.7 $nsec$. These manipulations are essential in order the maximize $\bar{p}$ yields. The short proton bunches are extracted from the Main Ring and are guided onto a tungsten target where they produce 82 equally short $\bar{p}$ bunches.

From each batch (82 bunches) of protons hitting the target, some 7×10^7 $\bar{p}s$ are produced. These $\bar{p}s$ are collected by a 15 cm long lithium lens. At this point the 8.9 GeV/c $\bar{p}$ beam has a momentum spread of 3% and emittances of 20π $mm - mrad$ in each plane. The $\bar{p}$ beam is then transported and injected into 53 MHz rf buckets in the Debuncher ring. After 2 seconds of rf manipulations (similar to those conducted on the protons in the Main Ring) the Debuncher has reduced the momentum spread of the $\bar{p}s$ to about 0.2% and has also stochastically cooled the emittances to 7π $mm - mrad$. It is at this point that the $\bar{p}s$ are finally injected into the Accumulator for further cooling and storage. A typical 30 mA (3×10^{11}) stack of $\bar{p}s$ takes about 24 hours to accumulate and cool. At the end of the stacking process, E760 is given control of the stack of 8.9 GeV of $\bar{p}$s which have stochastically

cooled emittances of $2\pi\ mm - mrad$.

In order for E760 to resonantly produce the various charmonium states (see table 2.1) of interest, the $\bar{p}$ beam must be decelerated [25]. The Accumulator, however, has been designed to run at a fixed momentum of 8.9 GeV and is not equipped with a hardware control system necessary to conduct beam decelerations. The deceleration process is accomplished by the use of an auxiliary front-end computer [26] that sets the current in 89 devices as a function of beam momentum to simulate a "ramp". These software ramps are just piece-wise linear functions of small steps. The deceleration process is relatively slow (proceeding at only $\sim$ 20 MeV/s) because the large quadrupoles and bending dipoles are run well into saturation at the design energy and cannot be ramped quickly. Once the beam has been decelerated to just above the energy of interest, the resonance being studied can be scanned by changing the beam energy in small steps. The minimum step size of the ramp is determined by the least significant bit of the dipole power supply's digital control which corresponds to 150 keV in the lab. Decelerations and scans have been successfully completed for all the lowlying charmonium resonances (see table 2.1) except the χ_0 and the η_c'.

2.1.2 $\bar{p}$ Energy Measurement

Determination of the initial state energy is at the heart of E760's ability to preform precision measurements of the various charmonium resonances (see discussion in section 1.2). The measurements of the mean beam energy (E_{beam}) and the mean

State	J^{PC}	Mass (MeV/c^2)	E_{beam} (MeV)
η_c	0^{-+}	2979.6	3792.8
J/ψ	1^{--}	3096.9	4172.6
χ_0	0^{++}	3415.1	5276.8
χ_1	1^{++}	3510.6	5629.3
${}^1P_1$	1^{++}	3526.2	5687.5
χ_2	1^{++}	3556.3	5801.4
η_c'	0^{-+}	?	?
ψ'	1^{--}	3686.0	6301.9

Table 2.1: Charmonium states and the corresponding $\bar{p}$ beam energy threshold for resonant $\bar{p}p$ production.

beam energy spread ($\sigma(E_{beam})$) are based on a determination of the velocity of the beam in the lab frame. The beam velocity is calculated by:

$$c\beta = fL = f(L_0 + \Delta L) \tag{2.1}$$

where L is the orbit length and f is the revolution frequency. The orbit length is given in terms of the reference orbit L_0 and a difference ΔL. By taking the logarithmic derivative of equation 2.1, the velocity spread of the beam can be expressed in terms of the revolution frequency and is given by the differential relation

$$\frac{df}{f} = \frac{d\beta}{\beta} - \frac{dL}{L}. \tag{2.2}$$

dL/L in equation 2.2 can be expressed in terms of γ_t (the transition gamma for the Accumulator lattice) and the beam velocity by the relation (see [27] equation 5.2)

$$\frac{dL}{L} = \frac{\gamma^2}{\gamma_t^2}\frac{d\beta_{beam}}{\beta_{beam}}. \tag{2.3}$$

Now using equation 2.3 which is a general result for strong focusing machines and the relation

$$\frac{d\beta}{\beta} = \frac{1}{\gamma^2\beta^2}\frac{dE_{beam}}{E_{beam}}, \tag{2.4}$$

one obtains from equation 2.2, the following relation between the frequency spread df and the energy spread dE_{beam}:

$$\frac{dE_{beam}}{E_{beam}} = \frac{\beta^2}{\eta}\frac{df}{f}, \tag{2.5}$$

where the parameter η is defined as:

$$\eta = \frac{1}{\gamma^2} - \frac{1}{\gamma_t^2}. \tag{2.6}$$

In order to determine the beam energy and beam energy spread, one must first measure the the revolution frequency, revolution frequency spread, the orbit length, and the machine parameter η.

Measuring f and df

The frequency spectrum of the beam is obtained from the Schottky[28] noise power spectrum. Since the spectral density of the noise is proportional to the particle density in any frequency bin, the Schottky spectrum gives a direct measure of the beam frequency spectrum. The Schottky noise is detected by a coaxial quarter wavelength resonant pickup with a principle frequency of 79.323 MHz. The signal is analysed by a spectrum analyzer (Hewlett Packard model 8568B) every 3 minutes. A typical spectrum is shown in figure 2.3.

Each beam frequency spectrum is fit to a gaussian as shown in figure 2.3. For each run (typically 1-2 hours of data taking) the results of all the fits are averaged together. It is the average (over a run) value for the mean revolution frequency and revolution frequency spread that are used in equation 2.5 to determine $\sigma(E_{beam})$. The error in the mean revolution frequency is very small (less than one part in 10^7).

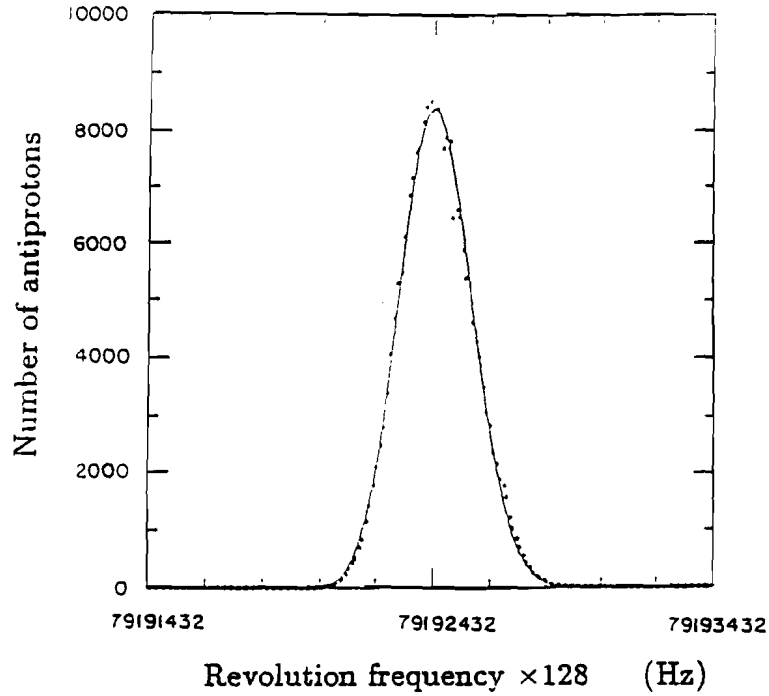

Figure 2.3: A typical beam frequency spectrum. The solid line shows the best fit gaussian.

Measuring the Orbit Length

The orbit length could in principle be measured by using data from a physical survey of magnet positions and alignments. Unfortunately, a survey of the several hundred elements in the Accumulator lattice could not be done with sufficient precision. E760 chose to measure the orbit length by using the known mass of the ψ' resonance.

The reference orbit L_0 is found by tuning the Accumulator energy to the peak of the ψ' resonance. Using equation 2.1, the reference orbit is given by $L_0 = c\beta_0/f_0$, where β_0 is calculated from the ψ' mass. Since the error in the beam frequency is very small, the dominant error in L_0 comes from the published value of the ψ' mass. The 0.1 MeV/c^2 uncertainty in the published value of the ψ' corresponds to

an absolute systematic uncertainty in the reference orbit length of $\delta L_0 = 0.7\ mm$.

If the reference orbit were reproducible at all energies then one would always know the orbit length. In practice the reference orbit is only approximately reproducible, so to find deviations from the reference orbit a system of 48 beam position monitors [29] (BPM) is used. By comparing the BPM readout that was recorded on the reference orbit to the BPM readout on any other orbit, the difference orbit ΔL can be found with an absolute accuracy of $1mm$.

The error in L_0 and the error in ΔL combine to give an overall total systematic error $\delta L = 1.7mm$. At the χ formation energy the error $\delta L = 1.7mm$ implies a systematic mass error of $\Delta M_R = 120\ keV/c^2$.

Determination of η

The machine parameter η is required in equation 2.5 in order to extract the beam energy spread from f and df. As it turns out, η is a very difficult parameter to measure accurately. Fortunately there are at least three methods that can be used to determine η.

The conventional determination of η is made by measuring the synchrotron frequency (ω_s) when the RF is on. In the small oscillation amplitude limit [30] ω_s^2 is proportional to η. This methods yields estimates of η that are accurate to 10%. The second. also conventional, method for the determination of η is to calculate it using equation 2.6 and a measurement of γ_t. The transition gamma (γ_t) can be found by varying the magnetic field of the machine and then measuring the corresponding

change in revolution frequency. The formula

$$\gamma_t^2 = \frac{df/f}{dB/B} \tag{2.7}$$

relates γ_t to the frequency (f) and the magnetic field (B). In this case, the error in η derived from the error in γ_t becomes very large as η becomes small. The third method for measuring η was developed by E760[25]. In the process of conducting a double scan, η becomes a free parameter that can be simultaneously determined along with the resonance mass and width. The double scan method yields an improved determination of η which is accurate to about 6%. Table 2.2 shows the value of η as determined by the various methods at the ψ' energy.

Method	η
synchrotron frequency	-0.0105
γ_t measurement	-0.0109
double scan	-0.0087

Table 2.2: η as measured by three methods in 1990.

Summary

To summarize, E_{beam} is determined by measuring the velocity of the beam in the lab frame. The velocity of the beam in the lab frame is determined from the frequency spectrum of the beam and the orbit length. The error in E_{beam} is dominated by the error in the orbit length. The orbit length has an uncertainty of 1.7 mm. The beam energy distribution is adequately described by a gaussian functional form. The determination of the beam width $\sigma(E_{beam})$ is made from measurements of the

frequency spectrum and the machine parameter η. The error in the beam width $\sigma(E_{beam})$ is dominated by the error in η which is only known to about 10%.

2.2 The H_2 gas jet target

E760 uses an internal (to the Accumulator vacuum chamber) molecular hydrogen gas jet target [31]. The hydrogen gas is cooled and then pumped at high pressure through a narrow trumpet shaped nozzle (see figure 2.4). As the hydrogen expands at supersonic speeds, the central portion of the flow becomes supersaturated. Further down stream the expanding hydrogen begins to nucleate and clusters of $\sim 10^6$ hydrogen molecules form. It is these clusters of hydrogen molecules that become the target material for E760. After the clusters have formed, a series of collimators is used to ensure a small interaction region in the center of the Accumulator beam pipe. On the other side of the Accumulator beam pipe is the collector where the excess hydrogen is pumped out. The interaction region created by E760 jet target and the $\bar{p}$ beam is about 1 cm^3 and the density is about 10^{14} $atoms/cm^3$.

2.3 The Luminosity Monitor

Since E760 cannot measure the thickness of the gas jet target in a reliable way, a luminosity monitor of some sort is required. By utilizing existing measurements of the differential elastic cross section [32] at low momentum transfers ($t < 0.05$ $(GeV/c)^2$) and a solid state silicon detector, E760 can obtain precise

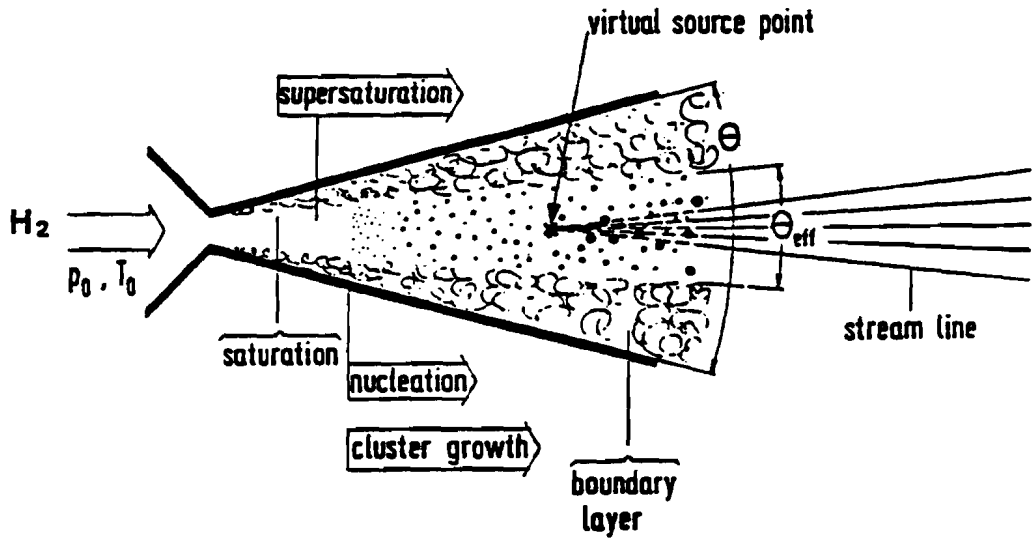

Figure 2.4: Schematic of the gas jet target.

luminosity measurements.

The E760 luminosity monitor counts the recoil protons scattered from the interaction region. Located 147 cm below the gas jet and fixed at $\theta_{lab} = 86.435°$, the $500\mu m$ thick fixed detector stops protons with a recoil energy of up to 8 MeV (see figure 2.5). In addition to the "fixed" detector used to measure the luminosity in E760, an additional six were mounted on a moveable carriage and were used to study the total elastic differential cross section.

The luminosity is extracted from the count rate (N) in the fixed detector by using the relation

$$N = L\frac{d\sigma_{elastic}}{d\Omega}\Delta\Omega. \tag{2.8}$$

In equation 2.8 $\Delta\Omega$ is the solid angle subtended by the detector and is taken to be

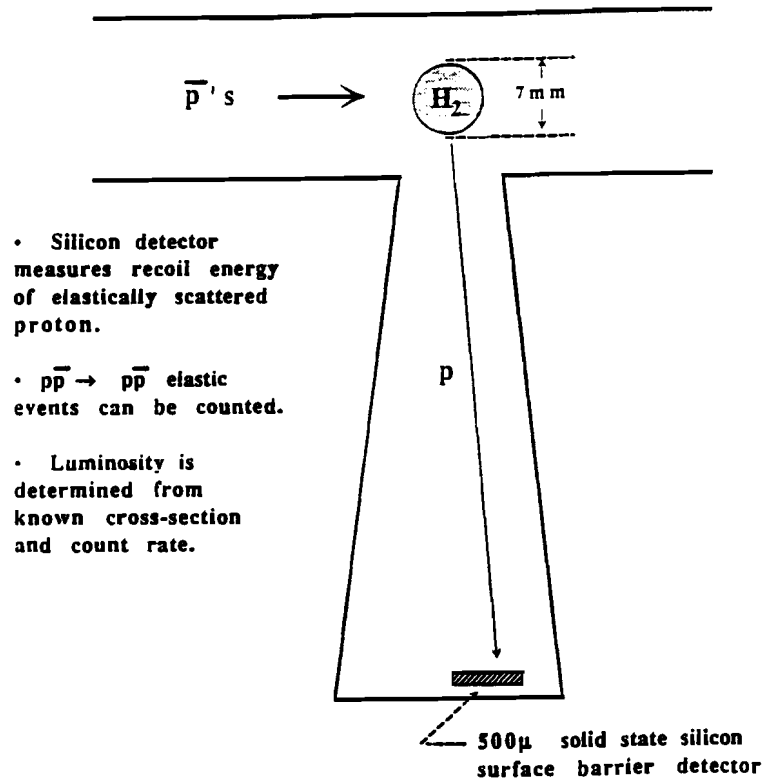

Figure 2.5: Schematic of the luminosity monitor.

A/R^2, the effective area of the detector divided by the square of the distance to the interaction point.

A typical pulse height spectrum from the fixed detector is shown in figure 2.6. Each measurement of the luminosity is typically taken over a 1-2 hour period and contained some $5 - 10 \times 10^5$ elastic scattering events. The spectra for each measurement are fit to an exponential background plus the expected spectrum shape to extract the number of elastic scattering events observed. By using the measurement time and the results of the fit, the luminosity can then be calculated. The measurement and fitting procedure result in a 3% statistical uncertainty in the luminosity.

The two dominant sources of systematic error come from the estimate of the effective detector area (A) and the value of the $\bar{p}p$ elastic scattering cross section.

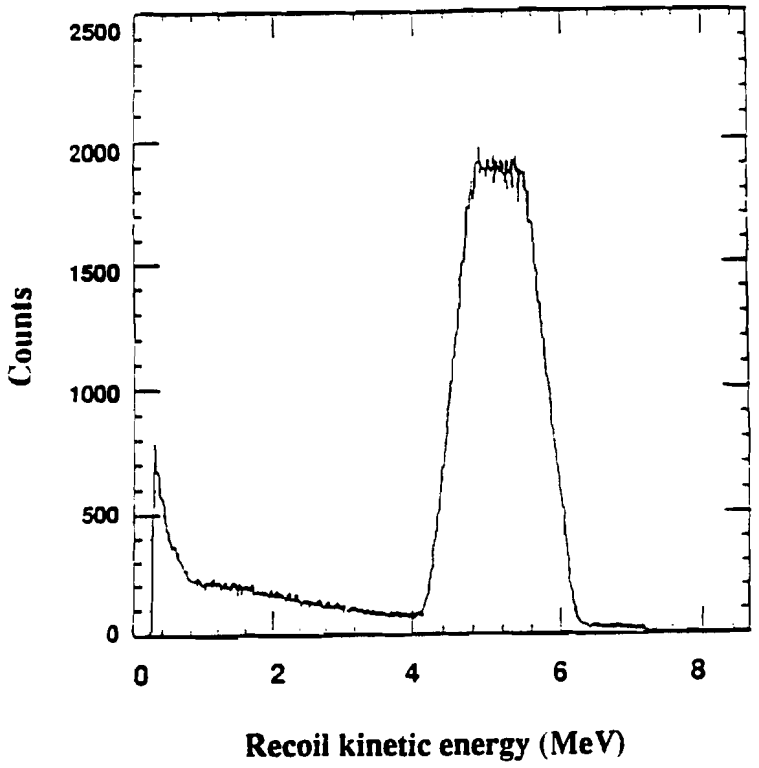

Figure 2.6: A typical luminosity monitor pulse height spectrum.

The error in the area of the fixed detector has been estimated by comparing the area (576 mm^2) given by the manufacturer to that predicted by a Monte Carlo simulation. By comparing the shape of the observed energy spectrum of the recoil protons (see figure 2.6) to that predicted by the Monte Carlo, the error in the area has been determined to be 2%. The error in $\frac{d\sigma_{elastic}}{d\Omega}$ is derived from the measurement uncertainties as reported in the literature. At the energies that concern E760, the error in $\frac{d\sigma_{elastic}}{d\Omega}$ is $\approx 2\%$.

The overall systematic error in the E760 luminosities reported in the dissertation is 4% while the statistical error is 3%. All luminosities reported are corrected for dead time caused by the data acquisition system. Typically the dead time is $< 6\%$.

2.4 The E760 Detector

The E760 detector (see figure 2.7) is a non-magnetic, large acceptance spectrometer with cylindrical symmetry about the beam axis. The central barrel has full azimuthal acceptance and polar acceptance from 12° to 70°, while the forward end-cap extends polar acceptance down to 2°. The detector has been optimized for detection of high-mass electromagnetic final states while still conforming to the extremely limited space avaliable inside the Accumulator tunnel.

The central detector is built out of a series of concentric cylindrical layers that begin at the Accumulator vacuum pipe. There are two sets of scintillator hodoscopes, H1 and H2 with 8-fold and 32-fold azimuthal segmentation respectively. The five central tracking chambers provide a redundant system necessary in the Accumulator environment since access to the inner components is all but impossible. The first chamber is made of two sets of straw drift tubes [33]. These aluminized mylar tubes are instrumented with a charge-division readout to give an azimuthal as well as a polar coordinate. Beyond the straw tubes is the inner tracking chamber which supports a radial projection chamber (RPC) and a separate multiwire proportional chamber (MWPC). The RPC provides up to 16 ionization measurements along charged tracks, while the MWPC with its transverse pad readout provides a second measurement of the longitudinal coordinate [34]. The outermost tracking elements are a barrel of Limited Streamer Tubes(LST) [35] with two layers and a planar multiwire proportional chamber in the forward direction with acceptance down to 12°. Between the inner and outer tracking elements is a threshold Čerenkov counter [36]

with the same 8-fold azimuthal segmentation as H1 and a 2-fold polar segmentation. The forward segment ($15° < \theta < 38°$) of the Čerenkov contains Freon13 at 1 atm while the backward segment ($38° < \theta < 65°$) contains CO_2 at 1 atm. The outermost component of the central detector is a lead glass electromagnetic Central Calorimeter (CCAL) [37] built out of 1280 towers that point to the interaction region. The calorimeter is segmented into 20 "rings" in the polar coordinate and 64 "wedges" in the azimuth.

The forward end-cap is instrumented with a scintillator hodoscope (FCH) that has 8-fold azimuthal segmentation. This is followed by three planes of straw tubes and a fine sampling Pb/scintillator Forward Calorimeter (FCAL) [38]. The Forward Calorimeter is made up of 144 towers that are individually read out through wavelength-shifter bars.

Because of their particular relevance to the analysis presented in this dissertation, a more detailed discussion of the hodoscopes H1 & H2, the Čerenkov, and the forward calorimeter are presented below. The following chapter will detail the central calorimeter.

2.4.1 Hodoscopes H1 and H2

The H1 hodoscope is segmented into 8 elements in the azimuthal angle ϕ_{lab} and completely surrounds the exterior of the 0.2 mm thick stainless steel Accumulator beam pipe. Each H1 element consists of a 2 mm thick NE102 scintillator that subtends the polar angle θ_{lab} between 9° and 65°. A single minimum ionizing particle

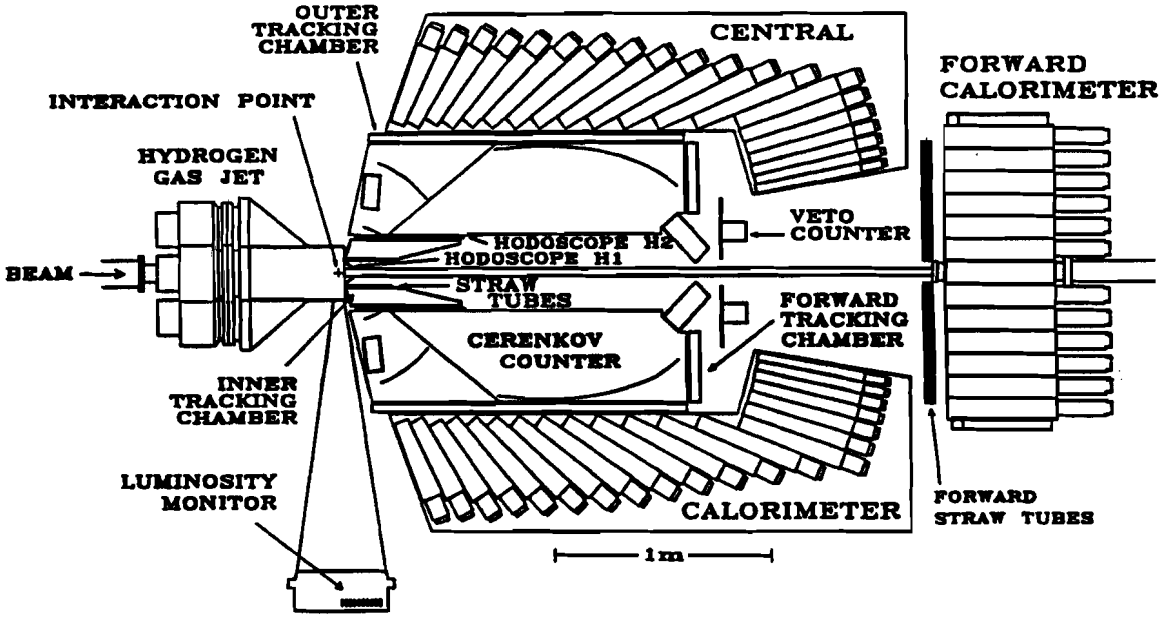

Figure 2.7: The E760 detector.

(mip) passing through H1 will typically yield an average of 10-20 photoelectrons.

The H2 hodoscope is located at a radius of 17 cm from the center of the beamline. Segmented into 32 ϕ_{lab} elements, the H2 counters are each 4 $mm \times 3\ cm \times 65\ cm$. Since a minimum ionizing particle passing through H2 will produce between 50 and 100 photoelectrons, the pulse height distribution can be used to separate single charged particles from e^+e^- pairs. Figure 2.8 shows the normalized (for path length) pulse height distribution for a sample of electrons from the reaction $J/\psi \rightarrow e^+e^-$ in mip units.

As discussed later in section 4.1.2, a coincidence between an appropriate H1 and H2 counter serve to define charged particle tracks at the trigger level. The threshold for the both the H1 and H2 hodoscopes are set at about 1/10th of the expected charge for a single mip. Both hodoscopes have been found to be fully efficient at detecting charged particles with the exception of the region between counters that form cracks. The consequences of the H1 and H2 cracks to the trigger efficiency are explored in section 4.2.1.

2.4.2 The Čerenkov

The gas Čerenkov [36] was built to select electrons from the decay of charmonium resonances. Since it is located between the interaction point and the central calorimeter, it had to be constructed out of light weight, low density materials so as not to spoil the calorimeter resolution. The Čerenkov also had to have a large acceptance and be very efficient so that it could be used in the trigger.

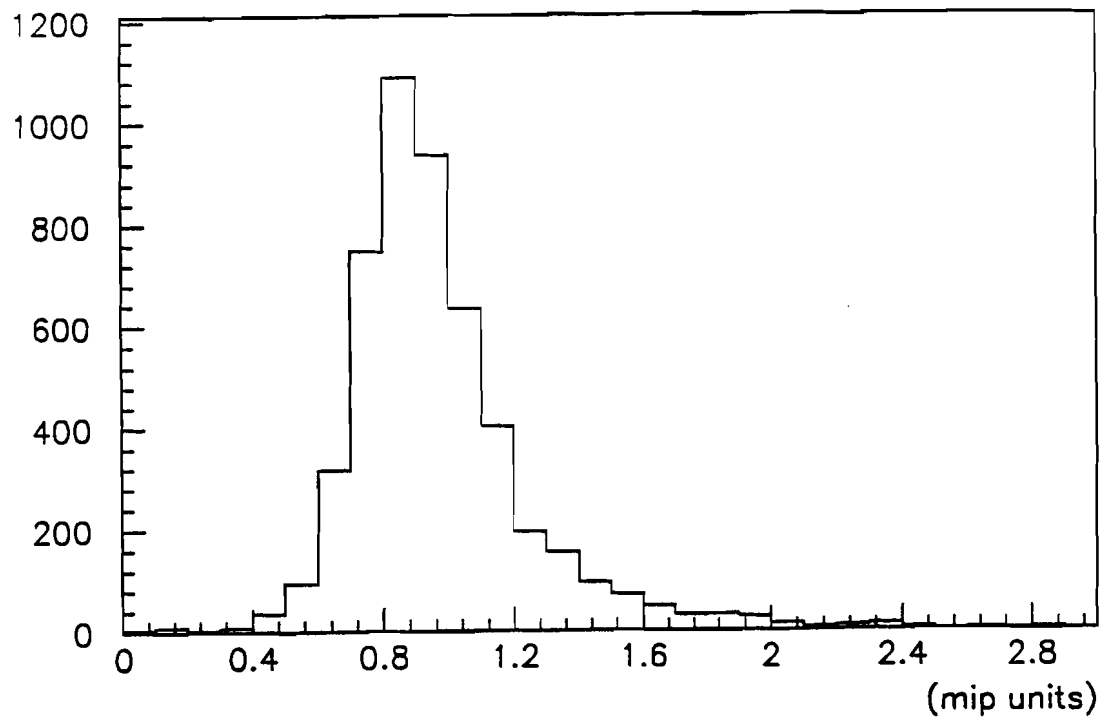

Figure 2.8: H2 pulse height in normalized mip units for electrons from J/ψ decays.

The Čerenkov was designed to operate at atmospheric pressure, although no single radiator would provide adequate hadron rejection over the entire polar acceptance range of $\theta_{lab} = 15°$ to $\theta_{lab} = 70°$. The final design solved the hadron rejection problem by introducing a 0.3 mm thick aluminum septum at $\theta_{lab} = 38°$, thus dividing the Čerenkov into "small angle" ($15° < \theta_{lab} < 38°$) and "large angle" ($38° < \theta_{lab} < 70°$) cells that could be filled with different radiator gases. The small angle cell is filled with Freon13 while the large angle cell is filed with CO_2. This choice of radiator gases was motivated by the need to reject charged pions while still allowing for the detection of electrons. Only pions with $\sqrt{s} > 3.4\ GeV$ in the small angle cell and $\sqrt{s} > 5.8\ GeV$ in the large angle cell were detected. In order to accommodate a reasonable optical system, the Čerenkov is segmented into eight

separate ϕ chambers. This choice of ϕ_{lab} segmentation is identical to that of the Hodoscope H1, thus allowing easy incorporation of the Čerenkov into the trigger. Figure 2.9 shows one of the ϕ_{lab} segments of the Čerenkov.

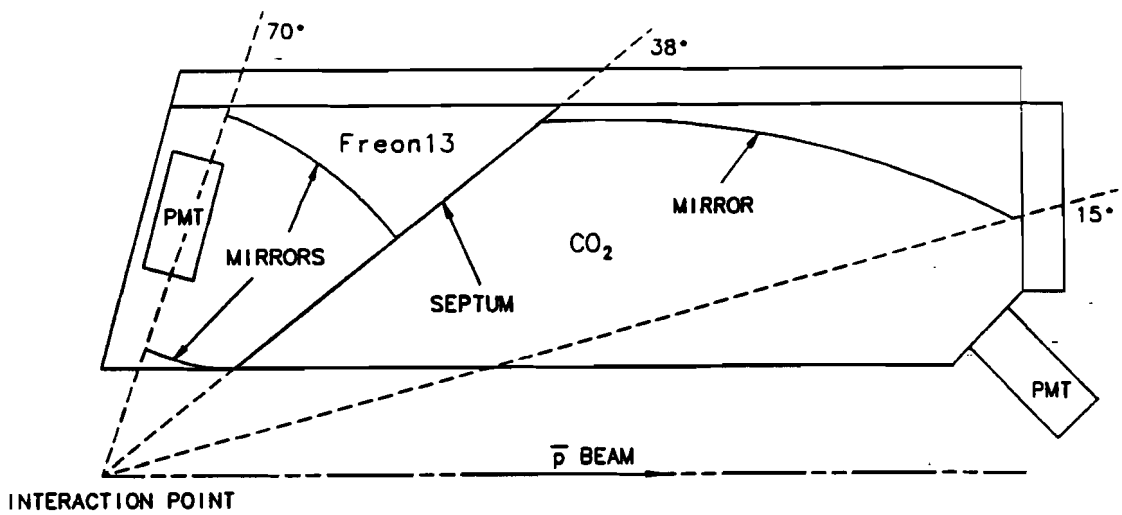

Figure 2.9: Schematic of the Čerenkov.

The optical system implemented in the Čerenkov takes advantage of the small interaction region. The large angle cell uses a spherical mirror to focus the light onto a smaller plane mirror which then reflects the light onto a photomultiplier tube (PMT). The small angle cell utilizes a single ellipsoidal mirror to focus the light directly onto a PMT. All PMTs used in the Čerenkov are 2 *in* diameter Hamamastu R1332Q tubes with fused silica windows. These PMTs provide excellent response to light with wavelengths as short as 200 *nm* and risetimes of 2-3 *ns*. The photoelectron yield is in general a function of the angle θ_{lab} due to the variation in the pathlength

traversed by the electron in the radiator. From a sample of 10,000 electrons (from the reaction $J/\psi \rightarrow e^+e^-$) it has been determined that the minimum number of photoelectrons seen for any angle θ_{lab} away from the septum is about 6 (pe). Since the threshold for detection of electrons was set at 1/2 (pe), the Čerenkov should have been fully efficient for electrons that were not near the septum. The efficiency for the detection of electrons near the septum is discussed in more detail in section 4.2.4.

2.4.3 The Forward Calorimeter

The forward calorimeter (FCAL) [38] covers the region from $\theta_{lab} = 2°$ to $\theta_{lab} = 12°$. This region was separated from the central calorimeter because of the expected high rates and high levels of radiation near the the beam pipe. The FCAL is composed of a 144 module array (see figure 2.10) that is stacked into a wall to form a forward end plug for the E760 calorimeter system. Each module is composed of a series of 148 alternating layers of lead and plastic scintillator (see figure 2.11). The scintillation layers are read out by a single wavelength shifter bar placed on one side of the lead-scintillator stack. A photomultiplier tube is attached to the wavelength shifter bar to complete the module. The energy resolution of the forward calorimeter has been determined [38] to be:

$$\frac{\sigma}{E} = \left[\left(\frac{0.08}{\sqrt{E(GeV)}} \right)^2 + (0.068)^2 \right]^{1/2} . \tag{2.9}$$

Despite the relatively coarse segmentation of the FCAL, a position resolution of 3 cm has been achieved for photons $> 1\ GeV$.

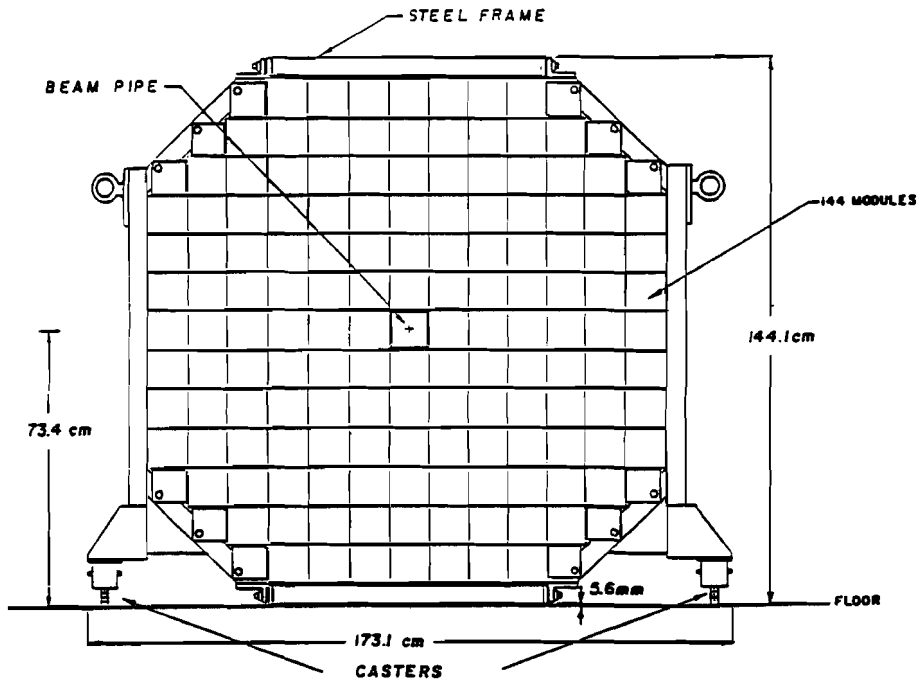

Figure 2.10: Beam view of the 144 module forward calorimeter.

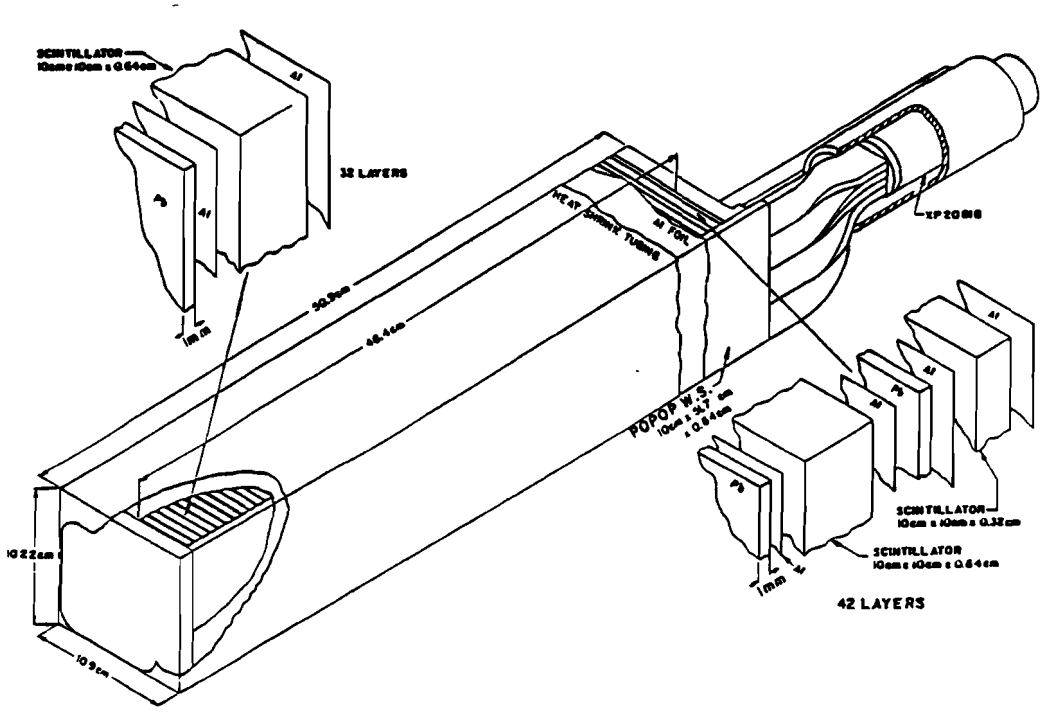

Figure 2.11: Schematic of a forward calorimeter module.

Chapter 3

The Central Calorimeter

The E760 central calorimeter (CCAL) [37] is a 1280 block lead glass electromagnetic calorimeter. The CCAL utilizes a pointing geometry and is cylindrically symmetric about the beam pipe. The very small interaction region in E760 combined with the CCAL's pointing geometry allow CCAL topological inputs into the first level trigger. This allows E760 to efficiently extract interesting events from the enormous total interaction rate of $\sim 1\ MHz$.

3.1 Design and Construction

The primary consideration in the design of the central calorimeter was the need to distinguish between γ's from the various charmonium decays and those produced from multipion reactions, in particular $\bar{p}p \rightarrow 2\pi^0 \rightarrow 4\gamma$. The photons from $2\pi^0$ decays can simulate the topology of 2γ decays from charmonium in two ways. In the first case, the π^0's can decay symmetrically producing two photons that have a very small spatial separation and may appear as a single γ in a detector. In the second case, the π^0's may decay asymmetrically producing a photon that carries

most of the π^0's initial energy and a second low energy photon that may be below the detection threshold.

One can conceive of a calorimeter that would deal with the problem of identifying both the symmetric and asymmetric decays of the π^0. For example, in order to detect the symmetric decays one would design a calorimeter that is far from the interaction region and has a very fine segmentation. In this way the two photons from a π^0 decay would always be resolvable. In order to deal with the asymmetric decays, one could design a calorimeter with complete 4π coverage of the solid angle with a very low energy threshold so that the low energy photons would always be observed. Unfortunately, such an ideal calorimeter is not practical since the cost would have been prohibitive.

The first design decision made was to construct a calorimeter with a pointing geometry (see figure 3.2). The pointing geometry allows for the use of calorimeter information at the trigger level to suppress the enormous neutral event rate. In order the determine the optimum combination of segmentation, energy resolution, position resolution, solid angle coverage, and distance from the interaction region given the constraints of cost and avaliable space, a series of Monte Carlo simulations were conducted. The Monte Carlo results showed that adequate suppression of the asymmetric π^0 background could be achieved with a low energy threshold around 50 MeV and that good energy resolution provided more suppression than good position resolution. For the symmetric decays, the Monte Carlo showed that only a modest segmentation was required.

So with the basic design parameters in mind, the next choice to be made was which materials to use. The constraints on the material choice, in addition to those above, were that the pulses generated had to be fast and the material had to reasonably radiation hard. Lead glass was selected because it not only met all the criteria but was also relatively easy to handle and to manufacture, and was reasonably inexpensive.

The specific type of lead glass selected was chosen to maximize light output especially for low energy photons. Five lead glass samples from three manufactures were tested at the Tagged Photon Facility at the University of Illinois Nuclear Physics laboratory (UINPL) for their response to low energy photons. The results of the study (shown in figure 3.1) indicated that the F2 and F2W glasses gave more light than the SF5 glasses. This result was expected since the SF5 glasses were known to have a much shorter path length for electrons than the F2 and F2W glasses. The longer path length for electrons in the F2 and F2W glasses more than made up for their somewhat smaller index of refraction. The Schott F2 glass (see table 3.1) was chosen for use in the E760 calorimeter because of its superior light output, good transmittance, and modest cost . The radiation hardness of the F2 glass was tested using a 40 *cm* test sample and a ^{137}Cs source. It was found that the transmittance to 400 *nm* light was reduced by a factor 2 after a single dose of 300 *rad*. Since the total expected radiation dose from the Accumulator environment was expected to be only about 300 *rad* over the entire 2 year running time, the F2 glass would be sufficiently radiation hard since the glass would have time to recover transmittance

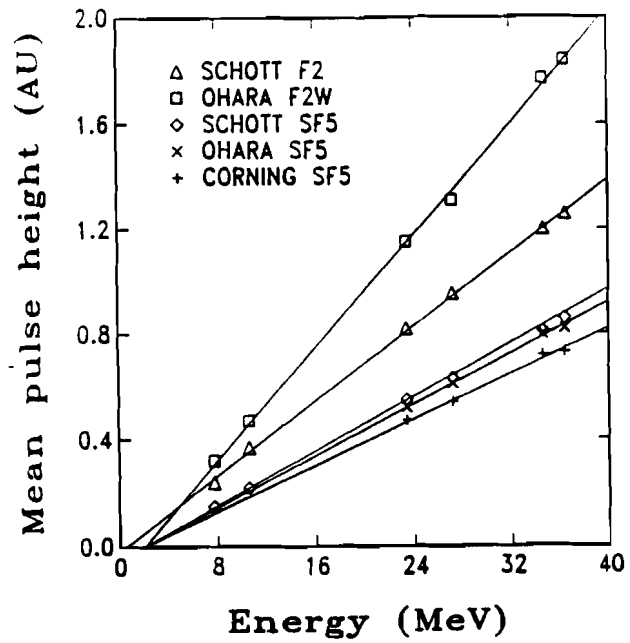

Figure 3.1: Mean pulse height distributions for the five lead glasses tested at UINPL. between doses [39].

With the F2 glass chosen, it was time to go back to the Monte Carlo to work out the final details of the design. It was found that in order to achieve the maximum background rejection, one could give up some energy resolution by making the blocks only long enough to contain 90%-95% of the electromagnetic shower energy, and thus improve the sensitivity to low energy photons. The added sensitivity to low energy photons in short blocks was due to reduced losses in light transmission (see table 3.1 for final block lengths). The final segmentation was also determined from a Monte Carlo simulation. The criteria imposed on the segmentation was that at the highest conceivable formation energies, symmetrically decaying $\pi^0 s$ should still be resolvable. This led to the final segmentation (shown in figures 3.2 and 3.3 and

Radiation Length	3.141 cm
Density	3.61 g/cm^3
Refractive Index at 404.7 nm	1.651

Composition By Weight:	
Lead	42.2%
Oxygen	29.5%
Silicon	21.4%
Potassium	4.2%
Sodium	2.3%
Arsenic	0.15%

Transmittance Through 10 cm of Glass:	
Wavelength (nm)	Transmittance
335-344	56.9%
385-394	95.5%
435-444	97.9%
485-494	98.4%
535-544	98.9%
585-594	99.4%

Table 3.1: Characteristics of the lead glass used in the E760 central calorimeter, Schott F2 lead glass.

detailed in table 3.1) which was chosen to be 64 blocks in the azimuthal angle ϕ covering the range $\phi_{lab} = 0°$ to $\phi_{lab} = 360°$ and 20 blocks in the polar angle θ covering the range between $\theta_{lab} = 10.6°$ and $\theta_{lab} = 70°$.

Block Number	Length (L_R units)	$\Delta\theta$ (degree)	$\Delta\phi$ (degree)	Distance from target[a](cm)	Fractional PMT coverage
1	12.03	5.226	5.625	72.44	0.473
2	12.30	5.031	5.625	75.87	0.475
3	12.70	4.803	5.625	80.07	0.476
4	13.21	4.552	5.625	85.08	0.478
5	13.86	4.284	5.625	90.96	0.479
6	14.65	4.007	5.625	97.79	0.481
7	15.59	3.728	5.625	105.62	0.482
8	15.92	3.451	5.625	114.54	0.497
9	15.92	3.183	5.625	124.66	0.520
10	15.92	2.925	5.625	136.07	0.544
11	15.92	2.679	5.625	148.89	0.568
12	15.92	2.449	5.625	163.26	0.593
13	15.92	2.233	5.625	179.34	0.617
14	15.92	2.033	5.625	197.28	0.641
15	15.92	1.848	5.625	197.29	0.546
16	15.92	1.678	5.625	197.29	0.664
17	15.92	1.522	5.625	197.30	0.527
18	15.92	1.380	5.625	197.30	0.644
19	15.92	1.250	5.625	197.30	0.443
20	15.92	1.131	5.625	197.30	0.543

[a] to front face of block

Table 3.2: Dimensions and positions of the lead glass blocks in a wedge.

The last non-mechanical design decision was the choice of photomultiplier tubes (PMT). The PMTs were chosen to maximize the collection of light, to provide a linear output within the dynamic range of the experiment, to be relatively immune to small magnetic fields, and to have gains that are compatible with the FERA ADC system. To maximize the light collection efficiency, PMTs of four diameter

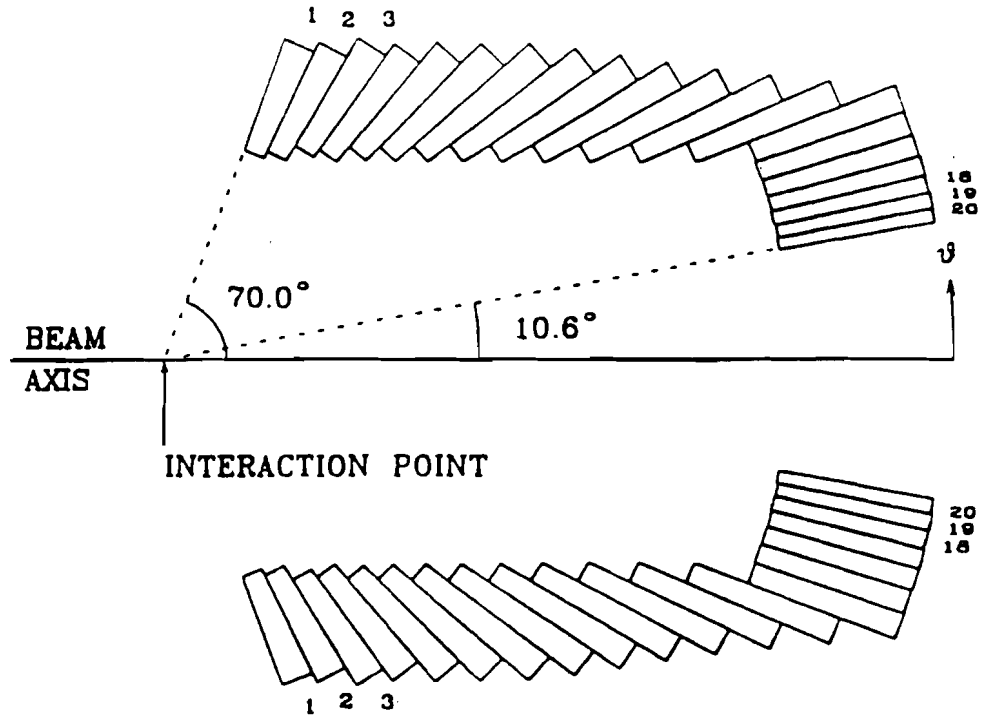

Figure 3.2: The CCAL showing the θ segmentation.

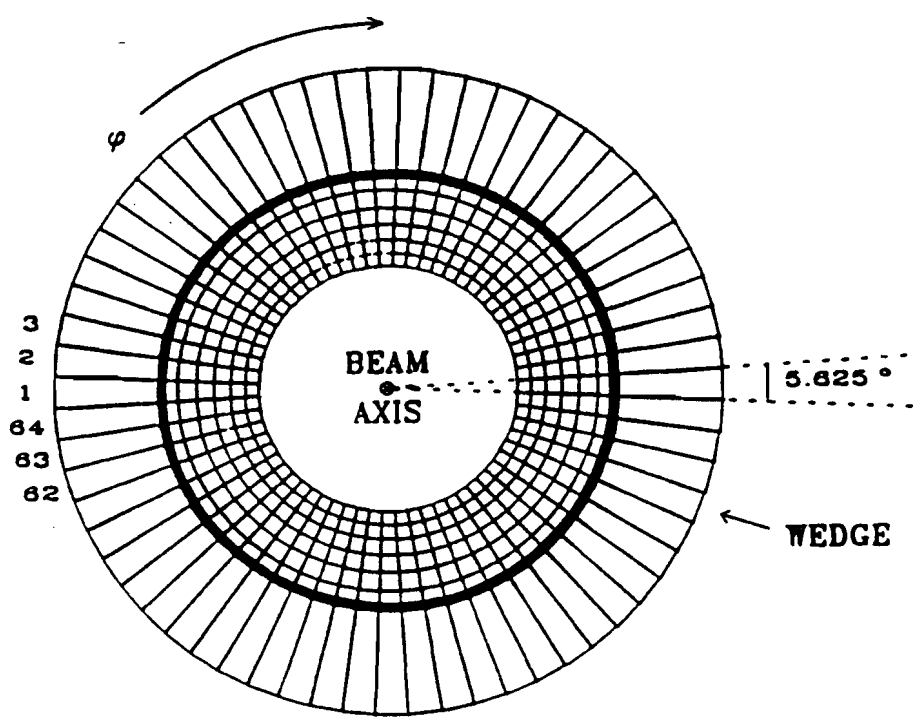

Figure 3.3: The CCAL showing the ϕ segmentation.

sizes (1.5, 2, 2.5, and 3 *in*) were used in order to match as closely as possible the area of the PMT to the area of the back end-face of each size lead glass block (see table 3.1). Three manufactures (Amperex, EMI, and Hamamatsu) provided 3 *in* diameter linear focused PMTs for evaluation. It was found that only the EMI D640 and the Hamamastu R3036 would meet the above requirements and eventually Hamamatsu won the competition to supply all the $\sim$ 1400 (1280 plus spares) PMTs for the E760 CCAL. The 2.5 *in* R3345 PMTs provided by Hamamastu were essentially the same as the R3036 but with a smaller glass envelope. Unlike the R3036 and R3345 PMTs which were specifically designed and manufactured for E760, the 2 *in* (R2154) and 1.5 *in* (R580) tubes were selected from the Hamamatsu catalog. Table 3.3 summarizes some of the characteristics of the PMTs used in the CCAL.

Photocathode Material		Bialkali	
Window Material		Borosilicate Glass	
Dynode Structure		Linear Focused	
Sensativity Range		300-650 *nm*	
Peak Sensitivity		420 *nm*	
Quantum Efficiency (at 450 *nm*)		0.015	
Model Number	Number of Dynodes	Diameter (in.)	Length (in.)
R3036-02	12	3.0	5.0
R3345-02	12	2.5	5.0
R2154-04	10	2.0	6.0
R580-13	10	1.5	6.0

Table 3.3: Characteristics of the Hamamatsu photomultiplier tubes used in the E760 central calorimeter.

The PMTs in the E760 CCAL operate using positive high voltage with a bleeder current of approximately 200 μA. In order to assure robustness of the PMT/base

assembly, all PMTs were supplied with base circuits as integral assemblies on a single board. Figure 3.4 shows the diagram for the bases used on the 2.5 and 3 *in* PMTs. The bases for the 1.5 and 2 *in* PMTs were similar to the one shown in figure 3.4. except that the smaller PMTs had 10 dynodes instead of 12. One last point about the PMTs used in the CCAL is that they have a relatively slow rise times (6-10 *ns*). A slow rise time is the trade-off for excellent photoelectron collection. Fortunately, timing information to several *ns* is not important in this part of E760.

3.1.1 Construction

A block assembly is comprised of a lead glass block, a PMT, a μ-metal shield, a fiber optic connector, and a white paper wrapping. In order to assure long term stability (both mechanical and optical) the PMTs were glued directly to the lead glass blocks using a semiflexible epoxy, Epotek 301. In addition to being semiflexible, this epoxy has an index of refraction ($n = 1.538$) that approximately matches that of the lead glass while also providing excellent light transmission above 320 *nm*. The fiber optic connector was mounted along side the PMT at the back of the block (see figure 3.9). To complete the assembly a μ-metal shield was wrapped around the PMT and white paper was tightly wrapped around the block. The purpose of the paper was to provide a mechanical cushion for the block. After the block assemblies were put together, they were tested and calibrated (see section 3.2) before being assembled into "wedges".

Every 20 block θ array is an independent mechanical and electrical unit called

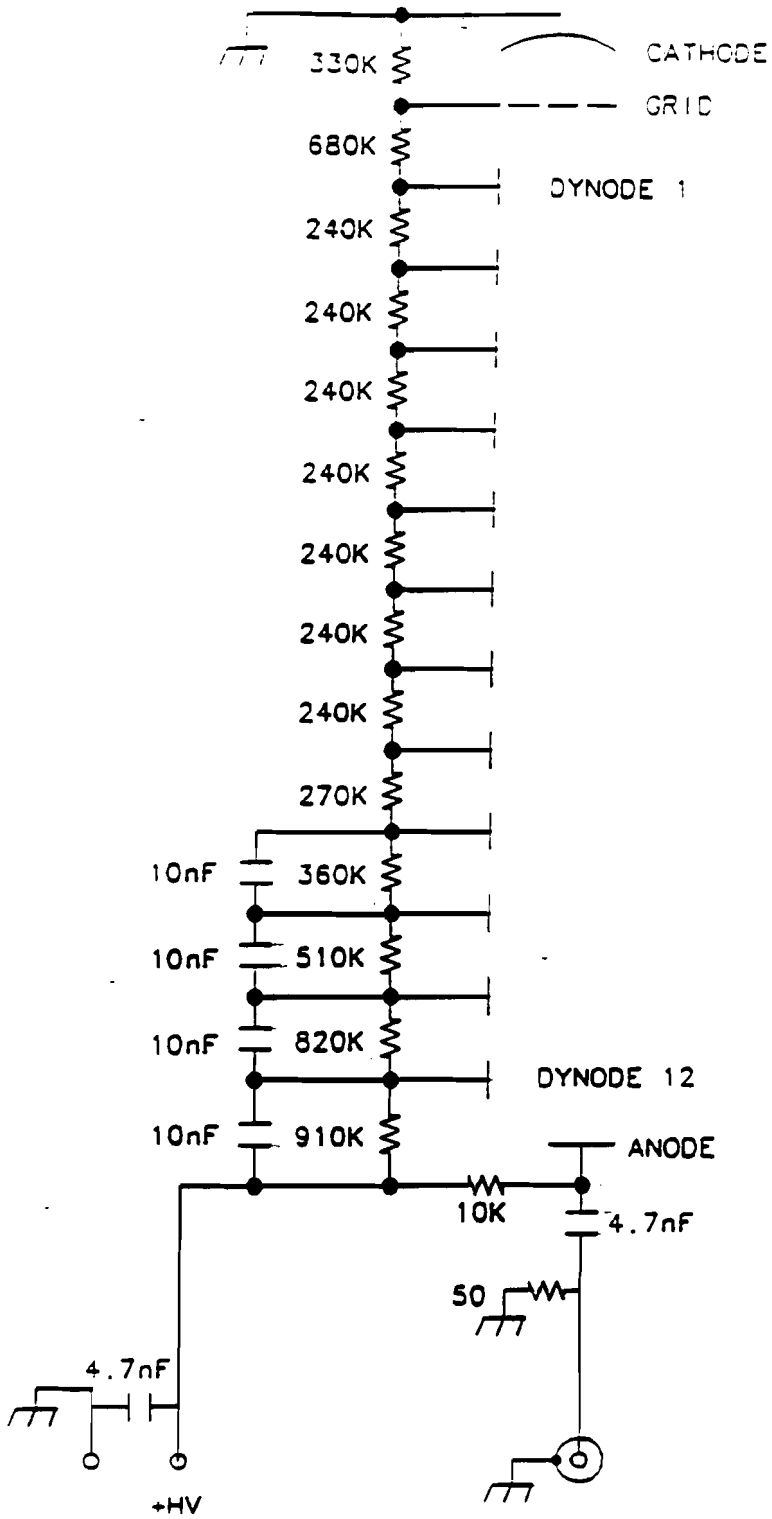

Figure 3.4: Base diagram for the 2.5 and 3.0 *in* PMTs. Bases for the 1.5 and 2.0 *in* PMTs are similar with the exception that they have only 10 dynodes.

a wedge. Shown in figure 3.5, each wedge is a light-tight stainless steel shell. The plates between blocks in θ (fins) are made of 0.254 mm stainless steel sheets while the outer surfaces that become the separations in ϕ (skins) are made of 0.735 mm sheets of stainless steel. The design of the wedges had two competing interests; on the one hand, the entire structure must be rigid and stable, while on the other hand too much material between blocks would degrade the energy resolution and lead to inefficiency in photon detection. In the final design the skins account for about 2% of the material in ϕ while the fins account for about 0.5% of the material in θ. All components in the wedge assemblies including the glass blocks themselves were machined to very tight tolerances, typically 0.08 mm or less. Every assembled wedge was tested for light tightness, electrical integrity, and optical response to the fiber optic system.

As the name might imply, the calorimeter wedges fit together very much like wedges in an orange. The fully completed wedges were mounted on the calorimeter support structure one at a time. The mounting started at the bottom and subsequent wedges were added on alternate sides. In this way the compressional loading on the bottom wedges could be carefully controlled. Each completed wedge weighed about 500 *lbs* and, if dropped while being installed, could have easily destroyed all of the other wedges already mounted. Fortunately no such accidents occurred. At this point one can see why the tolerances on the wedges and the glass components were so tight. In this mechanical assembly the glass itself becomes a structural element carrying a compressive load. If there had been significant inter-block gaps,

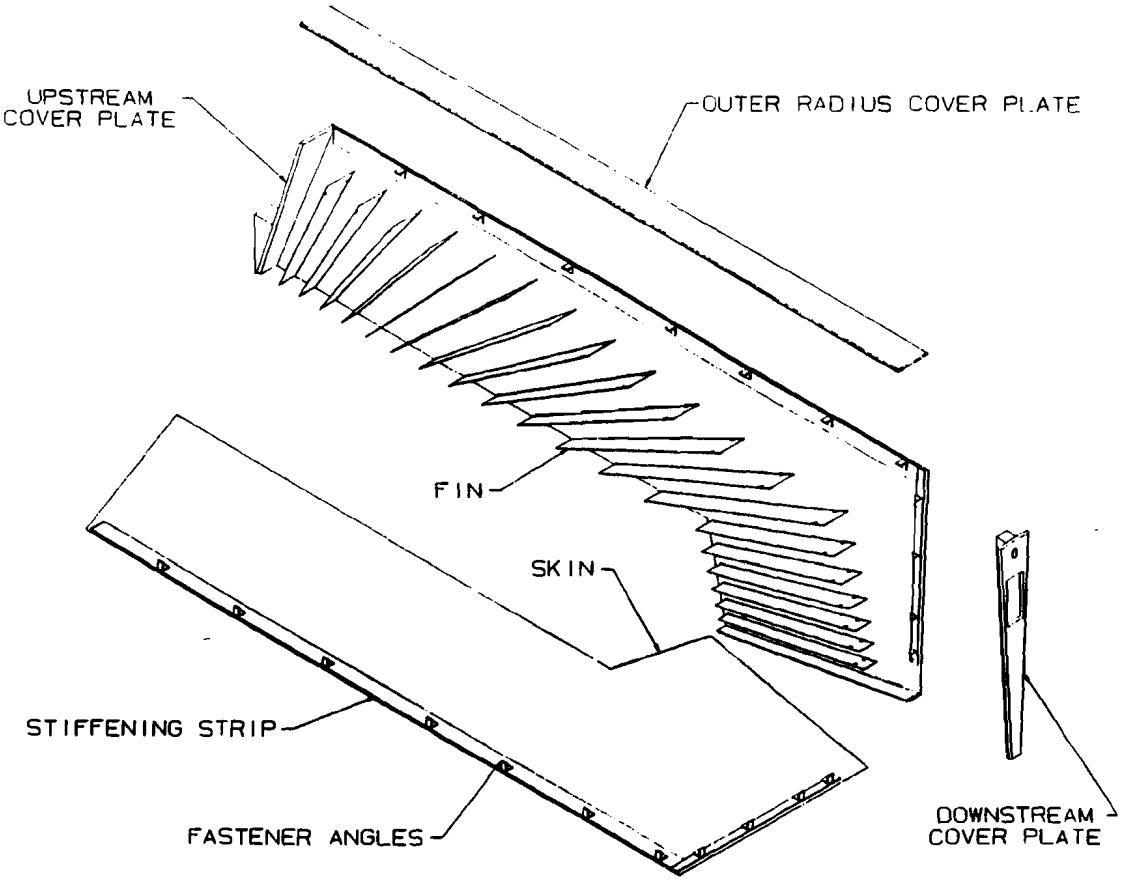

Figure 3.5: A cut-out view of a wedge.

tensile stress due to bending of the blocks would have been introduced. The design tolerances did not allow the blocks to be subjected to tensile stresses that exceeded 1.04×10^7 *Pascals*. The ultimate strength of glass is $\sim 5 \times 10^7$ *Pascals*.

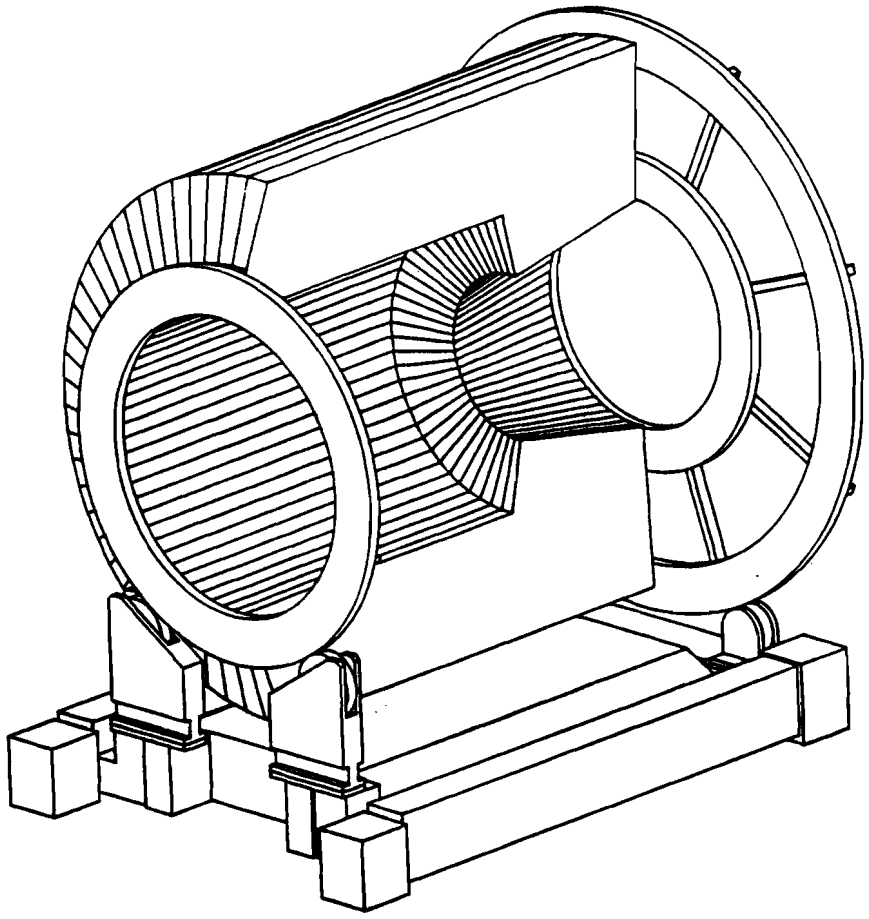

Figure 3.6: Diagram of the calorimeter and its support structure.

Once the calorimeter was fully assembled and mated to the inner detectors, it was transported from the assembly area to the Accumulator by flatbed truck. The entire assembly at this point weighed approximately 25 *tons*. Once inside the Accumulator tunnel the calorimeter and inner detectors were connected to the gas jet target and gingerly maneuvered into position on the beamline. The entire 25 *ton* assembly is

moved within the experimental area by mean of an air caster system that literally lifts the entire detector on a cushion of air. The final precision alignment is done by using four motorized screw jacks and eight hydraulic cylinders. The entire E760 detector can be aligned to an impressive accuracy of ± 0.0051 *cm*. Once in place the exterior electrical and fiberoptic connections are made to each wedge through a patch panel on the downstream side (see figure 3.5).

3.2 Initial Testing and Calibration

The goals of the initial testing and calibration were two-fold. Firstly, it was desirable to find all the marginal calorimeter modules prior to their installation into the calorimeter. Once installed into the calorimeter, a module could not be removed without removing the entire detector from the beamline. Secondly, a good initial calibration makes the problem of obtaining an *in situ* calibration much simpler.

3.2.1 Photomultiplier Tube Gain Curves

Measurements of the PMT gain curves were incorporated into the acceptance tests that were conducted as PMTs arrived from the manufacture. In order to test the 1500 tubes in a timely manner, a testing facility was set up that could process 45 PMTs per day. The test facility consisted of a rack which could hold up to 48 tubes and a Xenon flashlamp as a light source. In order to measure the relative response of the PMTs tested, the relative intensity of light falling on each slot had to be known. The relative light intensity of each slot was measured by two moving

"monitor" tubes. The two moving monitor tubes repeatedly tested the slots over the 3 month testing period to make sure that the relative light intensity between slots did not change. To measure the pulse-to-pulse light intensity variations of the flashlamp a fixed (fixed in the rack and operating at a fixed voltage) monitor tube was used.

The testing procedure was straightforward. Each afternoon 45 PMTs were loaded into the rack (48 slots less one for the fixed monitor and two for the moving monitors). The testing began by ramping the tubes up to 2000 V in order to check for electrical break downs. After 2 hours at 2000 V the PMT voltages were lowered to 1500 V and allowed to stabilize for an hour. Using the known relative light intensity for each slot, the voltage for each tube was then adjusted so that each tube would produce the same output per unit incident light. Gain curves for each tube were then constructed by stepping the voltage through a 200 V range centered on the voltage determined in the previous step. The entire testing procedure took about 6 hours per batch.

3.2.2 Initial Calibration with Muons

The goal of the initial calibration was to set the gains on all the modules such that a 5 GeV electron shower would produce 2000 pC at the PMT anode. Ideally the initial calibration would have been done at a test beam facility Unfortunately it was not reasonable to test all 1280 modules in an electron beam given the time constraints of the experiment. Since it was essential to have at least some nominal

calibration in place when the detector was installed, we decided to use cosmic ray muons (μ). The problem with μs is that they are minimum ionizing particles and do not produce electromagnetic showers in the lead glass. To solve this problem 60 modules (3 of each shape) were taken to Brookhaven National Laboratory (BNL) and placed in a beam that contained e^-s and π^-s.

By using a threshold Čerenkov counter and a series of scintillator paddles, e^-s and π^-s could be selected from the BNL test beam. It was then possible to determine the response of each module to e^- showers and to minimum ionizing π^-s. The idea was that if we could determine the ratio $\frac{\pi^-}{e^-}$ for each shape module, then we also know the ratio $\frac{\mu}{e^-}$ since $\frac{\mu}{\pi^-}$ could be reliably calculated. The ratio $\frac{\mu}{\pi^-}$ was calculated using a Monte Carlo simulation and was found to be independent of block shape and equal to $\frac{\mu}{\pi^-}$=0.85 for 3 GeV π^-s and sea level cosmic ray μ. The $\frac{\mu}{\pi^-}$ ratio was also experimentally checked with a small set of blocks tested both at BNL and at Fermilab. The calibration was transferred from BNL to Fermilab by using Bi^{207} pulsers (described in section 3.4) as an absolute calibration reference. The Monte Carlo and experimental determination of the $\frac{\mu}{\pi^-}$ ratio were consistent. The results of the BNL study are summarized in table 3.2.2.

Once the $\frac{\mu}{e^-}$ ratios were known then the response of every module could be calibrated by using μs. A testing and calibration program was set up at Fermilab as an integral part of the CCAL assembly process. The calibration was conducted using four dark-boxes that were designed to hold 6 modules vertically in each. Above and below each test station was a pair of scintillator paddles. μs that would pass

Shape	$\frac{\mu}{e^-}$ ratio
1	0.1012
2	0.1021
3	0.1060
4	0.1058
5	0.1189
6	0.1191
7	0.1318
8	0.1348
9	0.1347
10	0.1382
11	0.1383
12	0.1377
13	0.1361
14	0.1366
15	0.1418
16	0.1399
17	0.1427
18	0.1406
19	0.1557
20	0.1448

Table 3.4: $\frac{\mu}{e^-}$ as determined at BNL.

through the entire length of the module being tested could be tagged by using a coincidence between these paddles (see figure 3.7). As modules were assembled they were tested in the dark-boxes for a period of about 18 hours. Figure 3.8 shows a typical μ spectrum. In order to monitor the stability of the testing apparatus, two monitor tubes were employed. As in the PMT gain tests, one of the monitor tubes was kept fixed in the same slot for the duration of the testing and the other monitor module was systematically rotated through all the testing stations.

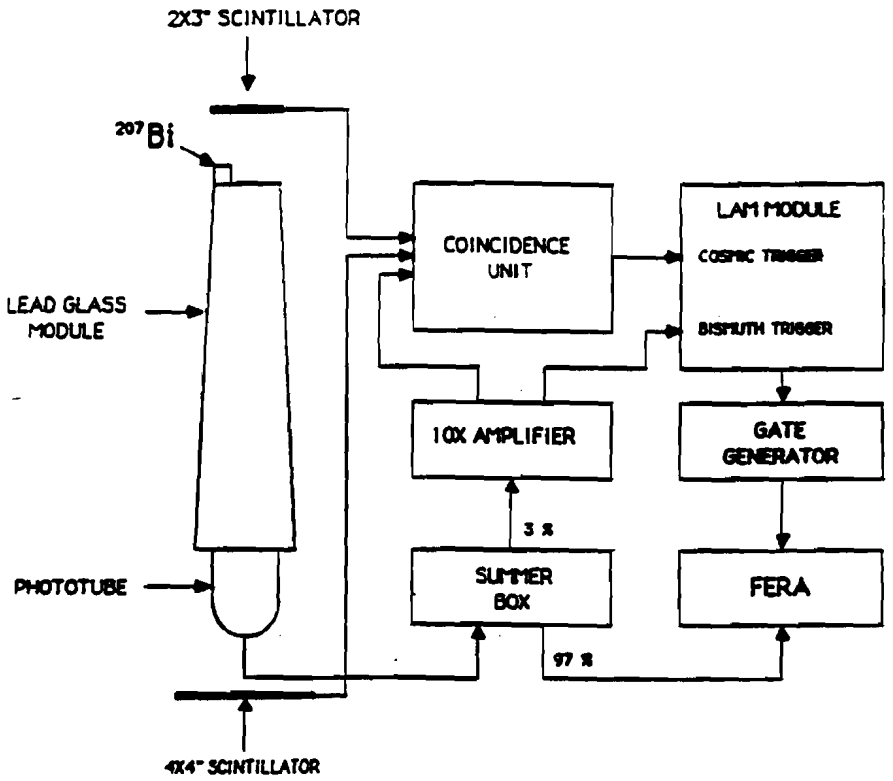

Figure 3.7: Diagram of the μ testing apparatus.

The operating voltages for each module were determined by an iterative procedure. One could use the BNL results and the gain curve for a particular PMT to estimate the operating voltage of a module. Using this intial voltage the μ test was conducted. If the result of the μ test was within 20% of expectation then the

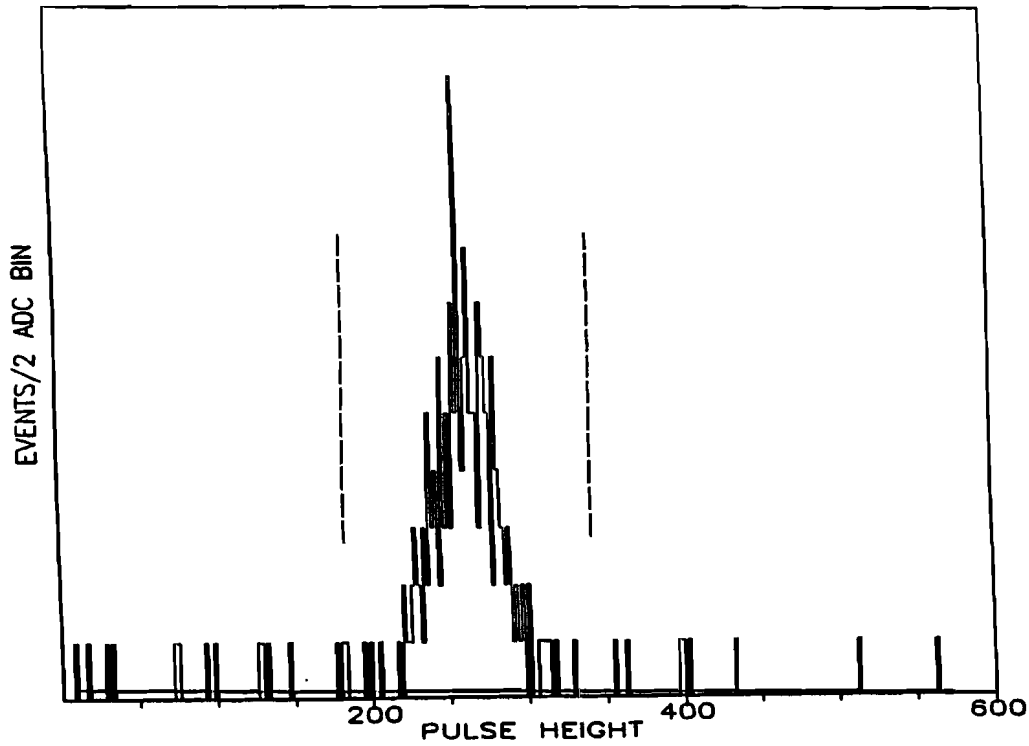

Figure 3.8: A typical spectrum from cosmic ray μs.

operating voltage for that module was set using the relation:

$$V = V_{initial} \left[\frac{\mu_{observed}}{\mu_{expected}} \right]^{\frac{1}{m}}, \tag{3.1}$$

where m is slope of the gain curve as determined for that PMT during the gain testing. If the results of the μ test were more than 20% off, then a new initial voltage was calculated using equation 3.1 and the module was retested. Fewer than 10% of the modules required a second test and none of the modules required a third. It was expected that this procedure would set the gains of all the modules to within 4% of each other. A comparison with the *in situ* calibration showed that the actual gains had a 6.6% rms spread. This was rather impressive since the final installation contained many variabilities that could not be simulated during the μ testing.

3.3 *In Situ* Calibration

Although the initial calibration was very good, it could not account for all the channel-to-channel variations of the final installation. The source of variations included such things as cable losses and ADC pedestals, to name just two. Further, even if a perfect initial calibration was achieved, one could expect the gains to drift over time so an *in situ* calibration would have still been required.

For the 1990 data, the energy calibration was obtained by reconstructing $J/\psi s$ from the reaction $\bar{p}p \rightarrow J/\psi \rightarrow e^+e^-$. The expected energy ($E_j$) deposited in the CCAL from the jth J/ψ event could be predicted by using two body kinematics. The measured energy (M_j) deposited in the CCAL for j^{th} J/ψ event is given by,

$$M_j = \sum_{i=1}^{n} g_i A_{ij} \tag{3.2}$$

where g_i is the gain constant associated with the ith module and $A_{i,j}$ is the response (in ADC counts) of the ith module to the jth event. To find the gain constant g_k one can use an iterative procedure. The derivative with respect to g_k of the function

$$\chi^2 = \sum_{j=1}^{N} \frac{(M_j - E_j)^2}{\sigma_j^2}, \tag{3.3}$$

is set to zero and solved for g_k to give:

$$g_k = \frac{\sum_{j=1}^{N}[A_{kj}/\sigma_j^2][E_j - \sum_{i=1,i\neq j}^{n} A_{ij}g_i]}{\sum_{j=1}^{N}[A_{kj}^2/\sigma_j^2]}. \tag{3.4}$$

The quantity σ_j is the estimated error in the predicted energy. For each iteration the gain constants from the previous iteration are used in the right hand side of equation 3.4. The procedure is repeated until the resulting gains converge to a

stable value. The iteration procedure works very well and converges quickly as long as each module has about 3 hits and the block-to-block variation in the gains does not exceed $\sim 20\%$.

The problem with using J/ψ events to calibrate the CCAL was the limited statistics. During the first several weeks of the 1990 data run, some 5000 $\bar{p}p \rightarrow J/\psi \rightarrow e^+e^-$ events were collected intermittently. Normalizations from the gain monitoring system (described in section 3.4) were used so that the data collected over several weeks could be combined to extract a set of calibration constants. Once the calibration was known at some time t_0, then the calibration could be found at any time t by using the normalization constants from the gain monitoring system. The eventual problem was that small errors in the normalizations from the gain monitoring system added up over time and caused the calibration to drift. The solution to the problem was to return the J/ψ every 4 weeks to restore the calibration. This had the obvious effect of reducing the amount of running time available to study other resonances.

In 1991 the calibration problem was solved by using events from the reaction $\bar{p}p \rightarrow \pi^0\pi^0$ which are produced in copious quantities. The $\pi^0\pi^0$ calibration was carried out in exactly the same way as the J/ψ calibration with the extra complication that each π^0 had to be reconstructed from the angles of the decay photons in the CCAL. Once the directions of the $\pi^0 s$ were reconstructed their energies could be calculated using 2-body kinematics. The $\pi^0\pi^0$ events were so numerous that many thousands of them could be collected every day, allowing for the determination of

new calibration constants every week. The energy calibration constants determined from the $\pi^0 s$ were accurate to about 0.5%.

3.4 Gain Monitoring System

In order to track the CCAL counter gains between calibrations, a gain monitoring system was developed which used a single Xenon flashlamp as a light source and plastic polymer fiber optic cables to distribute the light to all 1280 channels (see figure 3.9). The xenon flashlamp produced a 300 ns long pulse whose spectral output peaks at a wavelength of ~400 nm. The light was collected by an elliptical reflector and focused into a rectangular lucite mixing bar. A filter wheel allowed selection of a neutral spectrum or blue and green components. The mixing bar uniformly distributed the light into 64 fiber optic cables which are connected one to each wedge . . Inside each wedge assembly, the light was further divided by a secondary rectangular mixing bar into 20 fiber optic cables, each of which connects to a lead glass block. Each counter saw between 1 and 2 GeV energy equivalent of light. Pulse-to-pulse variation of the light output as measured by the counters was 12-14%.

There were several considerations in the design of the gain monitoring system, foremost being the need to assure long-term stability of the light intensity delivered to each counter. A known characteristic of flashlamps is that they lose intensity with time due to erosion of the cathode. To minimize the effects of the flashlamp aging, which diminishes light output over time, a long-life ($> 10^6$ flashes) flashlamp

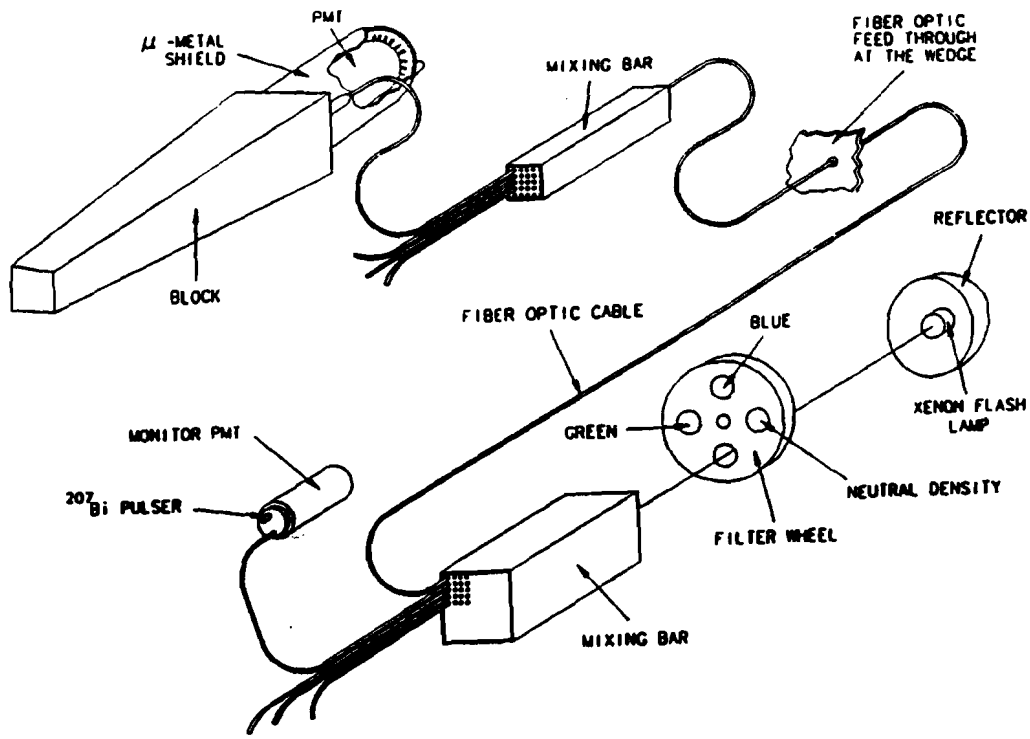

Figure 3.9: Diagram of the gain monitoring system.

was chosen. The long-life flashlamp has another beneficial property. In order to control erosion of the cathode, the breakdown of the Xenon is carefully controlled within the flashlamp bulb. This careful control leads not only to long-life bulbs but also to bulbs that produce small pulse-to-pulse variations in light output.

The selection of the particular fiber optic cable to transmit the light from the source to the 1280 CCAL modules was driven by two concerns. The first concern was the long-term durability of the fibers in a radiation field. The fiber optic cables used were composed of a high purity polymethyl methacrylate core with a transparent fluorine polymer cladding. Using a ^{137}Cs γ source, the fiber optic cables were found to be unaffected by radiation doses up to 1500 *rads*. The other concern in the choice of fibers was whether it was able to transmit enough light near 400 *nm*, over the required cable run, to be useful. As it turned out, the combination of a bright light source, efficient optics and the reasonable attenuation length (350 db/Km at 400 nm) of the fibers combined to provide more than sufficient light to each module. Figure 3.10 shows the flashlamp spectrum after folding in the effects of propagation to the PMT and the PMT quantum efficiency. One can see (from figure 3.10) that the Xenon flashlamp with the plastic fiber distribution system provided a spectrum that is very similar to the Čerenkov spectrum from an electromagnetic shower in the glass. In addition to being radiation hard and transparent, these fibers also had a number of other nice properties that simplified the overall design of the gain monitoring system. The optical properties of the fibers were virtually unaffected by temperature changes, bending, stress, tension, or chemical contamination. Further,

the polymer based fibers (as compared to the only other alternative fiber which is composed of fused silica) were very easy to work with, to handle, and to terminate.

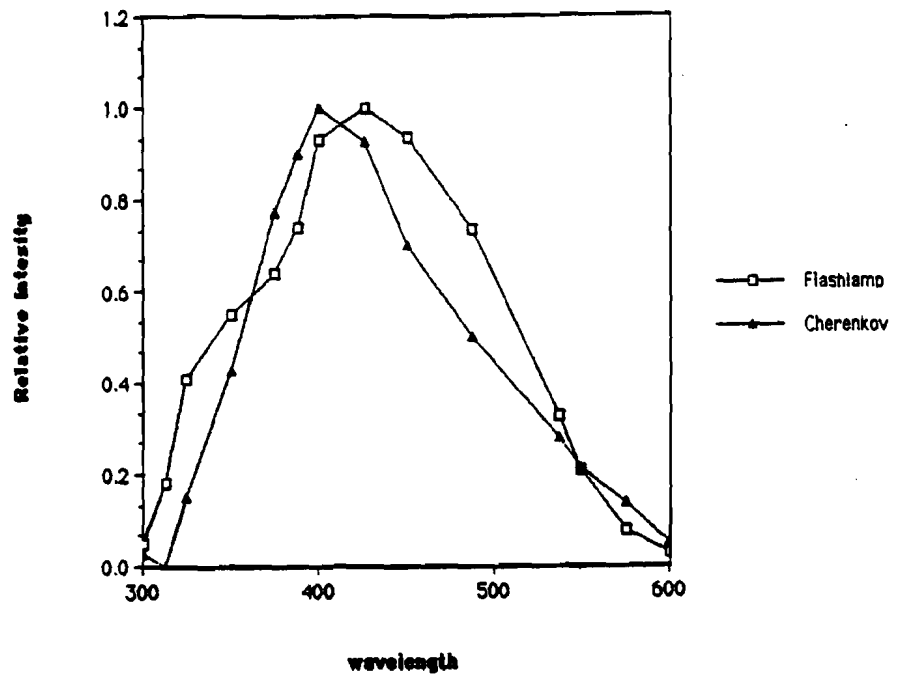

Figure 3.10: This figure shows the flashlamp spectrum as observed by a PMT in the CCAL compared to the Čerenkov spectrum from an electromagnetic shower after the quantum efficiency has been taken into account.

In order to track the pulse-to-pulse intensity changes of the flashlamp, the system incorporates three Hamamatsu R3036 photomultipliers acting as intensity monitors. To monitor long-term drifts, each monitor PMT is equipped with a ^{207}Bi/plastic scintillator light pulser to serve as an absolute gain reference. Figure 3.11 shows a typical spectrum from a ^{207}Bi pulser while figure 3.12 shows a flashlamp pulse height spectrum for one of the monitor tubes.

The gain constants worked remarkably well although they were not perfect. Figure 3.13 shows how the gain constants could correct for the drifting calibration. The

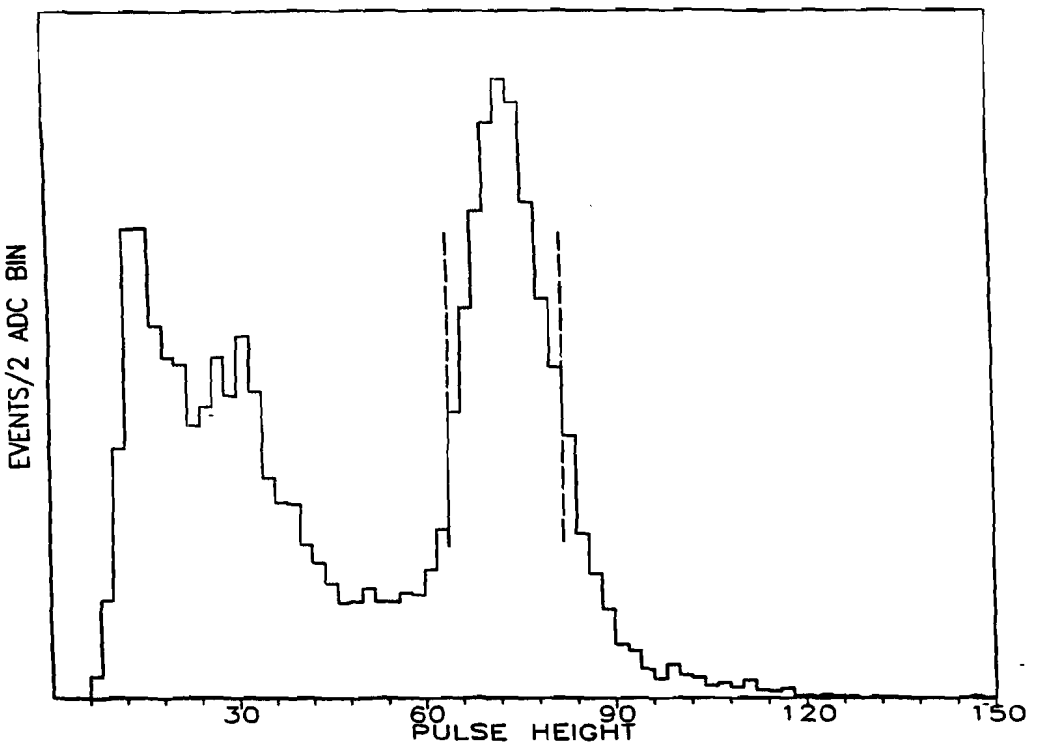

Figure 3.11: ^{207}Bi pulser spectrum as seen by one of the monitor tubes.

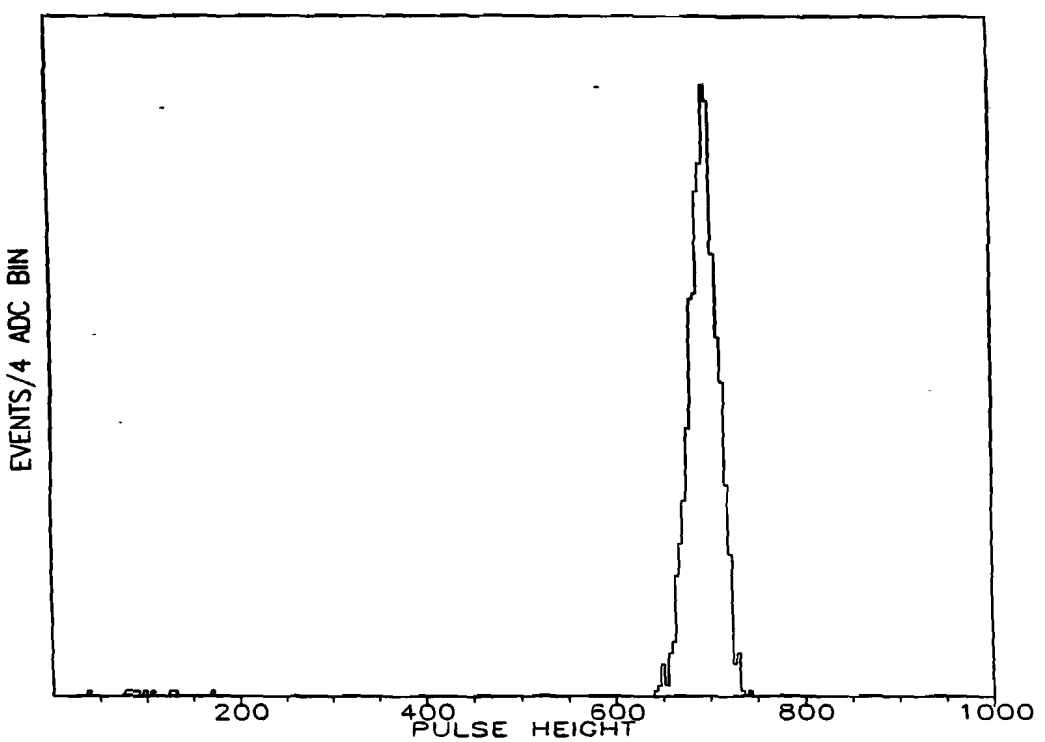

Figure 3.12: Flashlamp pulse height spectrum as seen by one of the monitor tubes.

first plot (in figure 3.13) shows the invariant mass distribution for the J/ψ events that were used to find the original calibration constants. The next plot shows a sample of J/ψ events collected about 1 month later. It is clear that the gains of the PMTs had drifted and caused the observed losses of resolution. By applying corrections derived from the flashlamp data to the calibration constants, the most of the lost resolution could be recovered (see the last plot in figure 3.13).

In addition to tracking the gains, the flashlamp system was very helpful during both the installation and operation of the CCAL. While installing the CCAL the flashlamp was used to check the cabling of individual CCAL channels as well as to provide a signal to conduct rough timing studies. Since the flashlamp ran at 1/6 Hz during the data taking, one had 10 opportunities per minute to check the status of the CCAL. The online flashlamp checks were able to catch almost instantly any problems with the high voltage supply, the ADCs, or the cabling. These online checks helped a great deal in maintaining the high quality of the data collected.

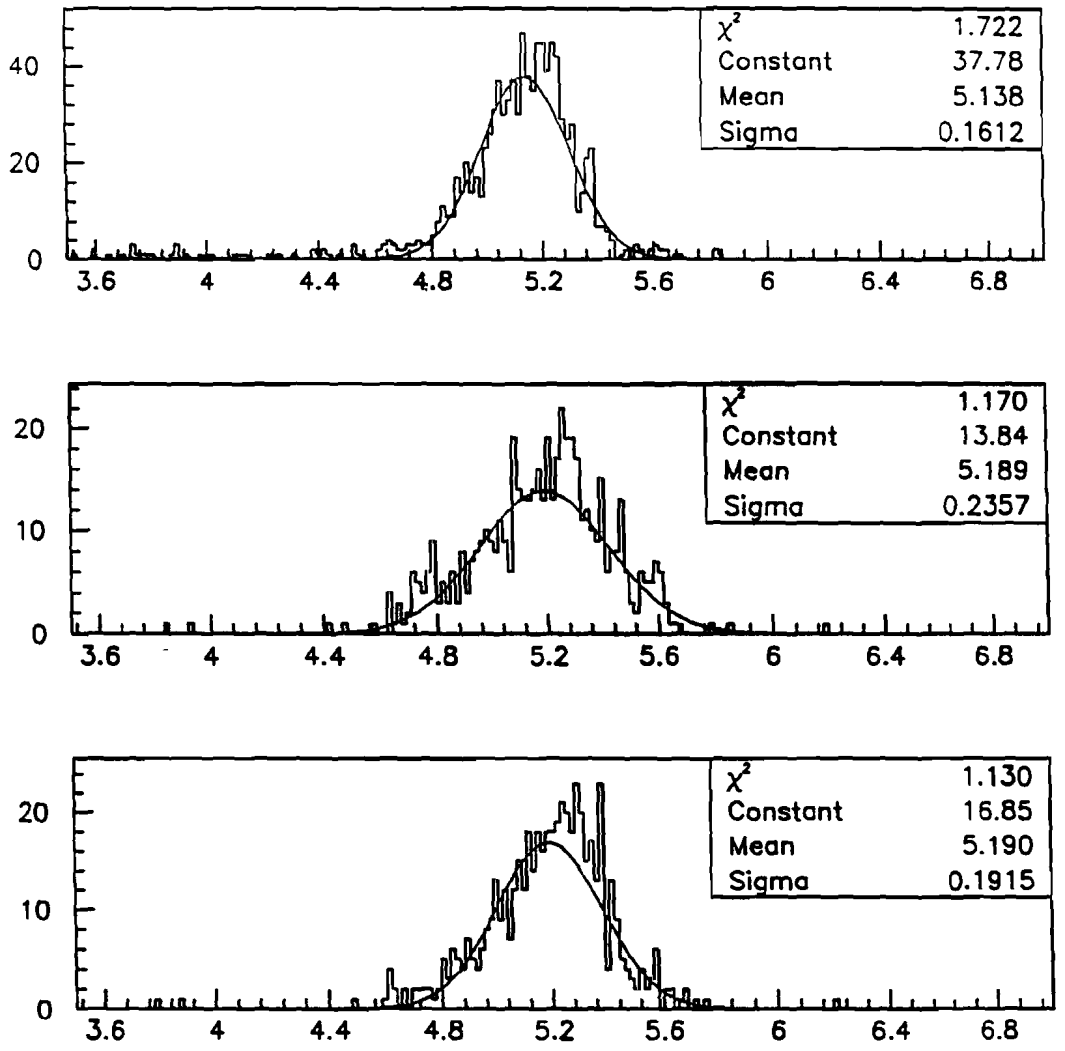

Figure 3.13: Comparison of the calibration with and without the gain monitor. The first plot shows the sample of reconstructed J/ψs from which the initial calibration constants were derived. The second plot shows a sample of reconstructed (using the original calibration constants) J/ψ events collected about a month after the first sample. The third plot is the second J/ψ sample but using the flashlamp gain constants to update the original calibration.

3.5 Clusterization and Resolution

The pointing geometry of the CCAL aids a great deal in the design of a clustering algorithm. The primary purpose of the CCAL clustering algorithm is to determine with reasonable accuracy the energy and position of hits in the CCAL. Since electromagnetic showers in the CCAL extend over many blocks and are symmetrical in shape, it is possible to use a weighted average of the energy deposits around the location of a hit to find the hit position to an accuracy of better than a single block.

The clustering algorithm begins by searching on a 3×3 block grid for all the locally maximal energy deposits. In order for a local energy deposit to become a cluster, the central block must have at least 25 MeV of energy deposited while the surrounding 8 blocks must have at least 25 MeV more among them. This defines the minimum cluster energy of 50 MeV. While the threshold of 50 MeV is appropriate to the analysis presented in this dissertation, the CCAL is capable of thresholds as low as 25 MeV when necessary to suppress the backgrounds, from asymmetrically decaying $\pi^0 s$, to the 2γ final states [40].

Once a cluster center has been identified, the clusterizing algorithm uses the energy weighted sum to determine the approximate entry position of the showering particle on the center block's face. At this point it is convenient to switch to "block units" where the origin is the center of the central block in the 3×3 block cluster. The $\hat{x}$ is taken in the $\hat{\theta_{lab}}$ direction while $\hat{y}$ is along $\hat{\phi_{lab}}$. The energy weighted

position can then be written as:

$$x = \frac{\sum_{i=1}^{9} E_i x_i}{\sum_{i=1}^{9} E_i} \tag{3.5}$$

$$y = \frac{\sum_{i=1}^{9} E_i y_i}{\sum_{i=1}^{9} E_i} \tag{3.6}$$

where E_i is the energy deposited in the ith block, $x_i = -1, 0, 1$ is the block row number for the ith block and $y_i = -1, 0, 1$ is the block column number for the ith block. While the hit position estimate from the weighted average is fairly good, it completely ignores the fact that the CCAL blocks are not square and that the losses in the inactive material between the blocks are different in the $\hat{x}$ direction from that in the $\hat{y}$ direction. To account for this, a parameterization of the transverse shower profile is used. The transverse shower profile can be described by two exponential functions [41], one function describing the shower core and the other describing the tails of the shower.Final hit positions are then extracted by using energy weighted positions and the following functions:

$$|X| = A_x(1 - e^{-\frac{|x|}{x_A}}) + B_x(1 - e^{-\frac{|x|}{x_B}}) \tag{3.7}$$

$$|Y| = A_y(1 - e^{-\frac{|y|}{y_A}}) + B_y(1 - e^{-\frac{|y|}{y_B}}) \tag{3.8}$$

where the constants have been empirically determined from test beam data taken at BNL and are tabulated in table 3.5. The relative sign of the final positions X and Y are the same as those of the energy weighted positions x and y.

Corrections for energy lost in the inactive material between the blocks have been parameterized using a similar functional form

$$E_{corrected} = \frac{E_{measured}}{(1 - C_x e^{-|X'|/x_C})(1 - C_y e^{-|Y'|/y_C} - D_y e^{-|Y'|/y_D})} \tag{3.9}$$

where (X', Y') is the position of the incident hit as measured from the edge of the block rather than the center. Due to the staggering of the blocks in the $\hat{\theta}$ (see figure 3.5) the ring corrections are different depending on which half of the block the incident particle hit, $C_x = C_{low}$ for the "lower" half of the block (larger θ) and $C_x = C_{high}$ for the "higher" half of the block (smaller θ). The values of the energy correction constants have also been empirically determined from test beam data taken at BNL and are tabulated in table 3.5. The slightly different parameterizations for X' and Y' are due to the differing amounts of inactive material in the $\hat{\theta}_{lab}$ and $\hat{\phi}_{lab}$ directions respectively.

Parameter	Value
A_x (ring)	0.2601
x_A (ring)	0.0321
B_x (ring)	0.2574
x_B (ring)	0.1860
A_y (wedge)	0.3138
y_A (wedge)	0.0397
B_y (wedge)	0.1969
y_B (wedge)	0.1715
C_{low} (ring)	0.0614
$x_{C_{low}}$ (ring)	0.1357
C_{high} (ring)	0.0857
$x_{C_{high}}$ (ring)	0.0508
C_y (wedge)	0.1474
y_C (wedge)	0.0204
D_y (wedge)	0.1594
y_D (wedge)	0.0784

Table 3.5: Values of clustering algorithms empirically determined constants.

The overall performance of the CCAL and its clustering algorithm can be determined by comparing particle positions as measured by the CCAL to those measured

by the charged tracking detectors. Using a sample of electrons from the reaction $\bar{p}p \rightarrow J/\psi \rightarrow e^+e^-$ one can plot the difference between θ_{lab} and ϕ_{lab} as measured by the charged tracking and as measured by the CCAL (see figures 3.14 and 3.15). After deconvolving the average charged track resolution (2.5 $mrad$ rms in θ_{lab} and ϕ_{lab}) the average angular position resolutions for the CCAL are found to be $\sigma_{\theta_{lab}} = 6.2\ mrad$ and $\sigma_{\phi_{lab}} = 12.5\ mrad$. Note that $\sigma_{\theta_{lab}}$ and $\sigma_{\phi_{lab}}$ give similar position resolutions when expressed in block units $\sigma_{x_{lab}}$ and $\sigma_{y_{lab}}$ at the surface of the block. By using the measured angles and two body kinematics, the energy of each electron from the reaction $\bar{p}p \rightarrow J/\psi \rightarrow e^+e^-$ can be predicted accurately. Figure 3.16 shows the difference between the predicted energy and the measured energy, divided by the predicted energy for a sample of J/ψ events. One can then see that the energy resolution is about $\sigma(\delta E/E) = 4.3\%$ for electrons with an average energy of about 2.5 GeV.

3.6 CCAL Logic and Timing Information

The goal of the CCAL logic [42] was to provide input to the hardware trigger. In order to do this in a reasonable way, the 1280 channels from the CCAL had to be reduced to a more manageable number. As is discussed in the next chapter, the basic trigger requires two particle final states consistent with the decay of a charmonium resonance.

In order to isolate large energy deposits in the CCAL and keep the number of logic channels reasonable, the 1280 CCAL channels were summed by two levels of

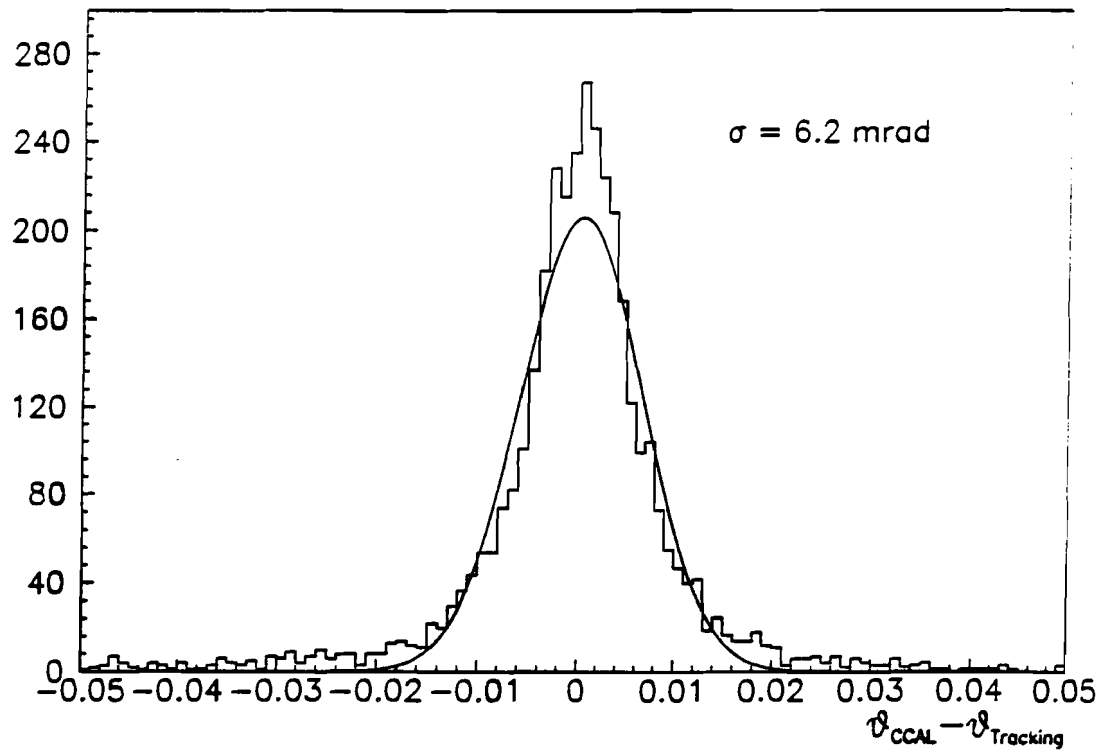

Figure 3.14: Difference between θ_{lab} as determined by the CCAL and that determined by the charged tracking for a sample of J/ψ events.

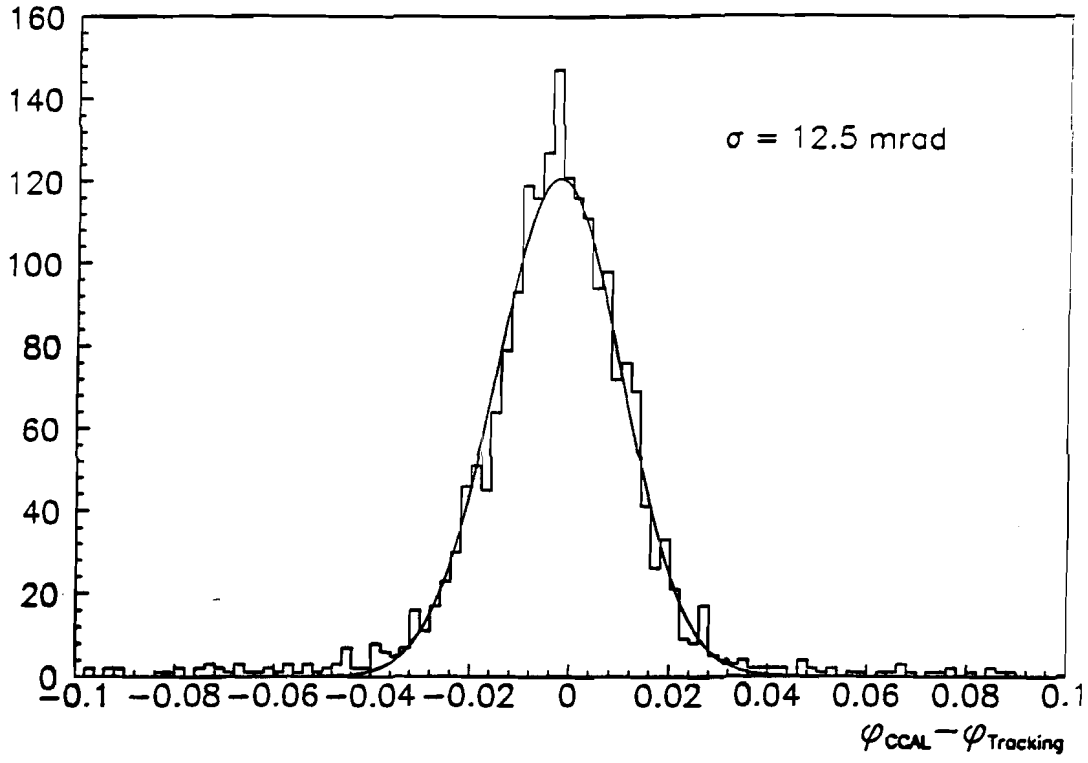

Figure 3.15: Difference between ϕ_{lab} as determined by the CCAL and that determined by the charged tracking for a sample of J/ψ events.

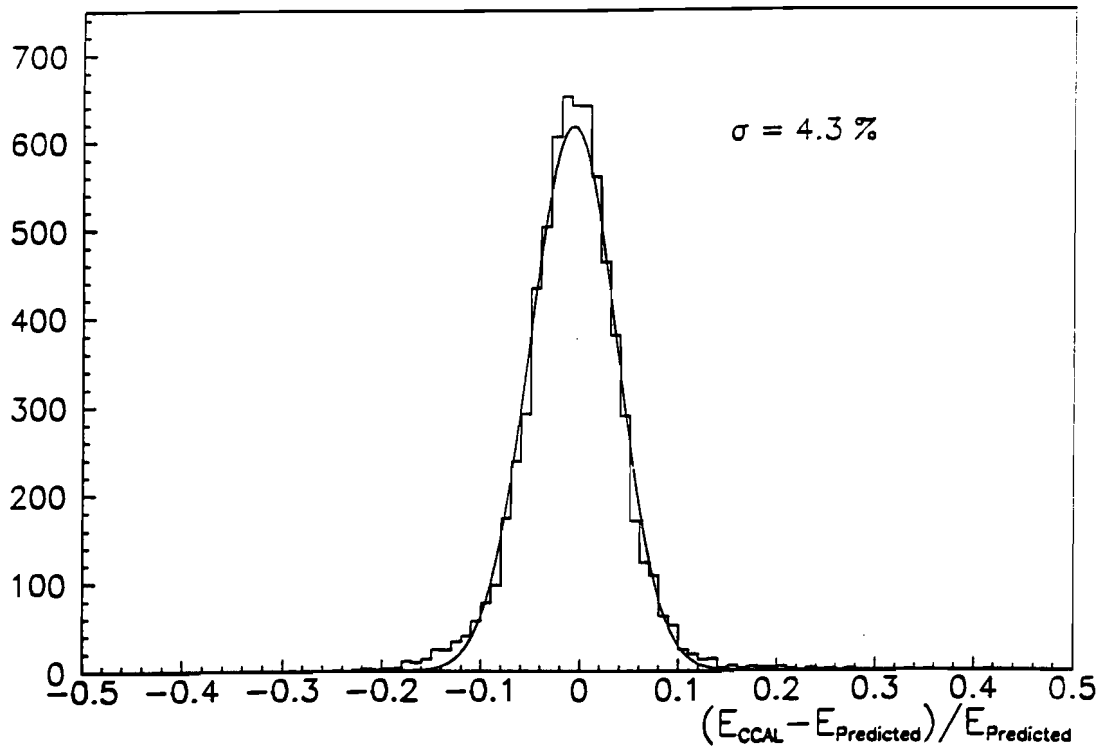

Figure 3.16: Average calorimeter energy resolution.

analog summers. The first level summer summed in the $\hat{\phi}_{lab}$ direction. The sums were constructed by taking 5% of the charge from the CCAL signals and constructing analog sums by taking groups of eight wedges with one wedge overlap to form "super wedges". This level 1 sum reduced the number of CCAL signals to 160 (8 divisions in ϕ_{lab} and 20 divisions in θ_{lab}). These 160 level 1 sums were the input to the level 2 summer which summed in the $\hat{\theta_{lab}}$ direction. The level 2 summer grouped together groups of four rings plus one ring of overlap to form the final 40 logic signals (8 divisions in ϕ_{lab} and 5 divisions in θ_{lab}). Unlike the the level 1 sums which are linear, the level 2 sums are weighted to compensate for the differing amount of energy expected from the kinematics of the process $\bar{p}p \rightarrow J/\psi \rightarrow e^+e^-$. The weights have been added to allow the setting of sharper discriminator thresholds.

Figure 3.17 shows the expected energy deposited in the CCAL as a function of ring number before and after weighting for $\bar{p}p \rightarrow J/\psi \rightarrow e^+e^-$.

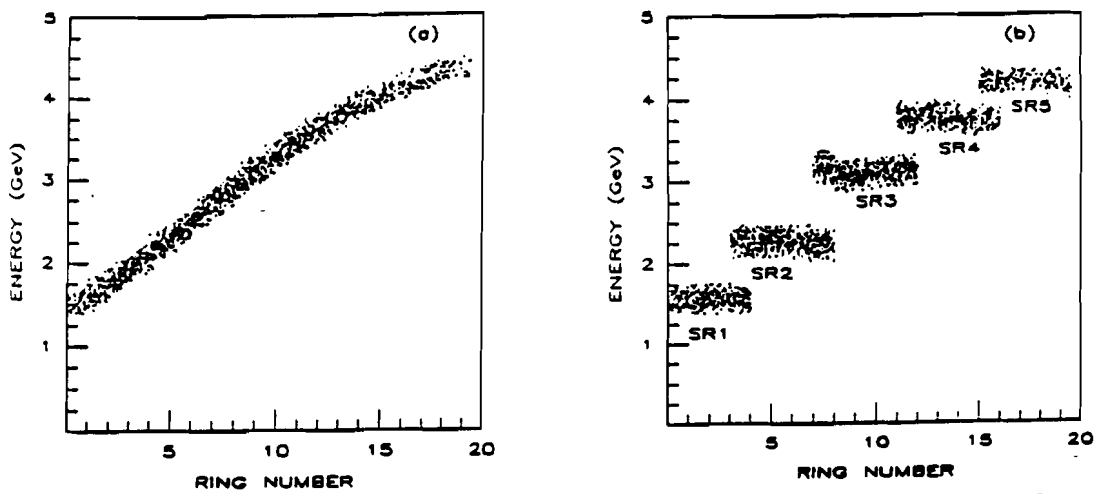

Figure 3.17: Monte Carlo simulation for the reaction $\bar{p}p \rightarrow J/\psi \rightarrow e^+e^-$. The ring number hit by the electron or positron is plotted vs the energy deposited: (a) shows the observed energy when no weights are used and (b) shows the observed energies when the level 2 summing weights are used.

The 40 final CCAL summed signals can really be thought of as "super blocks" since each one roughly corresponds to the sum of 32 neighboring blocks. The trigger accepts two logic inputs that are formed from the CCAL sums. The most important trigger input from the CCAL is the "PBG1" logic. PBG1 is constructed from the 40 super blocks and requires that there be two large energy deposits in the CCAL consistent with the decay of the J/ψ to e^+e^-. The PBG1 requirement is equivalent to requiring that the two large clusters be roughly coplanar. For data taken at the J/ψ, the actual requirement was that the two largest super blocks be exactly 4 super wedges apart. At all other resonances, the PBG1 requirement was loosened

to account for the momentum of the recoiling photon in the various transitions to the J/ψ such as $\chi_{1,2} \rightarrow J/\psi + \gamma \rightarrow e^+e^- + \gamma$, and only required that the two largest super blocks be separated by at least 3 but no more than 5 super wedges. The other logic input that is used in the hardware trigger is the total energy (ETOT) which a linear sum of the 160 level 1 summer outputs. The ETOT is only an approximate total energy since it does include the overlapping wedges from the level 1 summing process.

The CCAL summer outputs were not only useful in the trigger but were also invaluable in rejecting "pile-up" clusters in the CCAL. Pile-up clusters are clusters that are out of time with respect to the event that caused the trigger. In the 1990 data set pile-up was not much of a problem since the luminosities were relatively low. In 1991 however, the pile-up issue was more significant and typically contaminated $\sim$ 10% of the events. Since it was not practical to instrument all 1280 channels of the CCAL with TDCs, it was decided that some useful timing information could be extracted by using the 160 level 1 summer outputs. The super block analog signals were discriminated at about a 40 MeV level and sent to pattern units that were latched in by the trigger for 30 ns. If a hit occurred within one of the regions defined by the 160 level 1 sum signals but did not trigger the corresponding pattern unit, then the hit was considered out of time. A secondary determination of the cluster times could be gotten by using information from the 40 super blocks. Signals from the 40 super blocks were instrumented with two ADCs each. The first ADC integrates charge starting 100 ns before the trigger for 150 ns, while the second

ADC integrates from the beginning of the trigger for 150 ns. By looking at the ratio between the charge observed before a trigger and that coincident with a trigger, cluster timing could be determined. If there were ambiguities such as those caused by more than one hit in a super block, then timing could not be determined accurately. In the case of ambiguities or if the cluster had less than 100 MeV, the cluster time was designated as "undetermined". The effect of these undetermined clusters on the analysis efficiency is discussed later.

Chapter 4

The Trigger and Data Aquisition

The E760 data aquisition system was designed to handle the enormous rate from the nonresonant $\bar{p}p$ interactions. For example at the χ_2, the total $\bar{p}p$ cross section is $\approx 70mb$; this leads to an interaction rate of $\approx 700KHz$ at a luminosity of $10^{31} cm^{-2} s^{-1}$.

4.1 The Hardware Triggers

The basic trigger scheme involved two levels of hardware logic and a third level based on software reconstruction of events. The level 1 trigger was formed from low level logic elements that were based on simple topological inputs from the Čerenkov, the scintillator hodoscopes (H1,H2 and FCH), and the calorimeters (FCAL and CCAL). The level 1 triggers were defined as follows:

- *Hadron Tag (h)* - A hadron was defined to be the coincidence of an H1 with an appropriate H2 such that a line could be drawn from the vertex through both counters [1] (see figure 4.1).

[1] *The tag h for the data taken in 1990 was as shown in figure 4.1. In 1991 this was loosened to account for the finite size of the target by allowing a coincidence between an H1 and any one of six H2 counters (one extra on each side of the original four).*

- *Electron Tag (e)* - When a hadron could be combined with a Čerenkov cell in the same octant, an electron tag was also produced (see figure 4.1).

- *Coplanarity (COPL)* - The coplanarity flag required that two tagged hadrons or electrons be separated in ϕ_{lab} by at least 15 but no more than 17 H2 elements.

- *H1 OR (H1OR)* - This flag was set whenever there was a hit in any of the eight H1 hodoscope modules.

- *Hodoscope Multiplicity (#H1, #H2)* - These two variables would specify the number of hits in each of the hodoscopes H1 and H2.

- *Forward Charged OR (FCHOR)* - This flag was set if there was a hit in any of the eight FCH hodoscope modules.

- *FCAL OR (FCALOR)* - This flag was set whenever there was a hit in the Forward Calorimeter that exceeded an energy of $\approx$100MeV.

- *Total CCAL Energy (ETOT)* - The total energy flag was set when the analog sum from the Central Calorimeter exceeded $\approx$90% of the total available energy.

- *CCAL Two Body Tag (PBG1)* - The 1280 Central Calorimeter signals were summed into 40 "super-modules" with a segmentation of 5 "super-rings" in θ_{lab} and 8 "super-wedges" ϕ_{lab}. When two of these super-modules were loosely consistent with a two-body decay from a $\bar{p}p \rightarrow J/\psi \rightarrow e^+e^-$, this flag was set (see discussion 3.6).

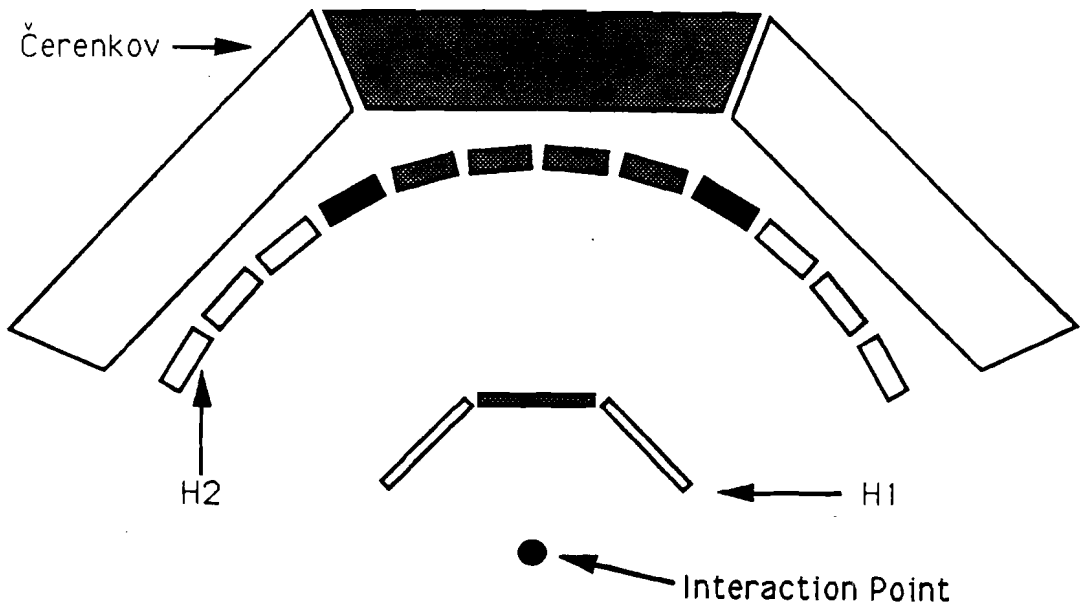

Figure 4.1: Coincidence between H1, H2, and the Čerenkov required to form the charged track tags *h* and *e*. *For 1990 the hashed H1 was required in coincidence with the hashed Čerenkov and with any one of the four hashed H2 modules. In 1991 the coincidence was expanded to include the two black shaded H2 modules as well.*

4.1.1 The Level 2 Triggers

The level 1 triggers were used to construct all the various level 2 triggers. The level 2 triggers were themselves combined into one of four readout groups, designated below:

- *MLU1* - The charged trigger.
- *MLU2* - Two body trigger.
- *MLU3* - Test or development trigger.
- *MLU4* - The neutral trigger.

These differed in terms of the detector subsystems which were readout. The distinction between the various read out types was done in order to reduce dead time in the data aquisition system. The charged trigger readout took about $1ms$ as compared to the neutral trigger which could be read out in $0.1ms$. The *MLU2* trigger was used during the run to collect events of the type $\bar{p}p \rightarrow 2(\textit{charged hadrons})$. This trigger was prescaled typically by a factor of ~ 200. A given event could simultaneously satisfy both the $MLU1$ and $MLU2$ triggers in which case the event would be treated as an $MLU1$ trigger. As its name implies the $MLU3$ trigger was used only for testing and development purposes.

4.1.2 MLU1 - The Charged Trigger

The E760 charged trigger was designed to select high mass objects that decay to e^+e^-. The four level 2 triggers that were OR'ed together to form the MLU1 readout

group were defined as follows:

- 2 Čerenkov $(2\check{C})$: $(PBG1) \otimes (\#H2 \leq 4) \otimes (\#H1 \leq 4) \otimes (2h) \otimes (2e)$
- *1* Čerenkov *$(1\check{C})$* : $(PBG1) \otimes (\#H2 = 2) \otimes (\#H1 = 2) \otimes (2h) \otimes (1e) \otimes (COPL)$
- *0* Čerenkov *$(0\check{C})$* : $(PBG1) \otimes (\#H2 = 2) \otimes (\#H1 = 2) \otimes (\overline{FCHOR}) \otimes (2h) \otimes (COPL)$
- *2* Čerenkov/*No CCAL* : $(\#H2 = 2) \otimes (\#H1 \leq 2) \otimes (2h) \otimes (2e) \otimes (COPL)$

The first three triggers allowed us to understand the inefficiencies introduced by the Čerenkov septum. The $0\check{C}$ trigger was used during all J/ψ running and at the 1991 χ_2. The last trigger was used only at the J/ψ and allowed us to study the effect of the CCAL in the trigger.

4.1.3 MLU4 - The Neutral Trigger

The neutral trigger was designed to select two classes of all neutral events, those with a high invariant mass and those where most of the available energy was deposited in the Central Calorimeter. The two level 2 triggers that were OR'ed together to form the MLU4 readout group were defined as follows:

- *Neutral 2 Body* : $(PBG1) \otimes (\overline{H1OR}) \otimes (\overline{FCHOR})$
- *Total Energy* : $(ETOT) \otimes (\overline{H1OR}) \otimes (\overline{FCHOR}) \otimes (\overline{FCALOR})$

4.2 The Overall Charged Trigger Efficiency

The charged trigger efficiency enters into the analysis of the reaction $\chi_{1,2} \rightarrow J/\psi + \gamma \rightarrow e^+e^- + \gamma$ in two ways:

- The trigger efficiency ($\epsilon_{trigger}$) is required in order to determine the cross section since the overall efficiency (ϵ) is the product of $\epsilon_{trigger}$, the geometrical acceptance ($\epsilon_{geometric}$), and the analysis efficiency ($\epsilon_{analysis}$).

- The various subtriggers have the potential to introduce angular biases into the data since they select different classes of events. It will be shown later that a knowledge of the relative efficiencies of the $0\check{C}$, $1\check{C}$, and $2\check{C}$ triggers is essential in order to fit the angular distributions.

Unless otherwise noted all the efficiencies discussed below were for the reaction $\chi_{1,2} \rightarrow J/\psi + \gamma \rightarrow e^+e^- + \gamma$. The fiducial region over which electrons were accepted was restricted to $15° < \theta_{lab} < 65°$ as determined by the CCAL. This is the same fiducial volume that will be used in the later analysis. The term "clean" below refers to a sample of events that were selected using an exclusive kinematical fit and a nominal cut on the invariant mass of the e^+e^- pair. The background contamination in the clean samples was less than 1%.

4.2.1 Cracks in H1 and H2

By far the largest source of inefficiency in the charged trigger came from the hadron tag which required a coincidence between appropriate H1 and H2 counters.

Since the hodoscope modules did not overlap each other, there were cracks where particles could escape detection. This problem has been examined in two ways.

The first method used to check the effects of the H1 and H2 cracks on the trigger was to select a sample of events that had more than two good charged tracks. One could then look at the extra tracks (i.e. the tracks that did not cause the trigger) and simply count the fraction of time that an H1 or an H2 did not provide a signal. This study showed that the cracks do indeed cause substantial losses.

The second method exploited the fact that the cracks in H1 coincide with those of H2 (see figure 4.1). By using a clean sample of reconstructed (selected and reconstructed using the central calorimeter) $J/\psi \rightarrow e^+e^-$ events, it was possible to map out the efficiency across an H1 or H2 module. Figure 4.2 shows such a map where all 32 H2 modules have been overlaid onto a single module to improve the statistics. Figure 4.2 clearly shows the depletion caused by the cracks in both H1 and H2. The efficiency can then be found by comparing the number of events expected to the number of events observed.

Although the results for the two methods are compatible, only the results of the first method are given below because their statistical error is somewhat smaller [25]:

- *For 1990* $\chi_{1,2}$: $\epsilon_{2h} = 0.87 \pm 0.02$
- *For 1991* $\chi_{1,2}$: $\epsilon_{2h} = 0.94 \pm 0.02$

The differences in ϵ_{2h} between the 1990 and 1991 data set came from a change in the number of H2 modules that were associated with a given H1. As noted earlier, the finite size of the target meant that we would not always have perfect alignment

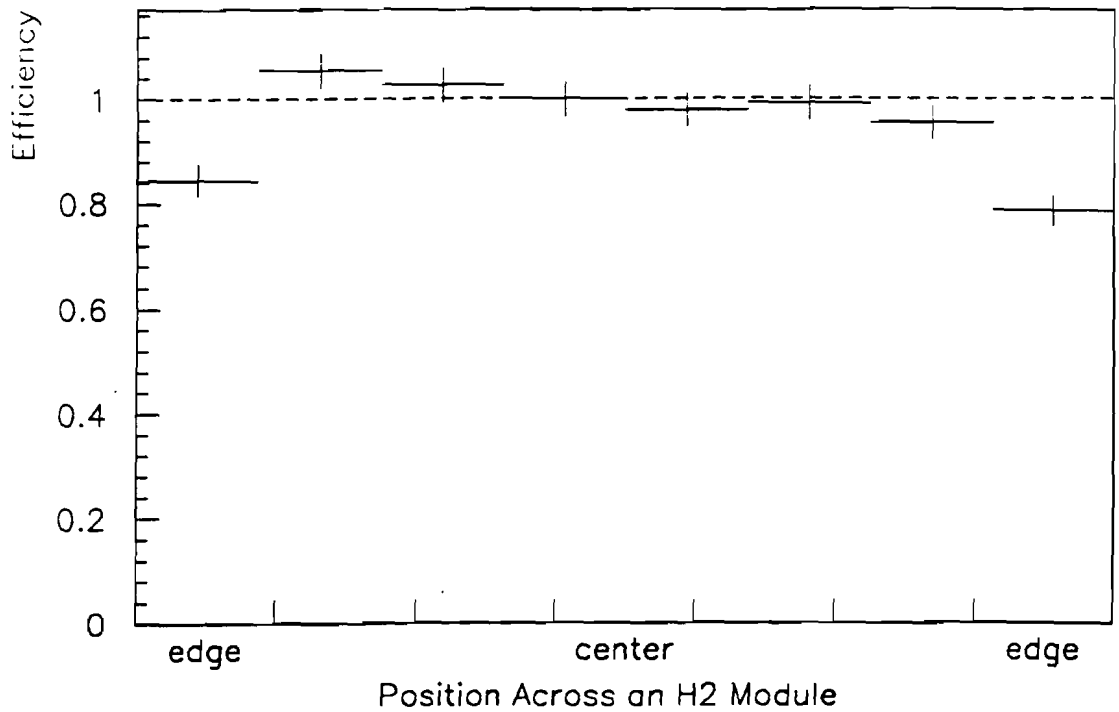

Figure 4.2: The efficiency of hadron tag for 1991 data set.

between the vertex, H1 and H2. The 1991 hadron tag allowed six H2 counters (instead of four) to be associated with each H1 and thus reduced the losses.

4.2.2 Hodoscope Multiplicity

A relatively large source of inefficiency, especially in the $0\check{C}$ and $1\check{C}$ triggers, was caused by extra hits in the hodoscopes. These extra hits had a number of sources, some of which were correlated with the event and some which were purely random including:

- δ rays in H1 due to interaction of the beam halo with the beam pipe;
- δ rays in H2 due to the passage of the electrons through the tracking detectors;

- conversion of the decay photon ($\chi_{1,2} \rightarrow J/\psi + \gamma$) in the beam pipe or in the inner tracking detectors causing hits in H1 or/and H2.

In order to study the effect of extra hodoscope hits on the $0\check{C}$ and $1\check{C}$ triggers, a clean sample of reconstructed $\chi_{1,2}$ events was selected using the $2\check{C}$ trigger. By imposing the hodoscope multiplicity requirements on this sample, it was possible to determine the efficiency (see tables 4.1 and 4.2). This method allowed the determination of these efficiencies without explicit knowledge of the source of extra hits.

	Events ($2\check{C}$ trigger)	Events ($2\check{C}$ trigger)$\otimes$ $(\#H2 = 2) \otimes (\#H1 = 2)$	Efficiency $(\#H2 = 2) \otimes (\#H1 = 2)$
1990 χ_1	284	210	0.74 ± 0.07
1990 χ_2	343	265	0.77 ± 0.06
1991 χ_2	1621	1117	0.69 ± 0.03

Table 4.1: Efficiencies for $(\#H2 = 2) \otimes (\#H1 = 2)$ requirements for the $1\check{C}$ trigger.

	Events ($2\check{C}$ trigger)	Events ($2\check{C}$ trigger) $\otimes(\overline{FCHOR})\otimes$ $(\#H2 = 2) \otimes (\#H1 = 2)$	Efficiency $(\overline{FCHOR})\otimes$ $(\#H2 = 2) \otimes (\#H1 = 2)$
1990 χ_1	284	209	0.74 ± 0.07
1990 χ_2	343	251	0.73 ± 0.06
1991 χ_2	1621	1069	0.66 ± 0.03

Table 4.2: Efficiencies for $(\#H2 = 2) \otimes (\#H1 = 2) \otimes (\overline{FCHOR})$ requirements for the $0\check{C}$ trigger.

In order to study the effect of the $\#H2 \leq 4 \otimes \#H1 \leq 4$ on the $2\check{C}$ trigger, it was necessary to determine the occupancy rate of the #H2 and #H1 counters. Using

the same $\chi_{1,2}$ sample as above, one could determine the rate of extra (in addition to those from e^+e^-) hodoscope hits (see table 4.3).

	Events (2Č trigger)	Events (2Č trigger)⊗ Extra $\#H1 \geq 1$	Events (2Č trigger)⊗ Extra $\#H2 \geq 1$
1990 χ_1	284	21	53
1990 χ_2	343	28	62
1991 χ_2	1621	272	328

Table 4.3: Occupancy of the hodoscope H1 and H2

For the reaction $\chi_{1,2} \rightarrow J/\psi + \gamma$, an event would have been rejected by the $2\check{C}$ trigger if there were three or more extra hodoscope hits. Using the information from table 4.3 one can estimate the probability of losing an event in the $2\check{C}$.

- *For 1990* χ_1 : $\epsilon_{\#H2\leq 4 \otimes \#H1\leq 4} \approx 0.99 \pm 0.01$
- *For 1990* χ_2 : $\epsilon_{\#H2\leq 4 \otimes \#H1\leq 4} \approx 0.99 \pm 0.01$
- *For 1991* χ_2 : $\epsilon_{\#H2\leq 4 \otimes \#H1\leq 4} \approx 0.988 \pm 0.002$

4.2.3 The PBG1 and COPL Requirements

The efficiency of the PBG1 requirement was found by looking at events taken at the J/ψ resonance. From a sample of 3744 J/ψ events that were selected using the Čerenkov instead of the CCAL, none were found to fail the PBG1 requirement. At the $\chi_{1,2}$ the decay photon has the potential to spoil the coplanarity of the two body decay of the ψ in the reaction $\chi_{1,2} \rightarrow J/\psi + \gamma \rightarrow e^+e^- + \gamma$. However, the 40 "super-modules" were sufficiently large that J/ψs from the $\chi_{1,2}$ were indistinguishable from

the true two body events found at the J/ψ resonance. The efficiency of the PBG1 requirement is thus taken to be $\approx 100\%$ at the $\chi_{1,2}$.

The efficiency of COPL requirement was determined by simply applying this requirement to a clean sample of $\chi_{1,2}$ events that was taken with the $2\check{C}$ trigger. Unlike the PBG1, the COPL requirement does cut events where the decay photon carried off a large amount of momentum (see table 4.4).

	Events ($2\check{C}$ trigger)	Events ($2\check{C}$ trigger)$\otimes$ (COPL)	Efficiency (COPL)
χ_1	284	262	0.92 ± 0.08
χ_2	1964	1705	0.87 ± 0.03

Table 4.4: Efficiency of the COPL requirement.

4.2.4 The Čerenkov Septum

As noted earlier the Čerenkov contains a septum at $\theta_{lab} = 38°$. While the septum is only $0.3mm$ thick aluminum foil, it does cause measurable losses due primarily to poor optics in this region. The Čerenkov is the only trigger element whose inefficiency is localized to a specific angular region in θ_{lab}. It is therefore important to understand not only the overall efficiency of the Čerenkov in the trigger, but also its efficiency as a function of θ_{lab} in order to study the $\chi_{1,2}$ angular distributions.

The easiest way to study the Čerenkov efficiency is to use a clean sample of J/ψ events and then look at the $0\check{C}$, $1\check{C}$, and $2\check{C}$ triggers. Figure 4.3 shows the distribution of electrons collected on the various triggers from the decay of the J/ψ.

The inefficiency caused by the septum can clearly be seen at $\cos(\theta_{cm})=0$.

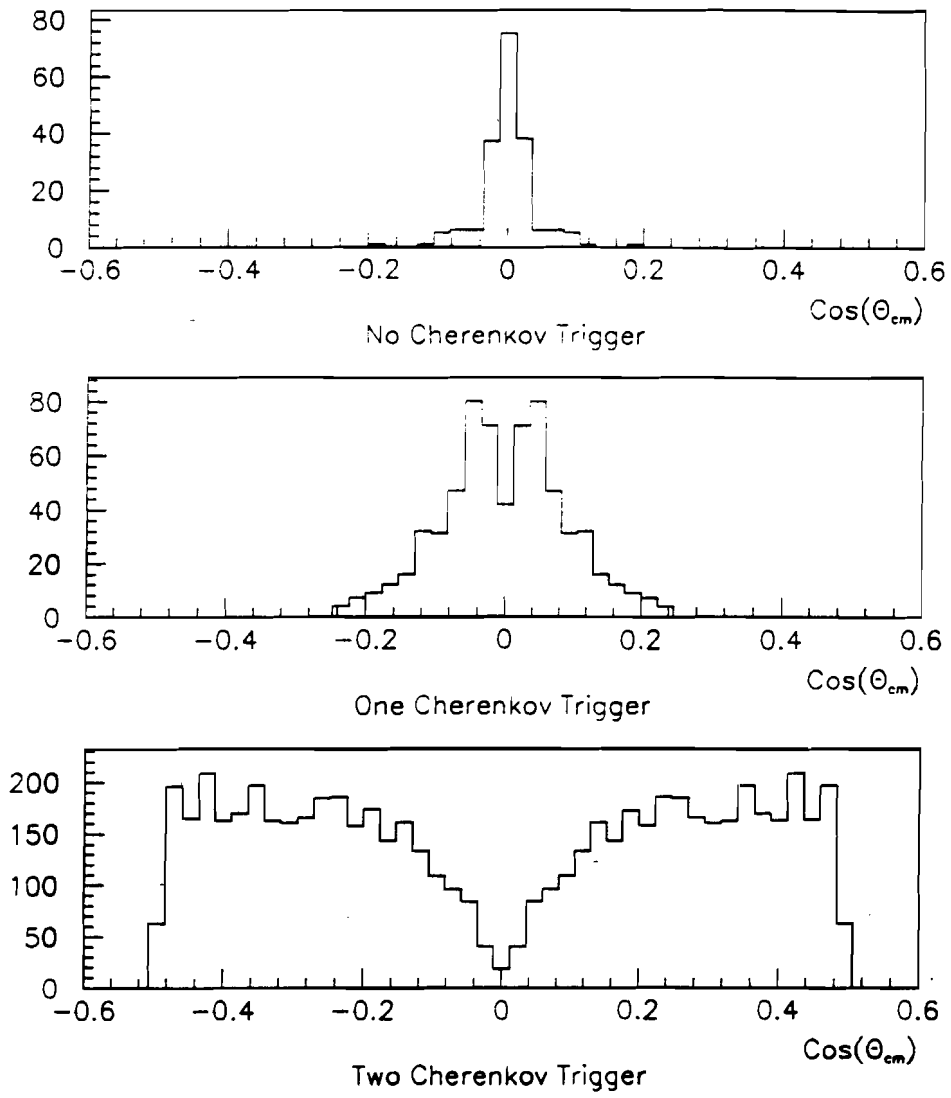

Figure 4.3: Distribution of electrons from J/ψ decays.

Ideally if the $1\check{C}$ and $0\check{C}$ triggers were as efficient away from the septum as the $2\check{C}$ trigger, all the angular bias could be removed by simply adding the three samples together. However, one can use the relative efficiencies of the various triggers to extract the angular dependence of the Čerenkov efficiency. Figure 4.4 shows the ratio of the observed events to the number expected as a function of $\cos(\theta_{cm})$.

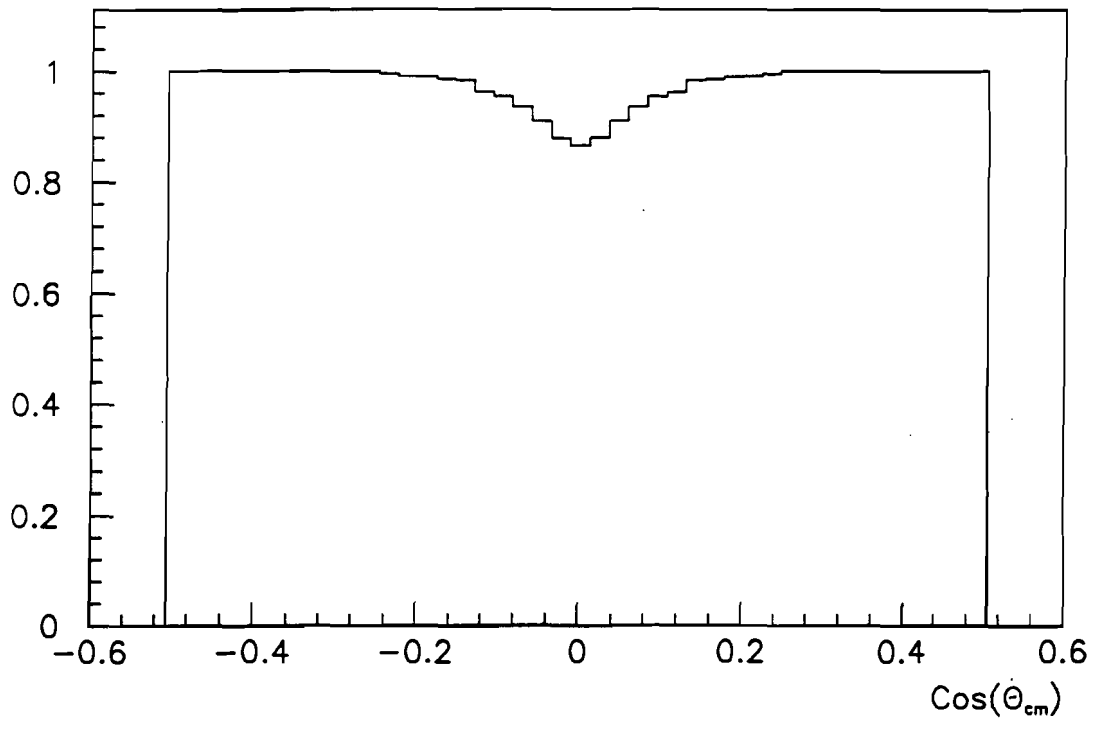

Figure 4.4: Čerenkov efficiency as a function $\cos(\theta_{cm})$ from a 1991 sample of J/ψ events.

The overall number of events lost in the septum depends in general on the kinematics of the event. For example, at the J/ψ, since we have a strictly two body event and the septum is at $\theta_{cm} = 90°$, if one electron enters the septum region, the other will also. At the $\chi_{1,2}$ if one electron enters the septum region the other electron almost never does. For this reason the efficiency for requiring that at least one of the two electrons register a hit in the Čerenkov (ϵ_{1e}) is $\epsilon_{1e} \approx 100\%$ for $\chi_{1,2}$ events. The efficiency for requiring that both electrons register Čerenkov hits (ϵ_{2e}) can be found looking at the ratio of events that are collected on the 2Čerenkov and the 1Čerenkov triggers after all other inefficiencies have been removed. ϵ_{1e} and ϵ_{2e} as defined have no angular dependence within the physical acceptance of the Čerenkov and are tabulated below for both the 1990 and 1991 data sets. Note that the effect of the tight hodoscope multiplicity requirements is especially acute in the 1991 data set since it was collected under high luminosity conditions.

- *For 1990* χ_1 : $\epsilon_{2e} = 0.89 \pm 0.02$
- *For 1990* χ_2 : $\epsilon_{2e} = 0.88 \pm 0.02$
- *For 1991* χ_2 : $\epsilon_{2e} = 0.80 \pm 0.01$

4.2.5 Efficiencies of the Various Subtriggers

By using the results of the previous several sections, the absolute efficiency of the various charged level 2 triggers have been calculated. The results are summarized in table 4.5 where the errors are only statistical.

	$2\check{C}$ Efficiency	$1\check{C}$ Efficiency	$0\check{C}$ Efficiency
1990 χ_1	0.77 ± 0.03	0.59 ± 0.06	—
1990 χ_2	0.76 ± 0.03	0.58 ± 0.05	—
1991 χ_2	0.74 ± 0.02	0.56 ± 0.03	0.54 ± 0.03

Table 4.5: Efficiencies for the various charged level 2 triggers averaged over all angles.

The overall Charged Trigger efficiencies averaged over all angles for $\chi_{1,2}$ were calculated by taking the OR of the appropriate triggers from table 4.5. One must account for the fact that the various level 2 charged triggers are not completely independent and all require that each electron be tagged by both an H1 and an H2 counter (see discussion in section 4.2.1). The overall charged trigger efficiency is calculated from:

$$\epsilon_{trig} = 2\check{C} + 1\check{C}(\epsilon_{2h} - 2\check{C}) \tag{4.1}$$

where $2\check{C}$ and $1\check{C}$ are given in table 4.5 and ϵ_{2h} is given in section 4.2.1. The charged trigger efficiencies are summarized below:

- *For 1990* χ_1 : $\epsilon_{trig} = 0.83 \pm 0.03$
- *For 1990* χ_2 : $\epsilon_{trig} = 0.82 \pm 0.03$
- *For 1991* χ_2 : $\epsilon_{trig} = 0.86 \pm 0.02$

4.3 The Level 3 "ACP" Trigger

The level 3 trigger consisted of a farm of 26 Fermilab ACP processors [43,44]. The APCs were responsible for assembling the data from the various detectors into events and then conducting a preliminary analysis. The ACP analysis was geared towards the neutral final states. The presence of the ACP system allowed for the more traditional hardware triggers to be looser than would have otherwise been required. This resulted in an overall trigger that was less susceptible to biases. In addition to being part of the trigger, the ACPs were an integral part of the overall readout system.

The ACP reconstruction began with the calculation of all the cluster energies and cluster positions within an event. The clusterizing algorithm used was similar to the offline algorithm except that unresolved double hits were not split. The invariant masses of all two-cluster combinations were calculated to make particle identifications on the basis of mass. Beginning with the highest mass objects, clusters were assigned to a particle and then removed from further consideration. Once the clusters were assigned to particles, the event's total energy and various kinematic quantities were calculated. The ACP information was appended to the data stream.

For the MLU1 (charged) events, there was no further processing by the ACP system. The MLU1 events were passed to the front-end VAX and written to tape at a rate of about $20Hz$. The MLU4 (neutral) events, however, were subjected to a software filter in order to reduce the event rate from about $1KHz$ to a more

manageable $200Hz$. Although complex selection criteria could have been used in the ACP filter, a simple selection based on total energy was sufficient.

The ACP information proved to be very useful offline during the data summary tape (DST) production. By selecting events based on the ACP bits, specific classes of events could be sorted for further offline processing. This capability was invaluable to E760 because it allowed a very fast turn-around on the first pass data analysis. It was often the case that the data analysis would lag behind the data collection by only a few hours. The ACP analysis was also invaluable for online monitoring purposes. By using the ACP bits to strip out events from the data stream, the online monitor could catch any detector related problems quickly. Overall the ACP system allowed E760 to accept a higher luminosity than would have been possible otherwise. Not only did E760 take more data as a result of the ACP system, but the data that was collected was of higher quality.

4.3.1 Data Readout Hardware

The data aquisition hardware was based primarily on the Fermilab standard Smart Crate Controller [45] (SCC) readout system. The system used conventional CAMAC modules in standard CAMAC crates. The SCC, which worked in conjunction with an A2 type CAMAC controller, read out modules using the CAMAC backplane. The advantage of the SCC system was that once the data was read out, it could then be sent from the SCC via a front panel bus directly to VME based data buffers (RBUF). After the data for a given event was in the RBUFs, it was

then avaliable to the ACP processors. As described earlier, the ACPs were responsible for gathering together the data for a given event from the 8 RBUFs. Once the event had been "built," it was then processed by the ACPs and passed to the front end VAX. The VAX was then responsible for writing the events to $8mm$ tapes and distributing specific event types to other computers for monitoring purposes. A schematic of the data aquisition readout system is shown in figure 4.5.

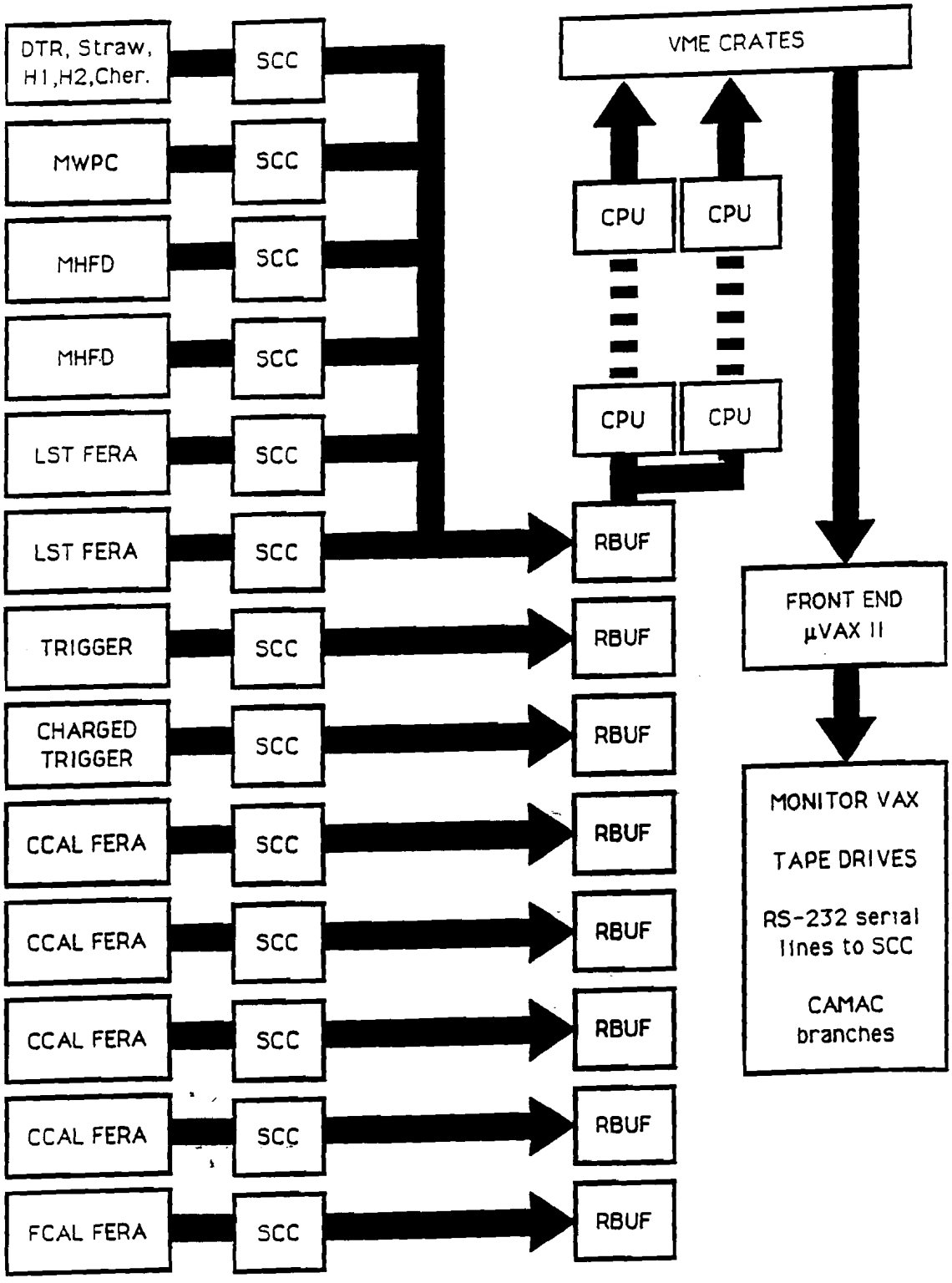

Figure 4.5: Schematic of the E760 read out system.

Chapter 5

The $\chi_{1,2}$ Angular Distributions

The angular distributions for the $\chi_{1,2}$ were determined from data collected during both the 1990 and 1991 runs. The 1990 χ_2 data was analyzed separately from the 1991 χ_2 data. This was done because of the superior quality of the 1991 sample.

Recall from chapter 1 that the angular distribution for the $\bar{p}p \rightarrow \chi_{1,2} \rightarrow J/\psi + \gamma \rightarrow e^+e^- + \gamma$ can be written as a function of three angles θ, θ' and ϕ', which are defined as follows (see also fig. 1.4.1)

- θ: the polar angle of the J/ψ with respect to the antiproton beam, in the center-of-mass system;
- θ': the polar angle of positron with respect to the J/ψ line of flight, defined in the J/ψ rest frame;
- ϕ': the azimuthal angle of the positron in the J/ψ rest frame, where the X' axis is in the plane containing the photon and the antiproton, and $\phi' = 0$ for the antiproton.

Also recall that the χ_1 angular distribution has only has only one free parameter[1]

[1]The particular parameterization for the $\chi_{1,2}$ was chosen so that the parameter estimators would be unbiased.

taken to be a_2 (the quadrupole amplitude) while the χ_2 has three free parameters a_2, a_3, and B_0^2 (the quadrupole, octupole, and the square of the production helicity 0 amplitudes respectively).

5.1 Selection of the Sample

The most important concern in selecting a sample of events for the angular distributions was the need to not introduce any angular biases. To minimize potential biases, the selection described below used only the central calorimeter; other detectors were exploited only at the trigger level. The fiducial volume was also selected to minimize or eliminate any potential biases.

The charged trigger attempted to find e^+e^- pairs that satisfied rough two-body kinematics. The offline event selection took this idea further by fitting to the $\chi_{1,2} \rightarrow J/\psi + \gamma \rightarrow e^+e^- + \gamma$ topology. The selection began by conducting a 2C kinematic fit (see section 6.1 for more details on the kinematic fits), where the inputs were the energies and angles of the two electrons as determined by the CCAL. The acceptance for electrons was limited to $15° < \theta_{lab} < 60°$. Within this region the acceptance for electrons was uniform ($\approx$100%) with the exception of the inefficiency introduced by the Čerenkov septum at $\theta_{lab} \approx 38°$ (see section 5.2.1). The very low background level allowed a low threshold on the kinematic fit probability (CL> 0.001) thus reducing any systematic effects from imperfect knowledge of the calorimeter resolution functions.

In order to reduce the background (discussed in the next section), a cut on the

invariant mass of the e^+e^- pair consistent with three times the mass resolution of the detector was made.

- *For 1990 data :* $2.6GeV/c^2 \leq M_{e^+e^-} \leq 3.6GeV/c^2$
- *For 1991 data :* $2.8GeV/c^2 \leq M_{e^+e^-} \leq 3.4GeV/c^2$

As noted in chapter 4, the larger mass resolution for the 1990 data set was due to the relatively poor energy calibration for 1990. The next cut that was used to reduce background was to cut events that had extra ontime clusters (as defined in chapter 3) in the CCAL. If the kinematic fit placed the photon within the acceptance of the CCAL, then 3 ontime clusters were allowed. If the kinematic fit placed the photon outside the acceptance of the CCAL, then only 2 ontime clusters were allowed. Since extra clusters are uncorrelated with the event, cutting on extra clusters did not introduce an angular bias.

The last three cuts were designed to remove specific kinematic regions that were troublesome. The idea here was to convert regions of inefficiency that would be difficult to parameterize later into simple acceptance cuts. The first cut was to remove events where the photon's angle $\theta_{lab} > 65°$ and thus reduce the background contamination. The second kinematic cut was to remove events where $|\cos\theta'| > 0.95$. This cuts the events where the decay photon and one of the J/ψ electrons could overlap in the CCAL and thus reduce the kinematic fit efficiency. The last kinematic cut required that all the events satisfy the COPL trigger requirement. Recall that COPL was the H2 coplanarity requirement imposed on the $1\check{C}$ and $0\check{C}$ triggers. This last cut was imposed so that the samples from the $2\check{C}$, $1\check{C}$, and $0\check{C}$

triggers could all be added together into a single sample. The final number of events in each sample is summarized in table 5.1.

Sample	Events
1990 χ_1	360
1990 χ_2	405
1991 χ_2	1904

Table 5.1: Number of events in the final sample of $\chi_{1,2}$ events used to fit the angular distributions.

5.1.1 Estimate of Background Contamination

The background to the reaction $\chi_{1,2} \rightarrow J/\psi + \gamma \rightarrow e^+e^- + \gamma$ comes from the enormous non-resonant multi π^0 cross section. A decaying π^0 can produce electrons in two ways:

- **Dalitz decay of the π^0 ($\approx$ 1.2%).**
- **Conversion of a photon in the beam pipe ($\approx$ 2.2%).**

When an event contains two pairs of e^+e^-, they occasionally can fool the trigger and be accepted as a J/ψ. These "fake" events can sometimes have kinematics that are consistent with a $\chi_{1,2}$ event and thus are inadvertently included as background in the sample.

The strategy for removing these background events is simple: either find the π^0s and remove the event or find the events with good $\chi_{1,2}$ kinematics. Cutting on the invariant mass of the J/ψ and on the results of the kinematic fit both seek out events with good kinematics. Cutting events with extra clusters tends to remove

fake events formed from π^0s. The cut $|\cos\theta'| > 0.95$ removes π^0s that decayed symmetrically where one of the photons converted (or Dalitz decayed) and has been mistaken for a single electron.

The background contamination has been estimated by taking data off the resonance of interest and subjecting the background sample to the same selection criteria as the data sample. Table 5.2 summarizes the background sample. The estimate of the background contamination is then found by scaling the observed background cross section by the luminosity in each sample, see table 5.3.

	Energy$_{cm}$ (MeV)	Luminosity (nb^{-1})	Events
1990 Background	≈ 3525	1670	34
1991 Background	≈ 3620	5975	46

Table 5.2: Number of events in the background sample taken off resonance.

	Luminosity (nb^{-1})	Background Events	% Contamination
1990 χ_1	1030	21 ± 4	5.8%
1990 χ_2	1160	24 ± 4	5.9%
1991 χ_2	2576	20 ± 3	1.1%

Table 5.3: Background estimate for the angular distribution samples. Scaled from table 5.2 by luminosity.

5.2 Likelihood Fit to the Data

The Maximum Likelihood Method is used to find the most probable values for the angular distribution parameters[2] α. The probability density describing the shape of

[2]Recall that for the χ_1 there is only one angular distribution parameter a_2 while for the χ_2 there are three parameters a_2, a_3, and B_0^2.

the angular distribution is given by

$$L(\alpha) = \prod_{j=1}^{N_{events}} P_j(\alpha; \Omega_j) \tag{5.1}$$

where Ω_j stands for $(\cos\theta_j, \cos\theta'_j, \phi'_j)$. The probability P_j of getting an event is a function of the undetermined parameters α, and is given by

$$P_j(\alpha; \Omega_j) = \frac{W(\alpha; \Omega_j) \cdot acc(\Omega_j)}{\int W(\alpha; \Omega) \cdot acc(\Omega)\, d\Omega} \tag{5.2}$$

Here W is the theoretical distribution function (Eq. 1.31 or 1.28), $acc(\Omega)$ is the geometric acceptance function, and the integral in the denominator is performed over the entire space.

The difficulty[3] with performing a 3-dimensional integral for each point in space in order to maximize the likelihood function can be overcome if we recall that W can be factorized into angle-dependent and amplitude-dependent terms (see Eq. 1.31 or 1.28). Using this property, the denominator of Eq. 5.2 can be written as

$$\int W(\alpha; \Omega) \cdot acc(\Omega)\, d\Omega = \sum_i K_i(\alpha) \cdot F_i \tag{5.3}$$

where the constants $F_i = \int T_i(\Omega) \cdot acc(\Omega)\, d\Omega$ are independent of the angular distribution parameters, and can be calculated for any acceptance configuration by numerical integration. The acceptance includes those reductions imposed by the Čerenkov septum, the coplanarity cut, and the fiducial volume.

The most likely values of the angular distribution parameters are found by minimizing the negative logarithm of the likelihood function -ln(L), using the CERN program MINUIT [46].

[3]The difficulty has to do only with the computational time required.

In general the maximum likelihood method yields parameter estimates that are normally distributed about the "true" value in the limit of an infinite sample. For small samples the estimators may be biased. In order to check for biases introduced by small samples and also the effects of the detector resolution and acceptance, 300 Monte Carlo experiments were generated for each resonance with small samples (360 events for the χ_1 and 1904 events for the χ_2). The results of the Monte Carlo simulations are summarized in figures 5.1 and 5.2 where the parameter estimates for each experiment are plotted. One can see that the parameter estimates are in fact not biased and are normally distributed about the true values. The true values of the fitted parameters (i.e. inputs to the Monte Carlo) were for the χ_1: $a_2 = -0.14$ and for the χ_2: $a_2 = -0.15$, $a_3 = 0.0$, and $B_0^2 = 0.02$ (these values were chosen because they correspond to the values obtained by fitting the actual data).

When one attempts to fit for an angular distribution in a limited acceptance, the results may be not unique (i.e. additional local maximums may appear in the ln(L) function). The reason for this is clear; if one can look in only a limited angular region, there may well be two or more sets of the parameters α which yield similar distributions within the acceptance. Figures 5.3 and 5.5 plot the ln(L) verses the fit parameters α for the χ_1 and χ_2 respectively from a Monte Carlo simulation where the acceptance was not limited. Figures 5.4 and 5.6 show Monte Carlo simulations where the acceptance of electrons is limited to θ_{lab} between 15° and 60°.

The limited acceptance for electrons in the E760 detector does in fact introduce an appreciable second local maximum into the ln(L) for the χ_2 resonance. This

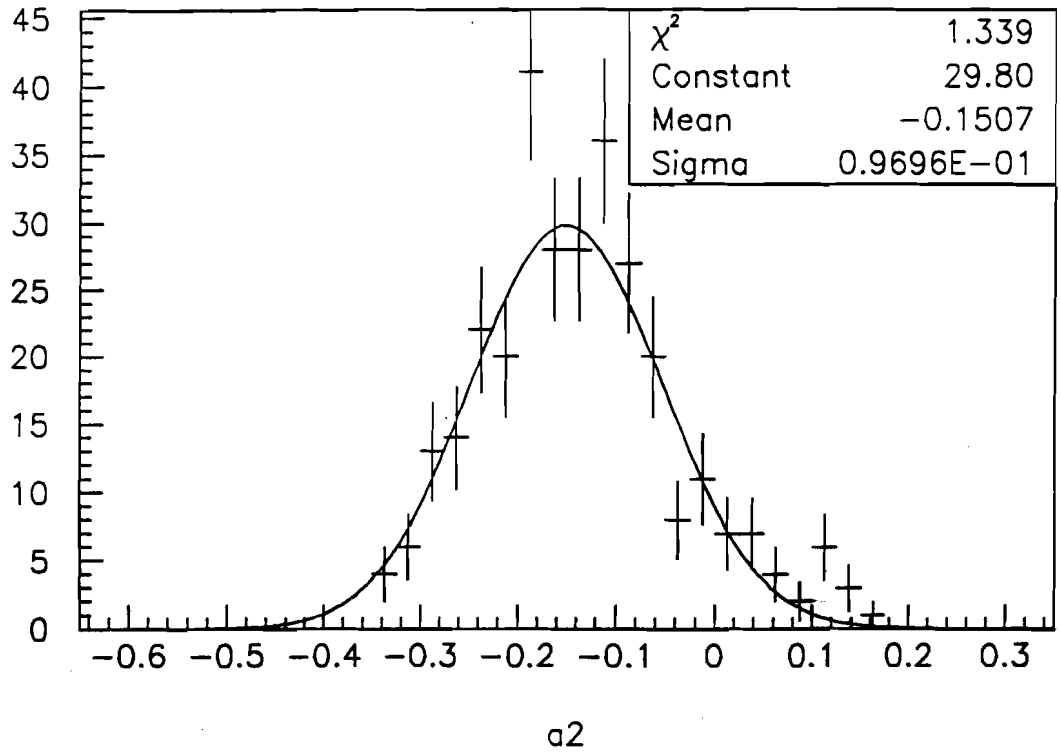

Figure 5.1: Results of 300 Monte Carlo experiments for the χ_1 angular distribution where the input value was $a_2 = -0.14$.

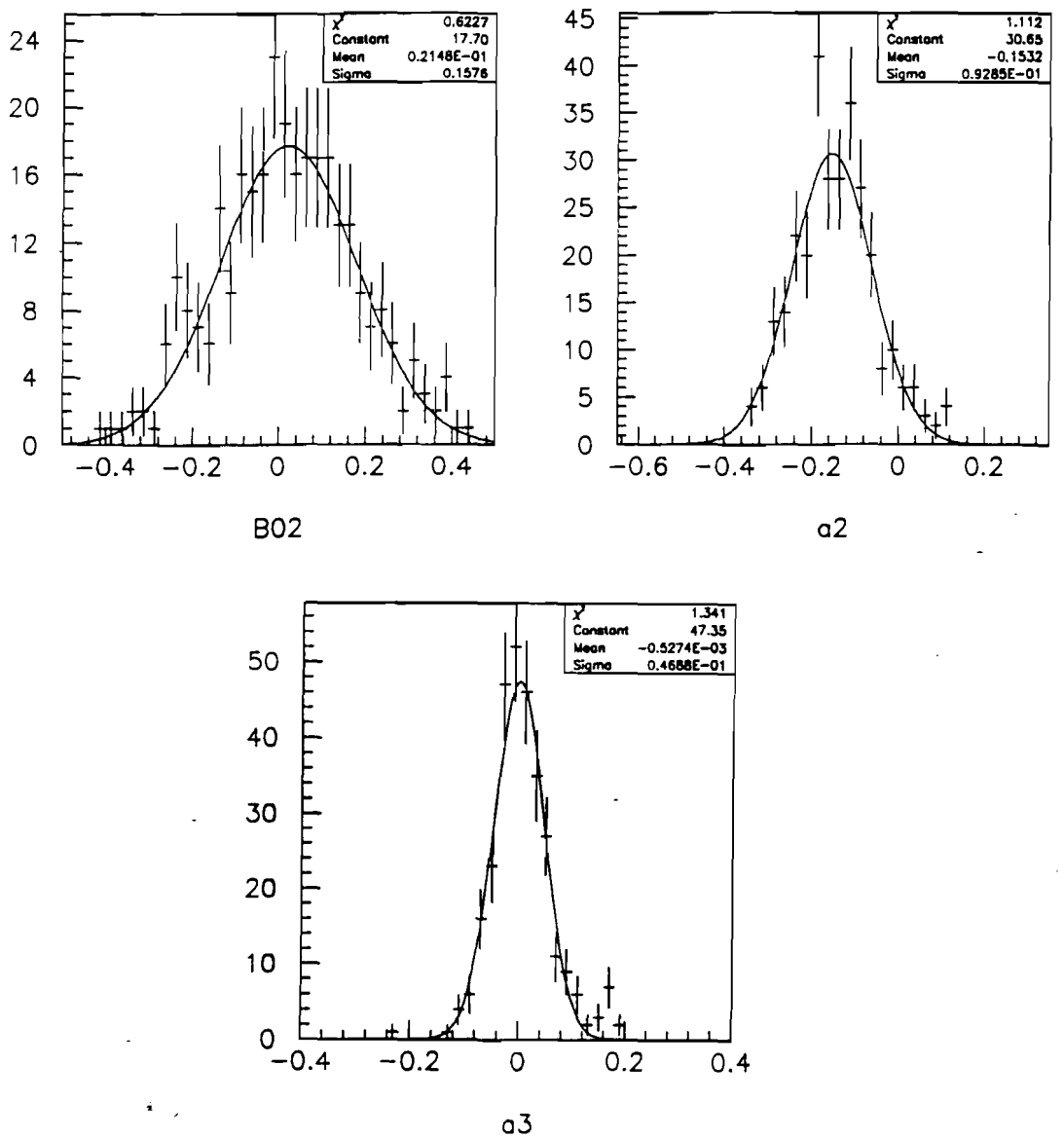

Figure 5.2: Results of 300 Monte Carlo experiments for the χ_2 angular distribution where the input values for the parameters were $a_2 = -0.15$, $a_3 = 0.0$, and $B_0^2 = 0.02$.

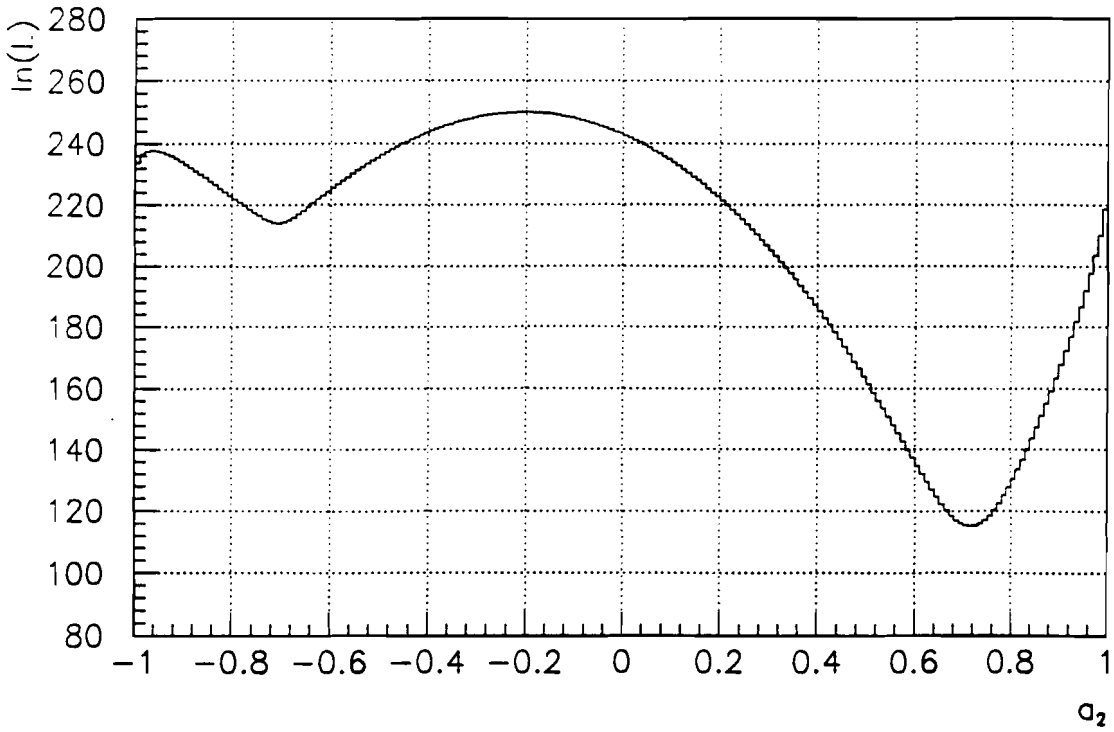

Figure 5.3: ln(L) plot for a fit to a Monte Carlo simulation of the χ_1, no acceptance restrictions were imposed and $a_2 = -0.14$.

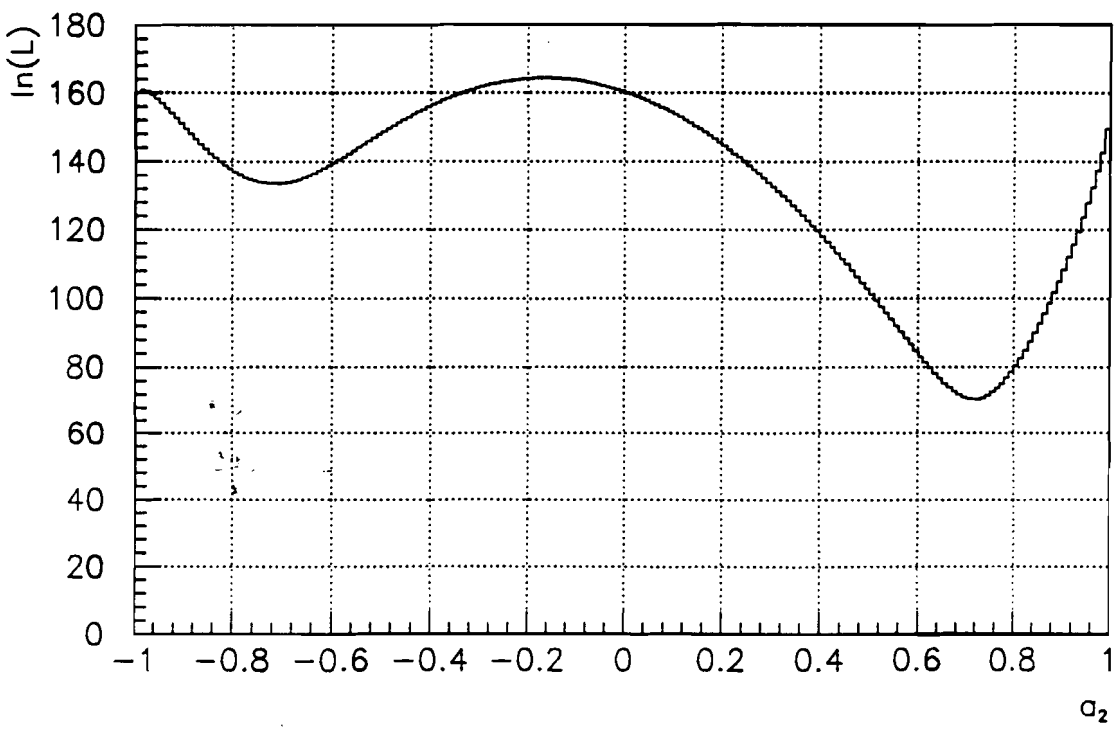

Figure 5.4: ln(L) plot for a fit to a Monte Carlo simulation of the χ_1 where the acceptance for electrons was restricted to $15° < \theta_{lab} < 60°$ and $a_2 = -0.14$.

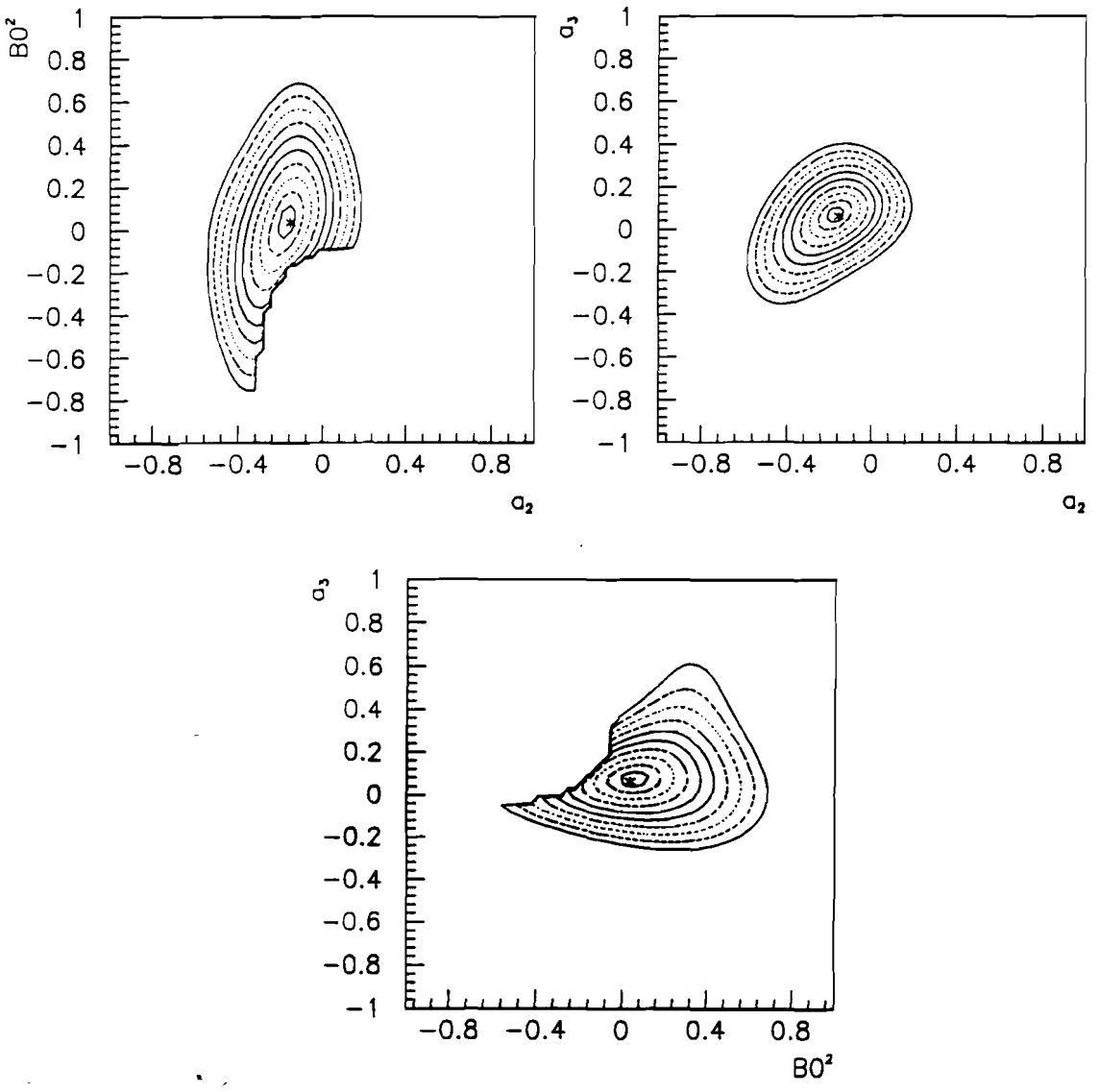

Figure 5.5: Contour plots of ln(L) for a fit to a Monte Carlo simulation of the χ_2, no acceptance restrictions were imposed and $B_0^2 = 0.02$, $a_2 = -0.14$, $a_3 = 0.0$. In each projection the contour lines correspond to 1,2,3...10 standard deviations from the maximum which is indicated by a *. The axis not shown is fixed at its best fit value.

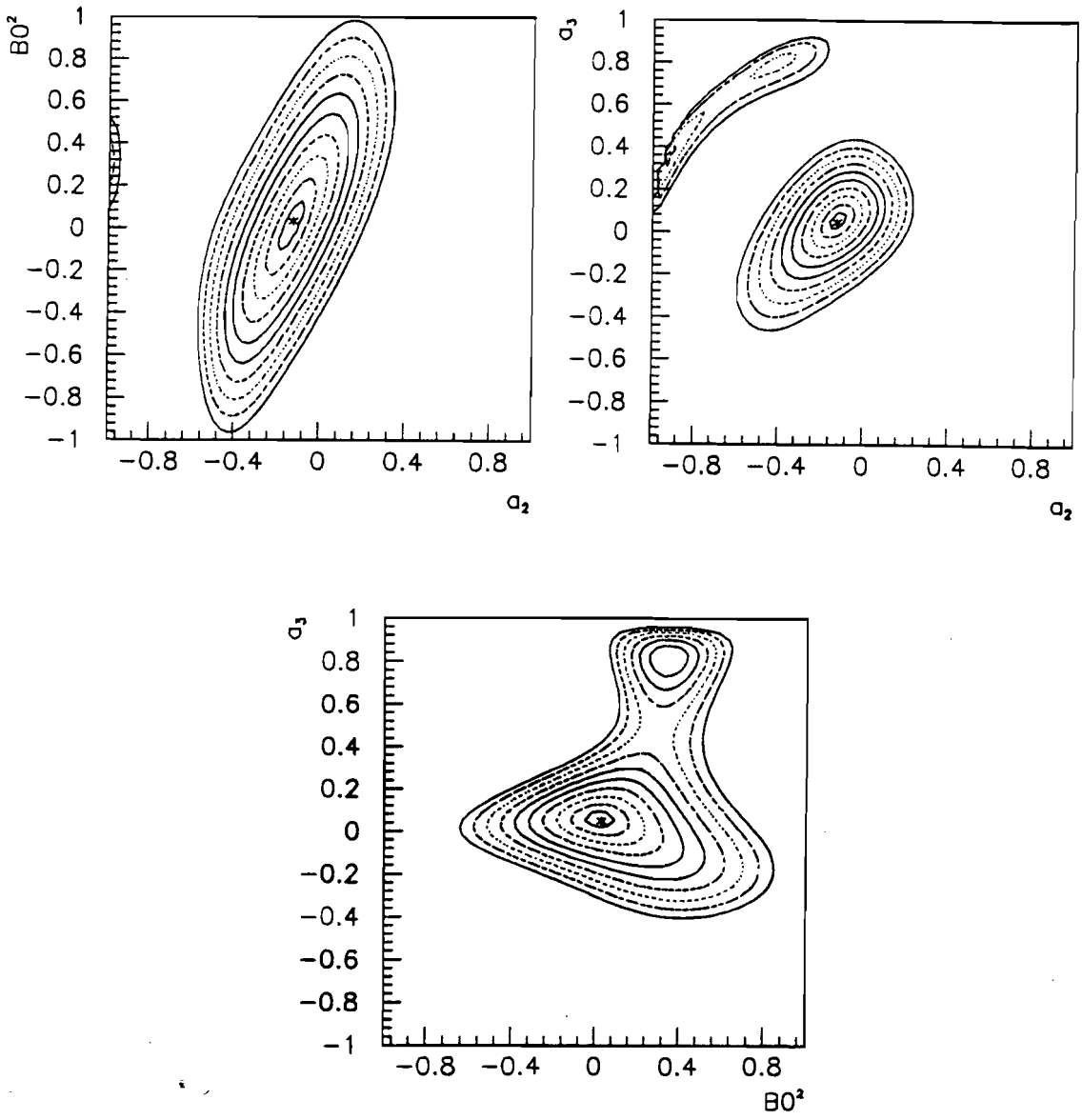

Figure 5.6: Contour plots of ln(L) for a fit to a Monte Carlo simulation of the χ_2 where the acceptance for electrons was restricted to $15° < \theta_{lab} < 60°$ and $B_0^2 = 0.02$, $a_2 = -0.14$, $a_3 = 0.0$. In each projection the contour lines correspond to 1,2,3...10 standard deviations from the maximum which is indicated by a *. The axis not shown is fixed at its best fit value.

second local maximum should not be of great concern for at least two reasons:

- The second local maximum is always (in the 300 Monte Carlo experiments) at least 5 units of ln(L) below the absolute maximum.
- The second local maximum yields the result that $a_2 \approx -1.0$. While such a result is strictly allowed, it would be highly improbable since it would imply that there is very little amplitude for a dipole transition (recall that $a_1^2 + a_2^2 + a_3^2 = 1$).

The χ_1 has a second local maximum again near $a_2 \approx -1.0$ even in the case where we have full acceptance. This maximum can again be excluded by the same considerations as above.

5.2.1 Čerenkov Correction

In order to remove the bias introduced by the inefficiency near the Čerenkov septum, it is necessary to map out the efficiency as a function of θ_{lab}. As previously discussed in 4.2.4, one can use a clean sample of J/ψ data to map out the efficiency. Figures 4.3 and 2.9 show the effect of the Čerenkov septum as a function of the $\cos(\theta_{cm})$ while figure 5.7 shows the detection efficiency for electrons in the Čerenkov as a function of θ_{lab}.

When the 1Č and 2Č triggers are OR'ed together the inefficiency of the Čerenkov septum is improved. If one electron from $\chi_{1,2}$ hits the septum region, the other electron will also hit the septum less than 5% of the time. Table 5.4 gives the efficiency as a function of θ_{lab} when the various triggers are OR'ed together.

θ_{lab}	1990 χ_1 $\epsilon_{\check{C}erenkov}$	1990 χ_2 $\epsilon_{\check{C}erenkov}$	1991 χ_2 $\epsilon_{\check{C}erenkov}$
15.0° *to* 29.0°	1.0	1.0	1.0
29.7°	0.999	0.999	0.999
30.5°	0.998	0.998	0.997
31.2°	0.998	0.998	0.997
31.9°	0.996	0.996	0.995
32.6°	0.996	0.996	0.994
33.4°	0.991	0.991	0.988
34.1°	0.989	0.989	0.986
34.9°	0.985	0.985	0.980
35.7°	0.979	0.979	0.972
36.5°	0.972	0.972	0.962
37.3°	0.969	0.969	0.958
38.1°	0.972	0.972	0.962
39.0°	0.979	0.979	0.972
39.8°	0.985	0.985	0.980
40.7°	0.989	0.989	0.986
41.6°	0.991	0.991	0.988
42.5°	0.996	0.996	0.994
43.5°	0.996	0.996	0.996
44.4°	0.998	0.998	0.997
45.4°	0.998	0.998	0.997
46.4°	0.999	0.999	0.998
47.5° *to* 60.0°	1.0	1.0	1.0

Table 5.4: Efficiency for detection of electrons for $\chi_{1,2}$ decays as a function of θ_{lab} using both the 1$\check{C}$ and 2$\check{C}$ triggers.

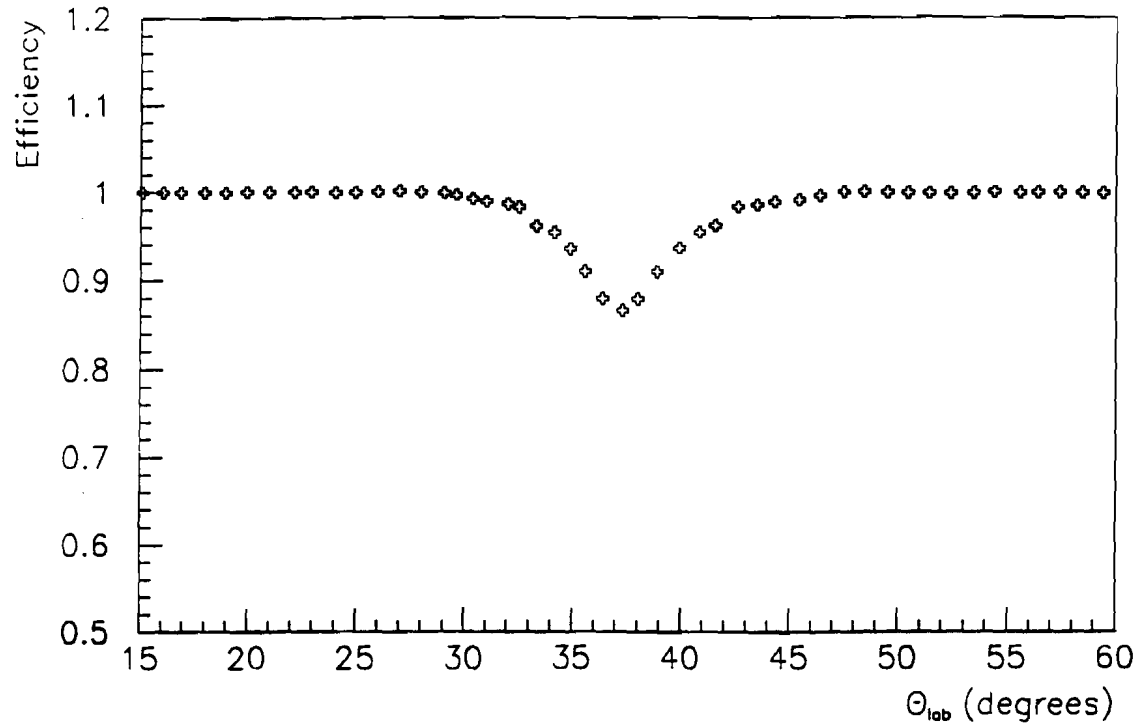

Figure 5.7: Detection efficiency as a function of θ_{lab} for electrons in the Čerenkov.

5.2.2 The Acceptance Constants

The acceptance constants $F_i = \int T_i(\Omega) \cdot acc(\Omega)\, d\Omega$ are calculated by numerically integrating over the entire space. The function $acc(\Omega)$ parameterizes all the acceptance restrictions and is the product of three functions:

$$acc(\Omega) = \alpha_{\text{fiducial}}(\Omega) \cdot \alpha_{\text{coplanarity}}(\Omega) \cdot \alpha_{\text{cerenkov}}(\Omega) \tag{5.4}$$

where

- α_{fiducial} is equal to 1.0 if the event is contained within the fiducial volume defined in the event selection, otherwise it is 0.0.
- $\alpha_{\text{coplanarity}}$ is equal to 1.0 if the event satisfied the coplanarity requirement defined in the trigger, otherwise it is 0.0.

- $\alpha_{\check{C}erenkov}$ is given in table 5.4 where points between entries are linearly interpolated.

The numerical values of the acceptance constants used to fit the angular distributions is given in table 5.5. The overall normalization of these constants is arbitrary.

Acceptance Constant	1990 χ_1	1990 χ_2	1991 χ_2
F_1	10.34648	9.81727	9.78512
F_2	2.78266	2.72373	2.71445
F_3	3.54862	1.45560	1.45058
F_4	0.72407	3.48874	3.47758
F_5	-1.85716	0.72291	0.72073
F_6	——	0.31701	0.31615
F_7	——	-2.31633	-2.30651
F_8	——	-0.45050	-0.44864
F_9	——	-0.17938	-0.17864
F_{10}	——	-1.84924	-1.84108
F_{11}	——	-0.69249	-0.68639

Table 5.5: Acceptance constants for the $\chi_{1,2}$.

5.3 Results and Goodness of Fits

The results of the likelihood fits are shown in table 5.6. The values of the fit parameters are those which maximize the likelihood function. The statistical errors are determined by varying the parameter in question, each time maximizing the likelihood function with respect to the other parameters until the maximum of the likelihood function decreases by a factor of $\exp(-\frac{1}{2})$ [47]. This method yields 68% (asymmetric) confidence intervals for the parameter errors and includes the effects of parameter correlations. The error matrix, which is the inverse of the second

derivative matrix of the function evaluated at the best fit parameter values, is given in table 5.7 for each fit.

Since the value of the likelihood function does not provide a measure of the goodness of fit, Pearson's χ^2 test was applied. The data were binned into $5 \times 5 \times 5 = 125$ bins in $\cos\theta$, $\cos\theta'$ and ϕ', and the χ^2 was calculated as

$$\chi^2 = \sum_{i=1}^{125} \frac{(n_i^{obs} - n_i^{pred})^2}{n_i^{pred}} \tag{5.5}$$

where n_i^{obs} is the observed number of events in the i-th bin and n_i^{pred} is the number of events predicted by a Monte Carlo assuming the values of a_2, a_3 and B_0^2 obtained from the likelihood fit. The χ^2 probability of the fits are summarized in table 5.6.

Sample	a_2 [a]	a_3	B_0^2	χ^2/dof
1990 χ_1	$-0.14^{+0.06}_{-0.06}$	—	—	125.2/124
1990 χ_2	$-0.38^{+0.11}_{-0.07}$	$-0.07^{+0.07}_{-0.06}$	$-0.39^{+0.23}_{-0.20}$	125.7/122
1990 χ_2	$-0.23^{+0.18}_{-0.15}$	$-0.07^{+0.16}_{-0.15}$	$0.00^{+0.38}$ $B_0^2 \geq 0.0$	133.3/122
1991 χ_2	$-0.15^{+0.08}_{-0.07}$	$0.00^{+0.05}_{-0.04}$	$0.02^{+0.13}_{-0.02}$	123.8/122

[a] Recall that $a_2(\chi_1) \neq a_2(\chi_2)$.

Table 5.6: Results of the angular distribution fits.

Figures 5.8-5.10 show the comparison of the data with the fitted function on one-dimensional plots in $\cos\theta$, $\cos\theta'$ and ϕ'. Data points have been corrected for trigger efficiency and acceptance, so they can be compared directly to the theoretical

Sample	a_2, a_2	a_2, a_3	a_2, B_0^2	a_3, a_3	a_3, B_0^2	B_0^2, B_0^2
1990 χ_1	0.0035	—	—	—	—	—
1990 χ_2 fit 2	0.0071	0.0012	0.0093	0.0043	-0.0019	0.0440
1991 χ_2 fit 2	0.0056	0.0021	0.0083	0.0022	0.0027	0.0179

Table 5.7: The error matrix for the angular distribution fits.

distribution function. The solid line shows the function $W(\theta, \theta', \phi')$ with parameters set to the values obtained from the 3-dimensional likelihood fit. The hashed area shows the data before the acceptance corrections.

Generally the fits are all well behaved and have well defined maxima as can be seen from the various contour plots in figures 5.11 through 5.13. However, the 1990 χ_2 does give a non-physical (negative) estimate of the parameter B_0^2. This is not as problematic as it may seem, since the "true" value of B_0^2 is expected to be very close to zero and the 1990 data set is relatively small, random measurement error can easily explain the result. By renormalizing the probability distribution for B_0^2 to include only the physical region [47] and then refitting the data while fixing B_0^2 at the physical bound, one can extract a conservative upper limit on the value of B_0^2. The result of fitting the 1990 χ_2 data with $B_0^2 \geq 0.0$ is given in table 5.6 and is found to be consistent with the measurements from the 1991 data set.

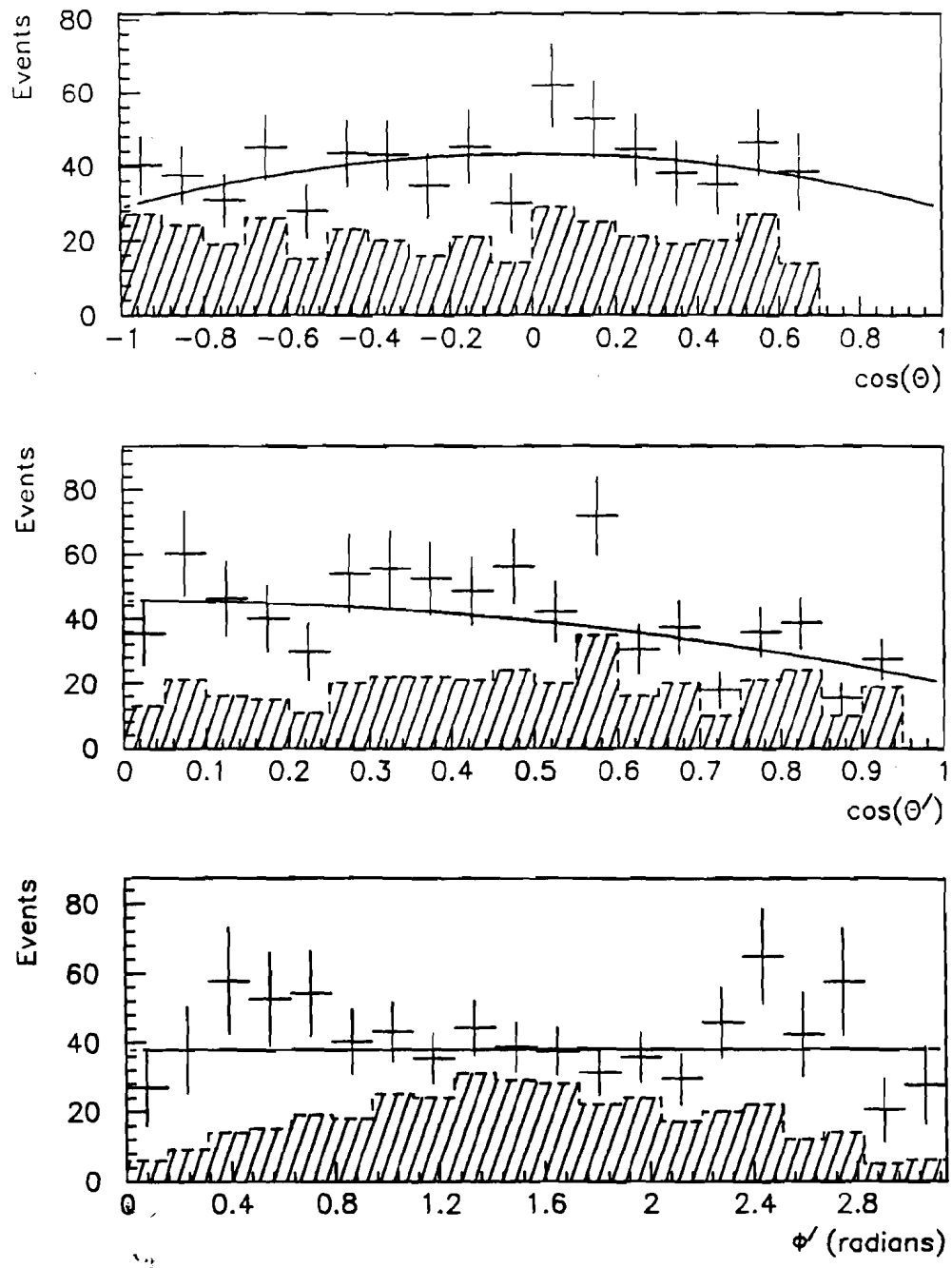

Figure 5.8: Comparison of the 1990 χ_1 data with the theoretical angular distribution function. The data points have been corrected for acceptance and efficiency. The solid line shows the theoretical distribution and the hashed area shows the data before any corrections.

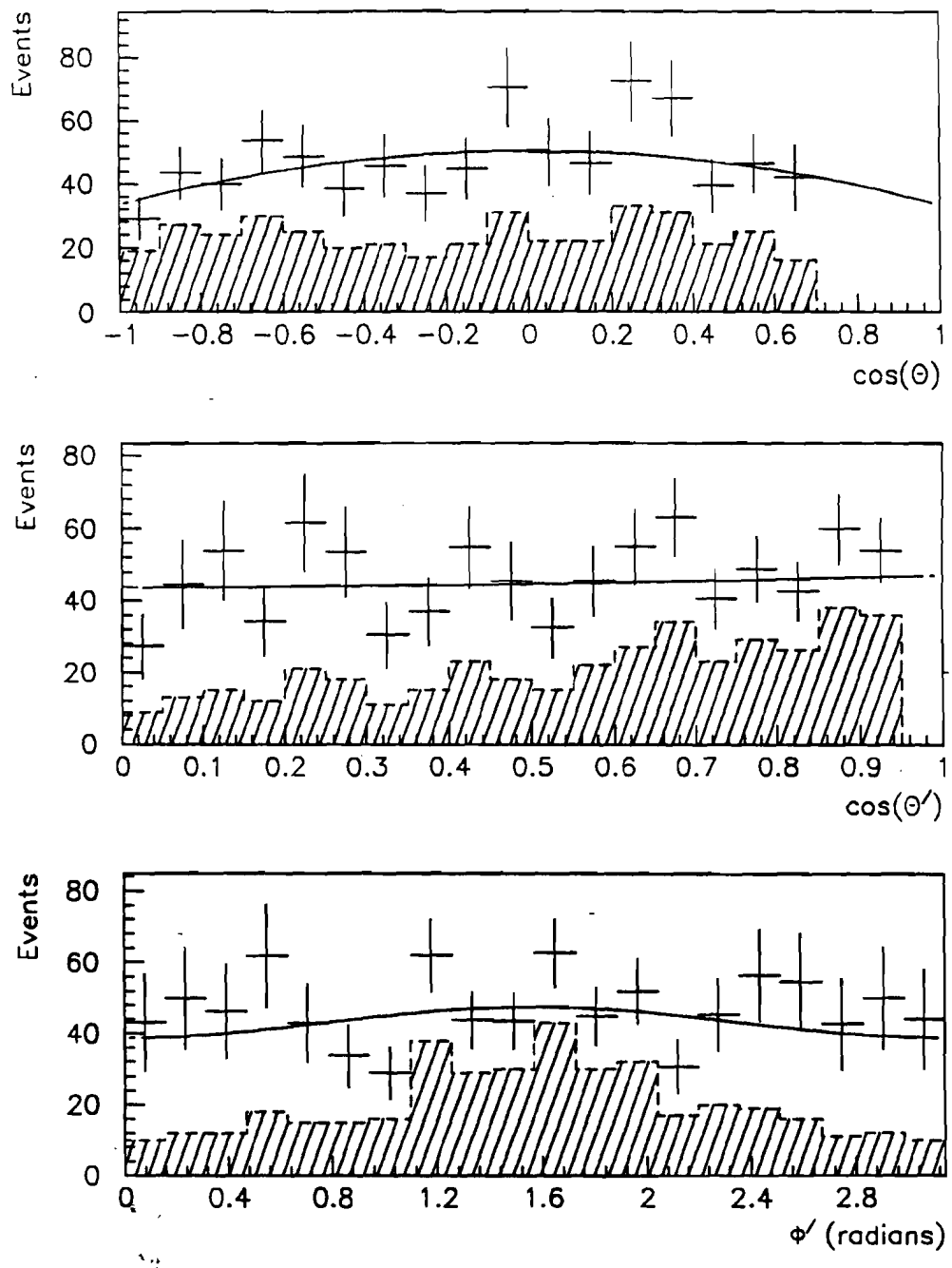

Figure 5.9: Comparison of the 1990 χ_2 data with the theoretical angular distribution function. The data points have been corrected for acceptance and efficiency. The solid line shows the theoretical distribution and the hashed area shows the data before any corrections.

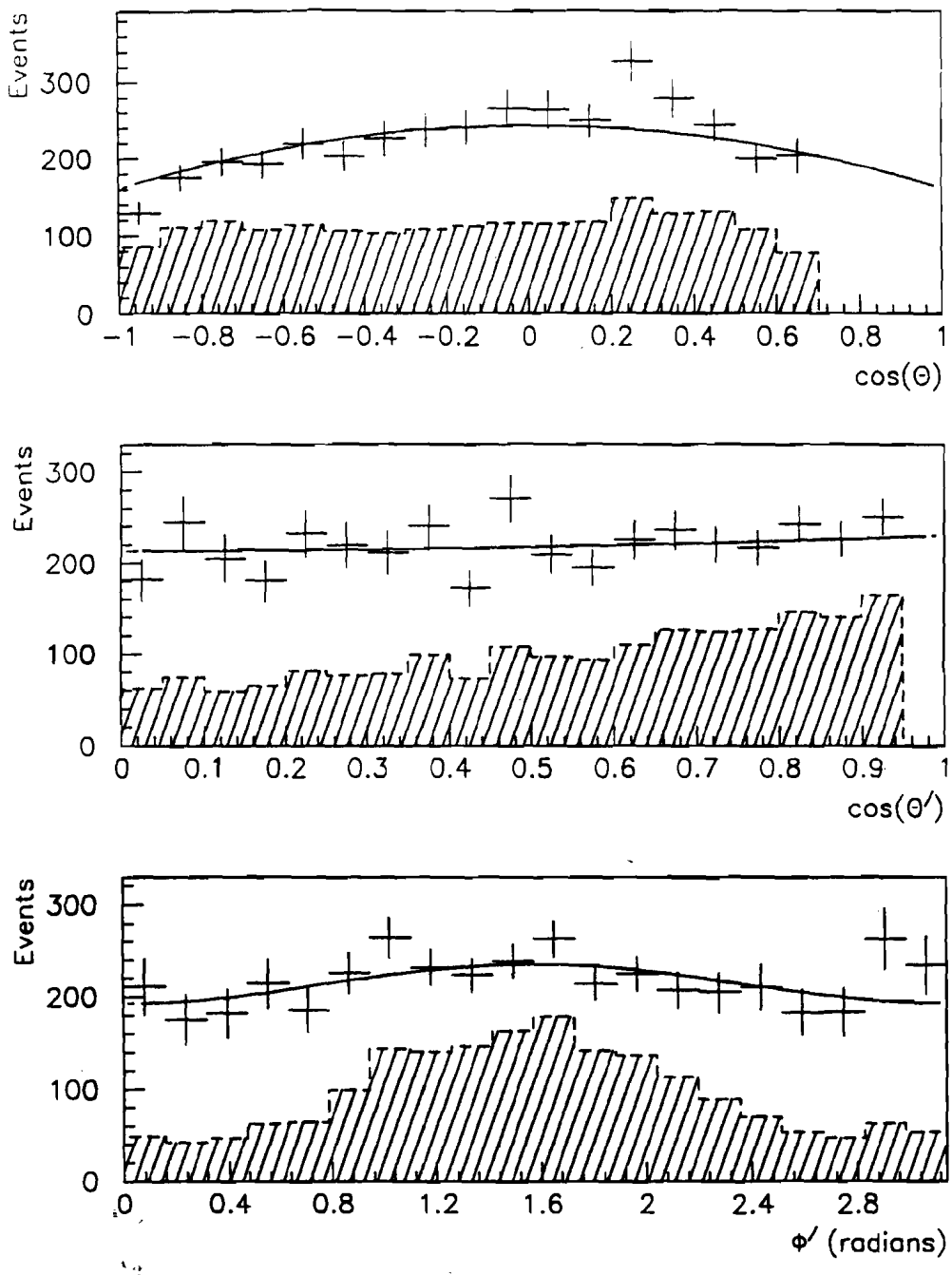

Figure 5.10: Comparison of the 1991 χ_2 data with the theoretical angular distribution function. The data points have been corrected for acceptance and efficiency. The solid line shows the theoretical distribution and the hashed area shows the data before any corrections.

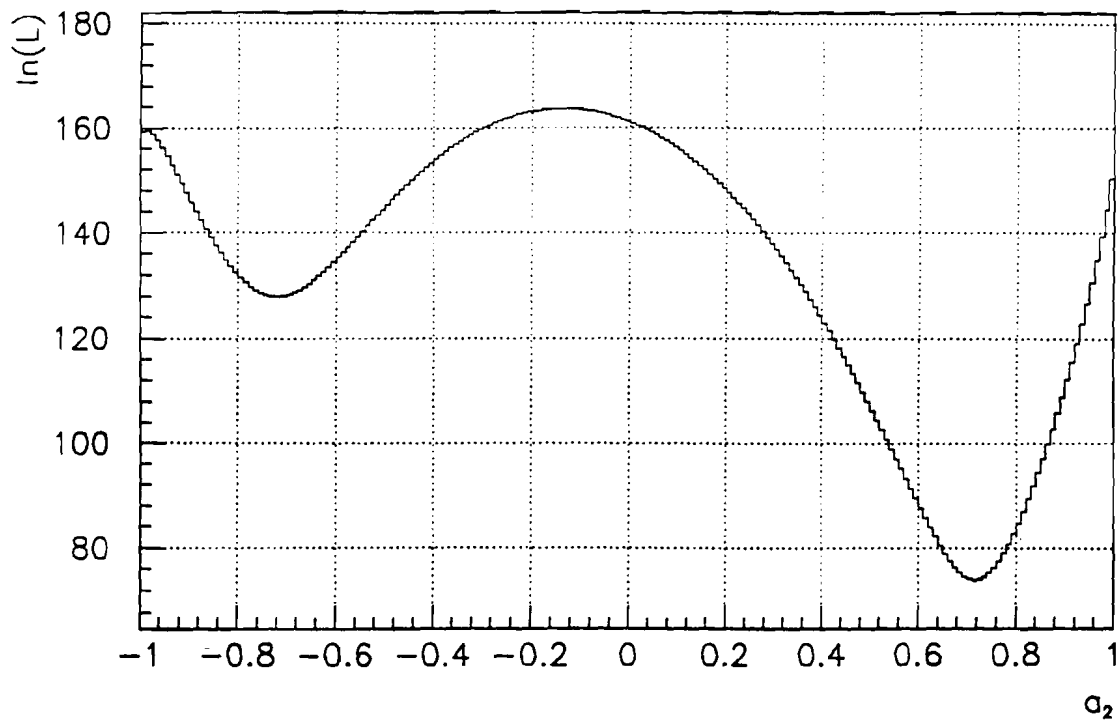

Figure 5.11: ln(L) plot for the fit to the 1990 χ_1 angular distribution.

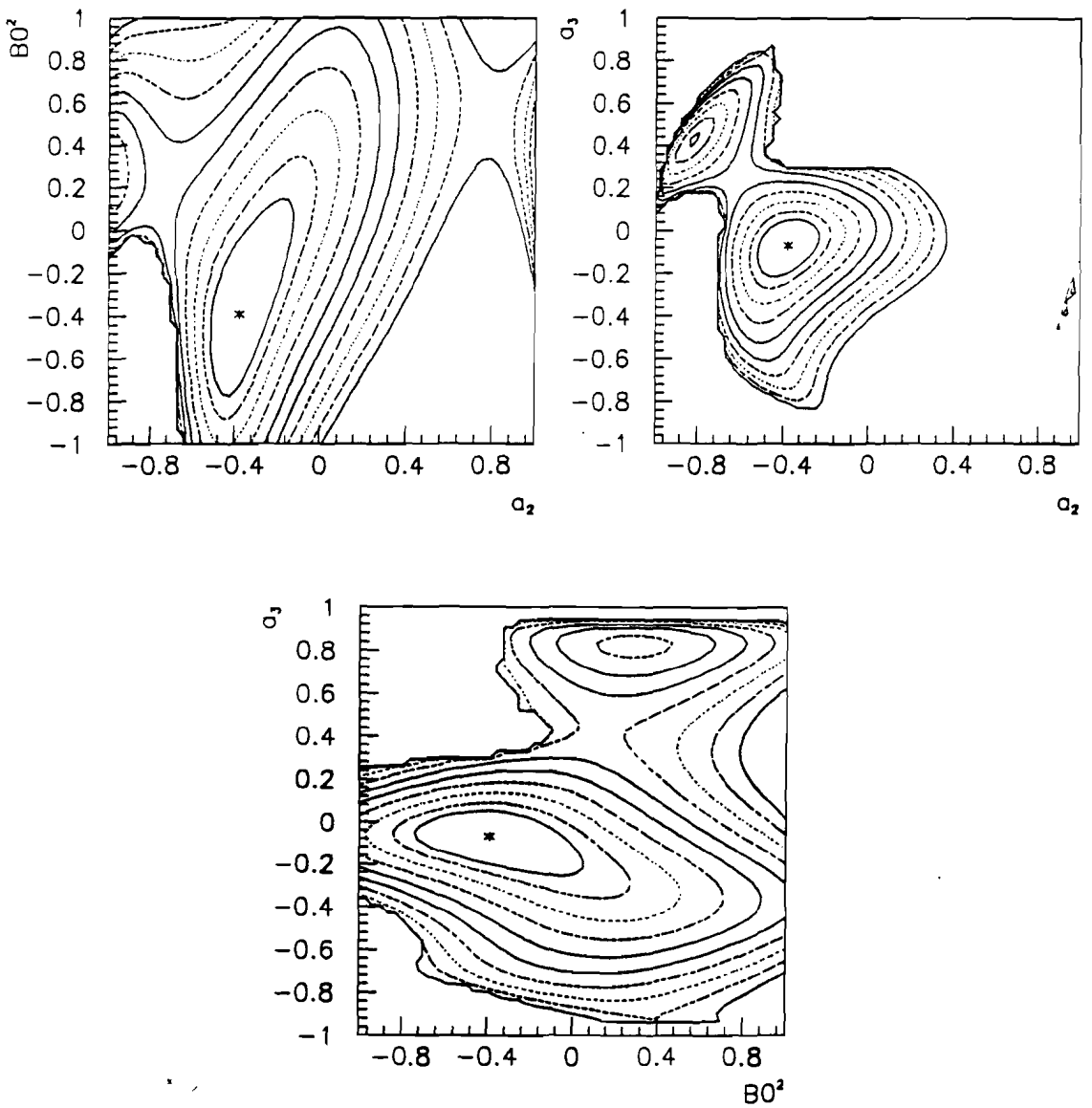

Figure 5.12: Contour plots of ln(L) from the fit to the 1990 χ_2 angular distribution. In each projection the contour lines correspond to 1,2,3...10 standard deviations from the maximum which is indicated by a *. The axis not shown is fixed at its best fit value.

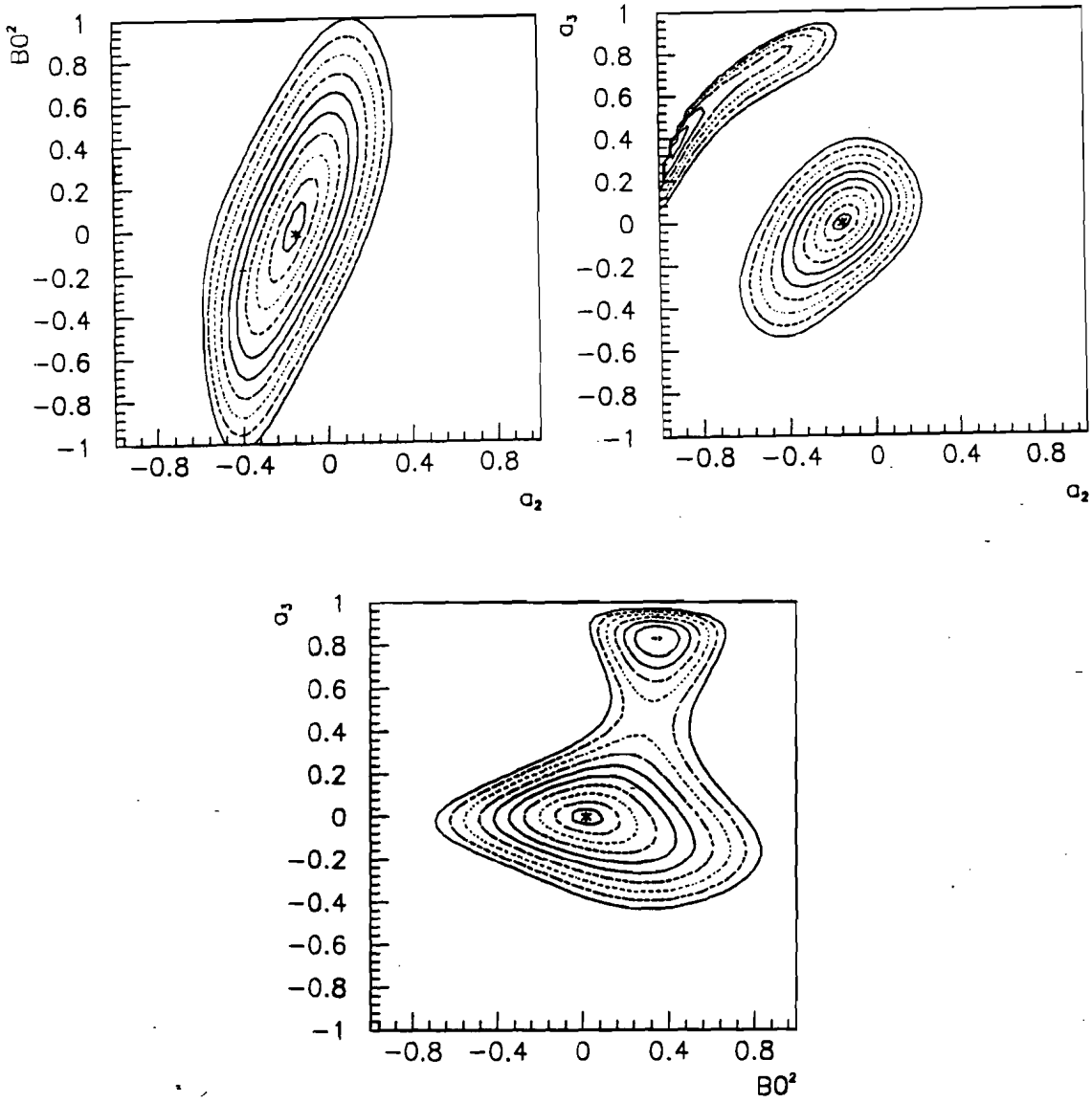

Figure 5.13: Contour plots of ln(L) from the fit to the 1991 χ_2 angular distribution. In each projection the contour lines correspond to 1,2,3...10 standard deviations from the maximum which is indicated by a *. The axis not shown is fixed at its best fit value.

Chapter 6

Resonance Parameters for the χ_1 and χ_2

During the summer of 1990 two scans of each resonance were conducted. Each scan consisted of about 7 or 8 points separated in center-of-mass energy ($W = \sqrt{s}$) by $\approx$ 250 keV. At each point the cross section for the reaction $\bar{p}p \rightarrow \chi_{1,2} \rightarrow J/\psi + \gamma \rightarrow e^+e^- + \gamma$ is measured and an excitation curve (cross section versus the center of mass energy) is constructed. The resonance parameters are then extracted from the excitation curve by a deconvolution of the resonance profile and the center-of-mass energy distribution of the beam.

6.1 Event Selection

Since the data used to fit the resonance parameters were taken during a scan where the instantaneous luminosity varied from $\sim$ 8×10^{30} cm^{-2} s^{-1} to $\sim$ 2×10^{30} cm^{-2} s^{-1}, the cuts used to select the sample were chosen to be insensitive to the instantaneous luminosity. In order to be as efficient as possible, the event

selection concentrated on finding the e^+e^- pair from the decaying J/ψ. There were no restrictions placed on the photon acceptance. As before, the selection relies primarily on a 2C kinematic fit to the reaction $\bar{p}p \rightarrow \chi_{1,2} \rightarrow J/\psi + \gamma \rightarrow e^+e^- + \gamma$ to find candidate events. After the events have been identified by the kinematic fit, a series of cuts is applied in order to identify those events with "good" electrons tracks. The term "good" refers to single electron tracks as opposed to the double electron tracks from π^0s with a photon conversion or Dalitz decay. The specific cuts used in this selection are listed below and each cut will be discussed in detail in the following sections:

- *Kinematic Fit – Each event was fitted to the* $\bar{p}p \rightarrow \chi_{1,2} \rightarrow J/\psi + \gamma \rightarrow e^+e^- + \gamma$ *hypothesis where the inputs to the 2C fits are the electron energies and positions of the electrons as determined by the CCAL. The fiducial volume over which electrons were accepted was restricted to* $15° < \theta_{lab} < 60°$. *No information on the decay photon was required. In order to pass the fit, an event had to have a confidence level greater than 0.1%. See figure 6.1 for a plot of the confidence level for* $\chi_{1,2}$ *events in the final sample.*

- *J/ψ Invariant Mass – Every* e^+e^- *pair candidate was required to have an invariant mass of between* $2.6 GeV/c^2$ *and* $3.6 GeV/c^2$ *(see section 5.1).*

- *Cluster Mass – The cluster mass is defined on a 5x5 grid of CCAL blocks about the central block of a cluster by the relation:*

$$m = \sqrt{\left(\sum_i E_i\right)^2 - \left(\sum_i \vec{p}_i\right)^2} \tag{6.1}$$

where the sums are over CCAL blocks and the momentum vector corresponding to each block and is directed toward the center of that block. The idea behind this definition for the cluster mass was to identify π^0s that had decayed symmetrically. Such π^0s would have both photons hit the CCAL so close as to be unresolvable as two distinct hits. By requiring that both electron tracks have cluster masses less than $95MeV/c^2$, electrons (isolated single showers) could be separated from symmetric π^0s (overlapping showers) which would tend to have a cluster mass of $\approx 135MeV/c^2$. The cluster mass cut was very efficient at separating electrons from symmetrically decaying π^0s (see figure 6.2).

- *π^0 Cut – In order to find the asymmetric π^0 component of the background, a cut was made on the invariant mass of every combination that could be formed between the "electrons" and other clusters in the event. If a mass consistent with a π^0 ($80MeV/c^2 < I_{mass} < 180MeV/c^2$) was found, then the event was removed from the sample.*

The results of the above event selection are summarized in table 6.1. The effect of the various cuts on the data can be seen in graphical form in figures 6.3 through 6.6.

	Events in Final Sample	Integrated Luminosity (nb^{-1})
First χ_1 Scan	245	525.8
Second χ_1 Scan	238	500.0
First χ_2 Scan	186	474.9
Second χ_2 Scan	370	698.8

Table 6.1: Events and luminosity for the final sample used to fit for resonance parameters.

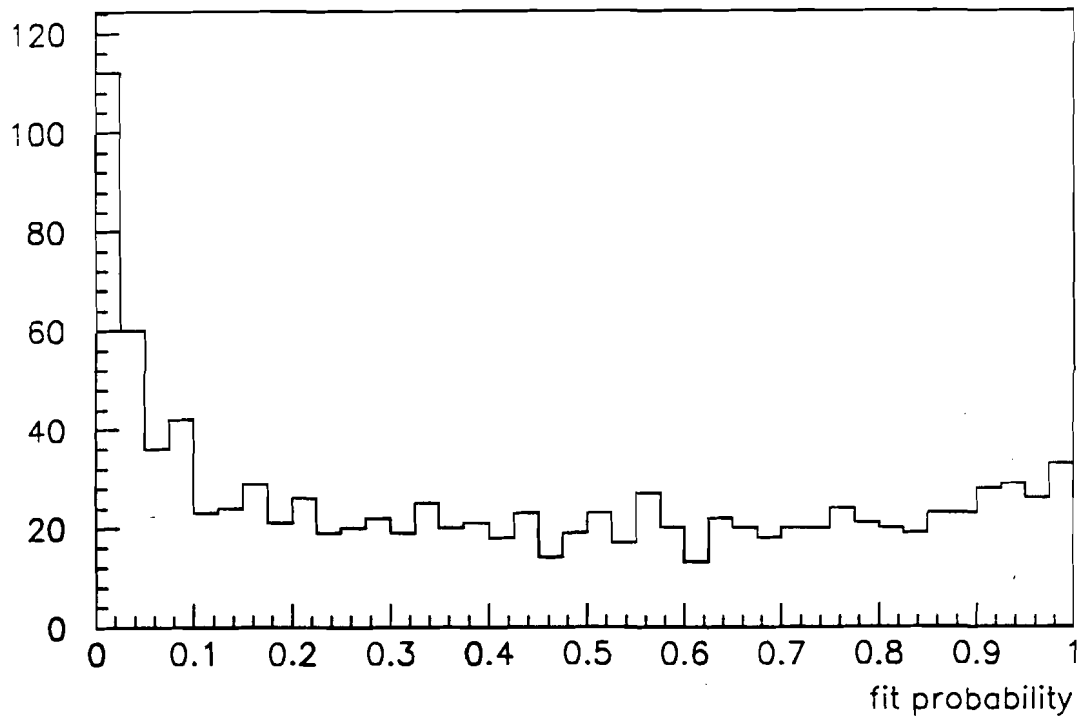

Figure 6.1: Plot of confidence level from the kinematic fit for the $\chi_{1,2}$ events in the final event sample.

6.1.1 Selection Efficiency

In order to study the efficiency of the selection detailed above, two "clean" (background free) samples of $\chi_{1,2}$ events were generated. The first clean sample did not use any kinematic information and was obtained by using the following selection:

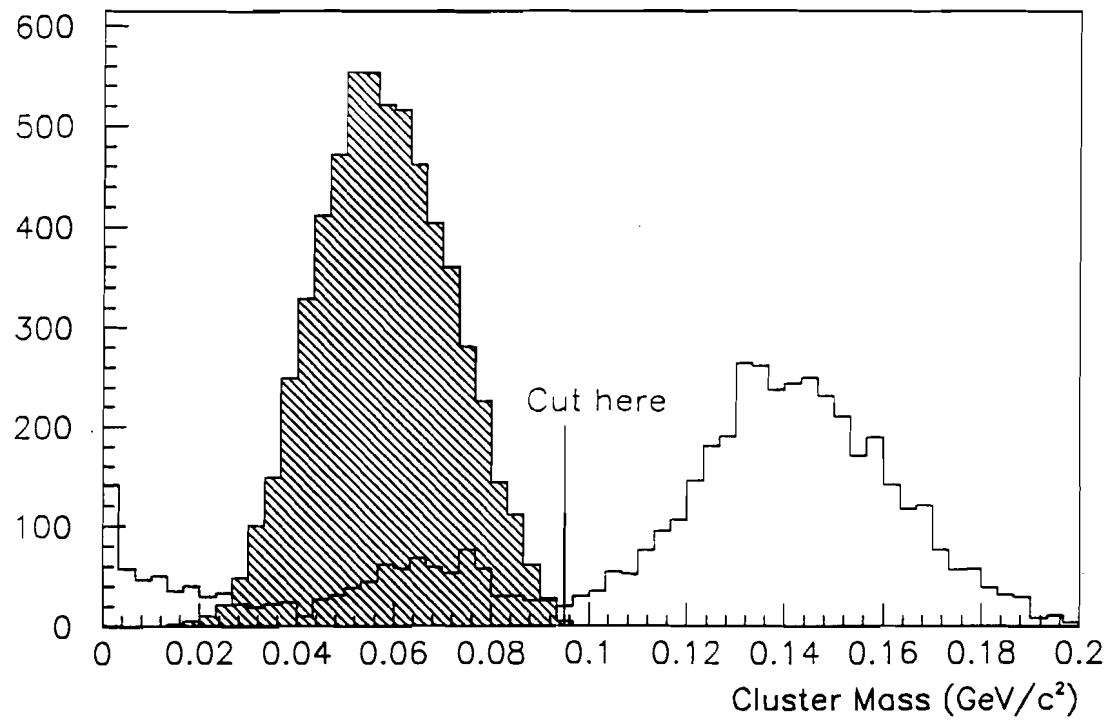

Figure 6.2: The shaded histogram shows the cluster mass for a clean sample of electron showers, the unshaded histogram shows the cluster mass for a sample of π^0 events.

- *Cluster Mass – As defined above.*
- *π^0 Cut – As defined above.*
- *H2 MIP – Requires that each electron track be consistent with a single electron in the scintillator hodoscope H2 (i.e. $H2_{MIP} < 1.5$).*
- *Čerenkov Cut – Requires that each electron track be consistent with a single electron in the Čerenkov*

This sample was then used to estimate the efficiency of the Kinematic Fit and the J/ψ Mass requirements. The second clean sample did not attempt to identify events with π^0 contamination and was obtained by using the follow selection:

- *Kinematic Fit – Cut on fit confidence level equal 10%.*

- *J/ψ Mass – As defined above.*

- *H2 MIP – As defined above.*

- Čerenkov *Cut – As defined above.*

This second sample was then used to estimate the efficiency of the Cluster Mass and π^0 Cut requirements.

	Events in Test Sample	Events After Cuts	Efficiency
Test Sample 1	745	694	0.932 ± 0.009
Test Sample 2	653	558	0.855 ± 0.014

Table 6.2: Events used to determine the selection efficiency.

The overall efficiency of the event selection is simply given by the product of the individual cut efficiencies from table 6.2:

- *For 1990* $\chi_{1,2}$: $\epsilon_{analysis} = 0.797 \pm 0.015$

One hazard that can be encountered in determining the efficiencies by the method outlined above is that the selection criteria may not be independent. This may occur if background events contaminate the sample. To minimize this possibility, the two samples used above have been extracted by using very tight cuts. The maximum number of background events in each test sample has been estimated to be at most 3-4 events. The efficiency of the analysis has also been cross checked by using a combination of Monte Carlo simulations and electron data taken at the J/ψ resonance. The results of the alternate efficiency determination are consistent with those quoted here.

6.1.2 Estimate of Backgrounds

As before, the background has been estimated by applying the event selection to off resonance data. In 1990 there were $\approx 1670\ pb^{-1}$ of data collected in the vicinity of the $\chi_{1,2}$. The estimated background cross section to $\chi_{1,2} \rightarrow J/\psi + \gamma \rightarrow e^+e^- + \gamma$ from non-resonant sources (see section 5.1.1 for a discussion of the background sources) is summarized in table 6.3.

E_{cm} (MeV)	Luminosity (pb^{-1})	Background Events	Background Cross Section (pb)
≈ 3525	1250	40	32.0 ± 5.1
≈ 3505	420	18	42.9 ± 10.1

Table 6.3: Estimate of background contamination.

The effect of the various cuts on the background can be seen in graphical form in figures 6.3 through 6.5. The figures show the reconstructed mass of the e^+e^- from the total sample of $\chi_{1,2}$ events collected during the 1990 scans as the open area, while the equivalent background is shown as the shaded area. Figure 6.6 is from a 1990 sample of $\bar{p}p \rightarrow J/\psi \rightarrow e^+e^-$ shown for comparison. Since the background in the vicinity of the $\chi_{1,2}$ is consistent with being flat [48], one can combine the data from table 6.3 and find the background to be 34.7 ± 4.6 (pb).

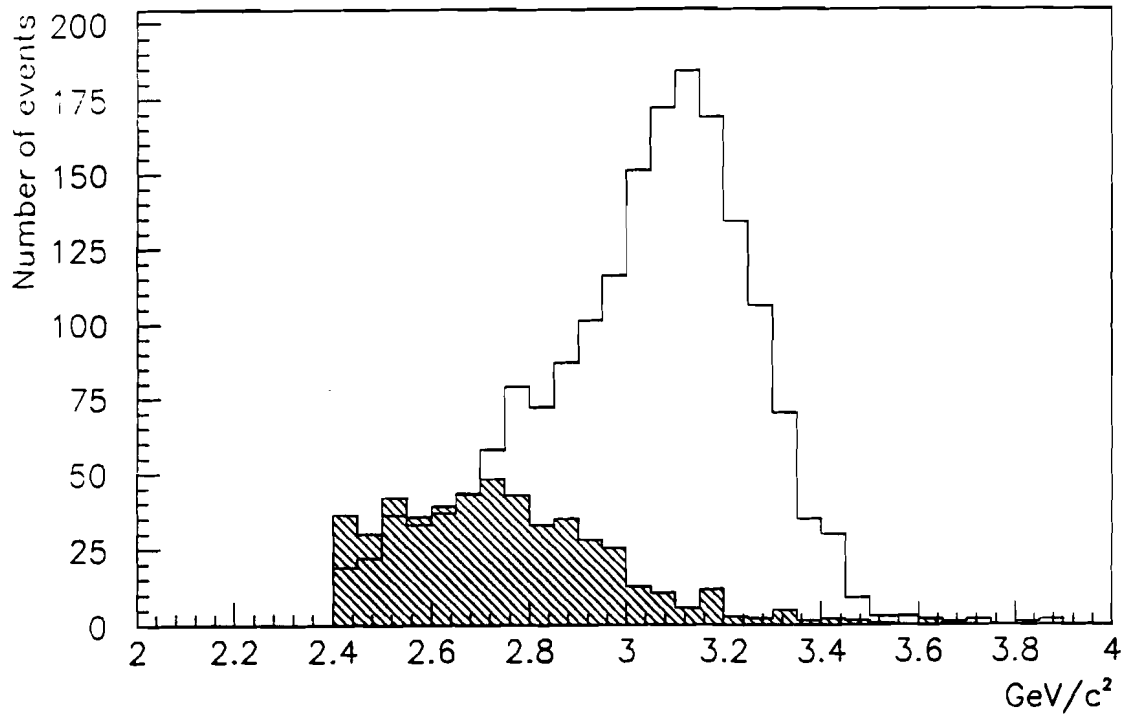

Figure 6.3: 1990 $\chi_{1,2}$ sample after selection with kinematic fit, the open area is the data while the shaded area is the luminosity scaled background.

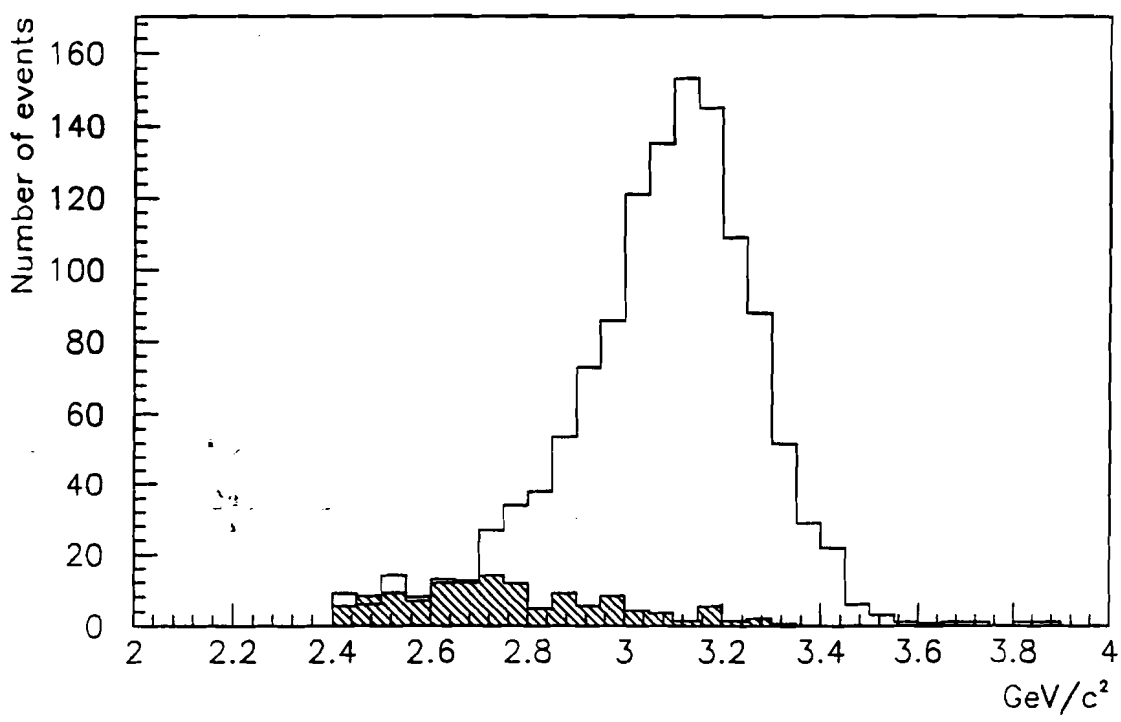

Figure 6.4: 1990 $\chi_{1,2}$ sample after selection with π^0 cuts, the open area is the data while the shaded area is the luminosity scaled background.

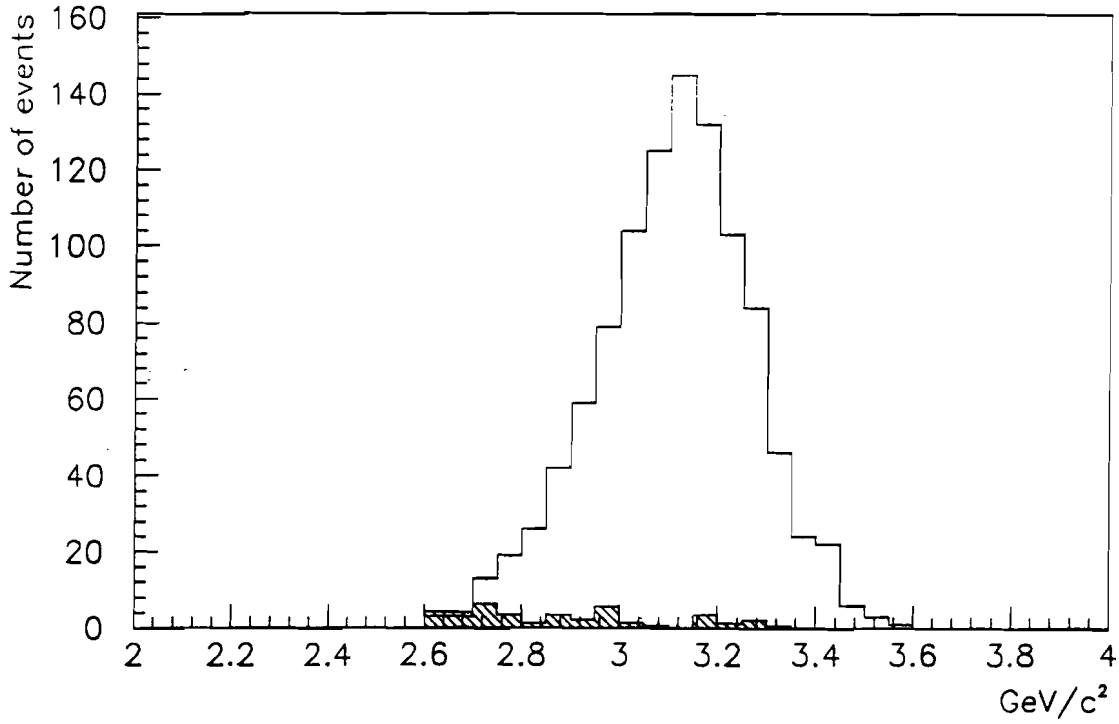

Figure 6.5: 1990 $\chi_{1,2}$ sample after selection with J/ψ invariant mass cut, the open area is the data while the shaded area is the luminosity scaled background.

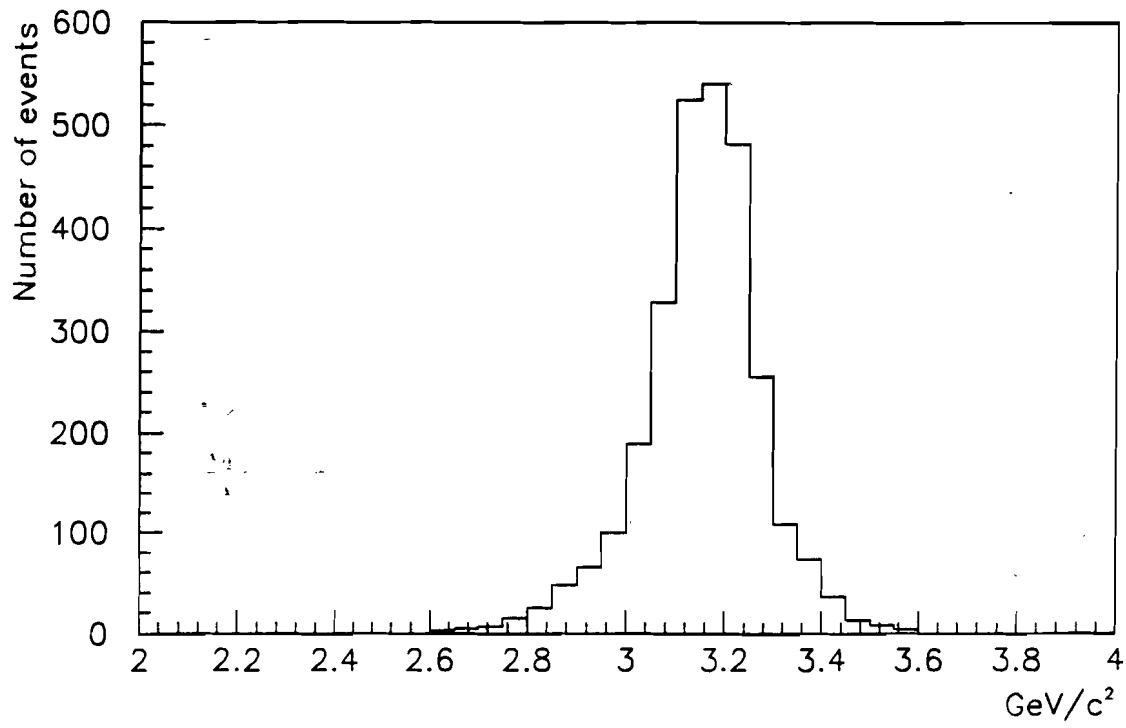

Figure 6.6: 1990 clean J/ψ sample, shown for comparison.

6.1.3 Acceptance

The geometrical acceptance was calculated using the measured angular distributions (see chapter 5) and integrating equation 5.3 over the allowed fiducial volume (i.e. the e^+e^- must be within $15° < \theta_{lab} < 60°$). For the χ_1, using $a_2 = -0.14^{+0.06}_{-0.06}$ as determined from the 1990 data, the acceptance was found to be $\alpha_{geom}(\chi_1) = 0.62 \pm 0.01$. For the χ_2, using $a_2 = -0.15^{+0.06}_{-0.06}$, $a_3 = 0.00^{+0.05}_{-0.04}$, and $B_0^2 = 0.02^{+0.13}_{-0.02}$ as determined from the 1991 data, the acceptance was found to be $\alpha_{geom}(\chi_2) = 0.625 \pm 0.007$.

6.2 Fitting the Excitation Curves

The Maximum Likelihood Method is used to find the most probable values for the resonance (R, either the χ_1 or χ_2) parameters. The probability density describing the resonance is given by the product of N (number of data point in the excitation curve) Poisson functions where n_j is the number of events observed and ν_j is the number of events expected for the jth data point:

$$L(M_R, \Gamma_R, A_R) = \prod_{j=1}^{N} \frac{\nu_j^{n_j} e^{-\nu_j}}{n_j!} , \tag{6.2}$$

where

$$\nu_j = \left[\int \mathcal{L}\, dt\right]_j \left(\sigma_{bckg} + \epsilon \int f_j(W)\sigma_{peak} \frac{\Gamma_R^2}{4(W - M_R c^2)^2 + \Gamma_R^2} dW\right) . \tag{6.3}$$

The first factor in equation 6.3 is the integrated luminosity for each point corrected for dead time, ϵ is the overall acceptance and efficiency, σ_{bckg} is the background

cross section to the reaction $\chi_{1,2} \rightarrow J/\psi + \gamma \rightarrow e^+e^- + \gamma$, the integral over dW is the convolution of the resonance Breit-Wigner with the center-of-mass energy distribution function $f_i(W)$, and

$$\sigma_{peak} = \frac{4\pi(\hbar c)^2(2J_R+1)}{W^2 - 4m^2c^4} \times BR(R \rightarrow \bar{p}p) \times BR(R \rightarrow J/\psi\gamma) \times BR(J/\psi \rightarrow e^+e^-). \tag{6.4}$$

The fitted parameters are then the mass of the resonance M_R, the width of the resonance Γ_R, and the product

$$A_R = \Gamma(R \rightarrow \bar{p}p) \times BR(R \rightarrow J/\psi\gamma) \times BR(J/\psi \rightarrow e^+e^-). \tag{6.5}$$

Recall from chapter 3 that the center-of-mass energy distribution function $f_i(W)$ is derived from the measured $\bar{p}$ revolution frequency spectrum and the machine parameter η. These spectra were collected approximately every 3 minutes and are fit to a gaussian shape (see figure 2.3). From the average value of the mean revolution frequency ν_{beam_j} and the frequency spread $\sigma(\nu_{beam_j})$ one can calculate the average beam energy E_{beam_j} and the average beam energy spread $\sigma(E_{beam_j})$ which are inputs to the fit for each point. The input data to the fits are summarized in tables 6.4 and 6.5.

6.3 Results and Goodness of Fits

The best fit parameters (i.e. those which maximize the likelihood function) are given in table 6.6. As before, the statistical errors for each parameter are determined by varying that parameter while minimizing with respect to the others until

$(\int \mathcal{L}dt)_j$ (nb^{-1})	E_{beam_j} (MeV)	$\sigma(E_{beam_j})$ (MeV)	$Events_j$
4.95	3511.190	0.2390000	2
20.84	3510.183	0.2574726	8
60.81	3511.883	0.3887261	8
70.96	3510.818	0.3518787	42
49.38	3510.207	0.3215861	45
71.83	3511.334	0.3865435	22
89.34	3510.552	0.3422702	72
74.90	3509.912	0.3461901	30
82.78	3509.153	0.3041579	16
99.15	3510.360	0.2145134	65
57.66	3511.405	0.2442274	10
57.72	3511.063	0.2427069	29
72.93	3510.613	0.2098470	65
68.56	3510.010	0.1924237	41
78.35	3509.710	0.1664277	13
65.59	3509.477	0.1511259	15

$\sigma_{bckg}(\chi_1) = 34.7 \pm 4.6\ (pb)$

$\epsilon(\chi_1) = \alpha_{geom} \times \epsilon_{trig} \times \epsilon_{anal} = 0.41 \pm 0.02$

Table 6.4: Summary of the data used to fit the χ_1 resonance. The first 9 entries are from scan#1 while the last 7 are from scan#2.

$(\int \mathcal{L}dt)_j$ (nb^{-1})	E_{beam_j} (MeV)	$\sigma(E_{beam_j})$ (MeV)	$Events_j$
62.52	3556.086	0.2740969	60
60.60	3564.783	0.3449742	2
58.46	3561.976	0.3554209	1
48.85	3560.241	0.2876225	5
48.83	3558.484	0.2581608	10
47.09	3556.152	0.2248407	37
37.30	3555.794	0.2741922	36
55.99	3554.928	0.2646450	26
40.57	3554.287	0.2617296	9
53.22	3557.656	0.2811202	11
52.70	3557.735	0.2891161	9
80.40	3557.069	0.3157344	55
83.06	3556.164	0.2365364	63
83.95	3555.767	0.2168579	68
90.43	3555.165	0.2067516	62
87.70	3554.939	0.2144972	47
87.28	3554.160	0.1921999	12
80.06	3557.061	0.2297101	43

$\sigma_{bckg}(\chi_2) = 34.7 \pm 4.6\ (pb)$

$\epsilon(\chi_2) = \alpha_{geom} \times \epsilon_{trig} \times \epsilon_{anal} = 0.41 \pm 0.02$

Table 6.5: Summary of the data used to fit the χ_2 resonance. The first 9 entries are from scan#1 while the last 9 are from scan#2.

the maximum of the likelihood function decreases by a factor of $\exp(-\frac{1}{2})$. For completeness, the error matrix (the inverse of the second derivative matrix evaluated at the best fit parameter values) is given in table 6.7.

Since the value of the likelihood function does not provide a measure of the goodness of fit, Pearson's χ^2 test was applied. The χ^2 was calculated as:

$$\chi^2 = \sum_{j=1}^{N} \frac{(n_j^{obs} - \nu_j^{pred})^2}{\nu_j^{pred}} \tag{6.6}$$

where n_j^{obs} is the observed number of events at the j-th point and ν_j^{pred} is the number of events predicted by equation 6.3 assuming the best fit values of M_R, Γ_R, and A_R obtained from the likelihood fit. The χ^2 probability of the fits are summarized in table 6.6. The data and the fitted excitation curves are plotted in figures 6.7 and 6.8.

Resonance	M_R (MeV/c^2)	Γ_R (MeV)	A_R (eV)	χ^2/dof
χ_1 scan 1	$3510.473^{+0.061}_{-0.064}$	$0.88^{+0.20}_{-0.17}$	$1.29^{+0.14}_{-0.12}$	8.4/6
χ_1 scan 2	$3510.523^{+0.054}_{-0.053}$	$0.86^{+0.14}_{-0.12}$	$1.18^{+0.11}_{-0.10}$	9.5/4
χ_1 combined	$3510.506^{+0.040}_{-0.040}$	$0.86^{+0.11}_{-0.10}$	$1.22^{+0.08}_{-0.08}$	19.2/13
χ_2 scan 1	$3556.022^{+0.217}_{-0.185}$	$1.92^{+0.36}_{-0.37}$	$1.64^{+0.26}_{-0.23}$	4.1/6
χ_2 scan 2	$3556.024^{+0.078}_{-0.080}$	$2.06^{+0.25}_{-0.21}$	$1.69^{+0.12}_{-0.11}$	17.4/6
χ_2 combined	$3556.029^{+0.070}_{-0.071}$	$2.01^{+0.18}_{-0.16}$	$1.68^{+0.10}_{-0.10}$	21.6/15

Table 6.6: Results of the fits to the resonance curves for the $\chi_{1,2}$

Resonance	M_R,M_R	M_R,Γ_R	M_R,A_R	Γ_R,Γ_R	Γ_R,A_R	A_R,A_R
χ_1 scan 1	0.0039	-0.0014	-0.0006	0.0338	0.0174	0.0169
χ_1 scan 2	0.0028	0.0009	0.0015	0.0171	0.0086	0.0115
χ_1 combined	0.0016	0.0002	0.0005	0.0112	0.0056	0.0065
χ_2 scan 1	0.0415	0.0396	0.0296	0.1270	0.0739	0.0614
χ_2 scan 2	0.0062	-0.0012	0.0002	0.0517	0.0149	0.0131
χ_2 combined	0.0050	0.0006	0.0009	0.0303	0.0109	0.0010

Table 6.7: The error matrix for the fits to the resonance curves.

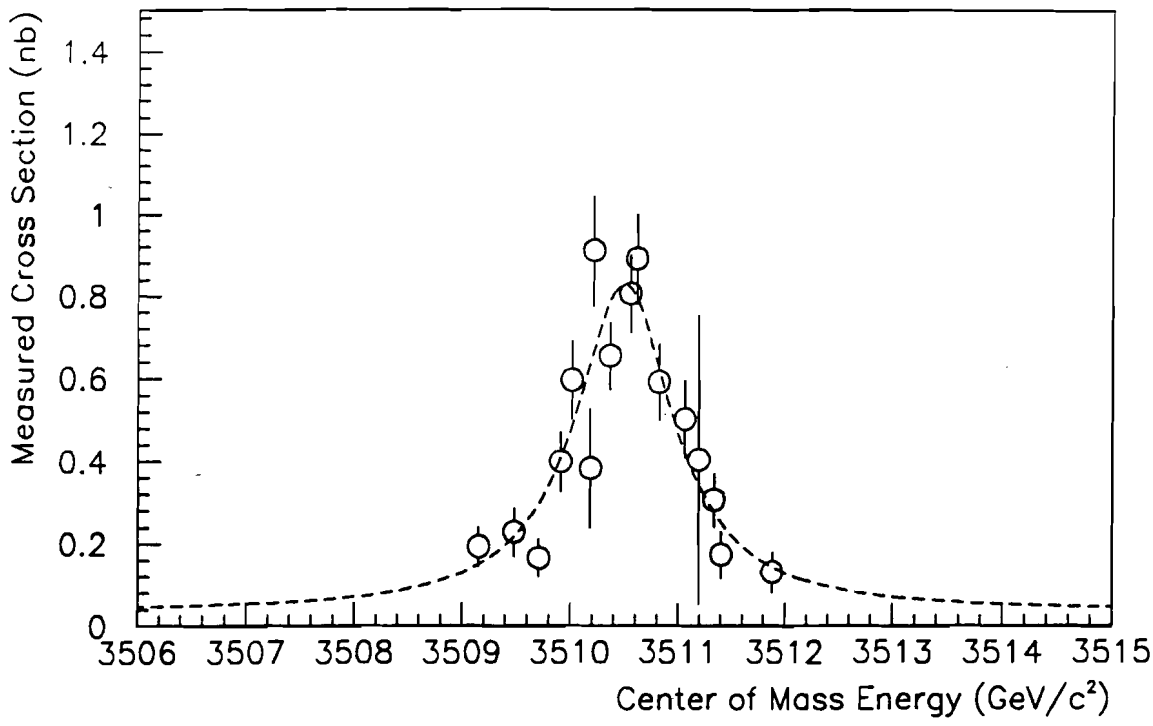

Figure 6.7: Measured cross section for the χ_1. The dashed line represents the best fit to the data.

The random errors for all the resonance parameters reported here are due only to $\chi_{1,2}$ event statistics. All other sources of error are treated as systematic even if they are associated with random variables. The systematic error in $\Gamma(R \to \bar{p}p) \times BR(R \to J/\psi\gamma) \times BR(J/\psi \to e^+e^-)$ is calculated by varying the values of ϵ, σ_{bckg}, and $(\int \mathcal{L}dt)_j$ one at a time by amounts equal to their r.m.s. errors, then refitting

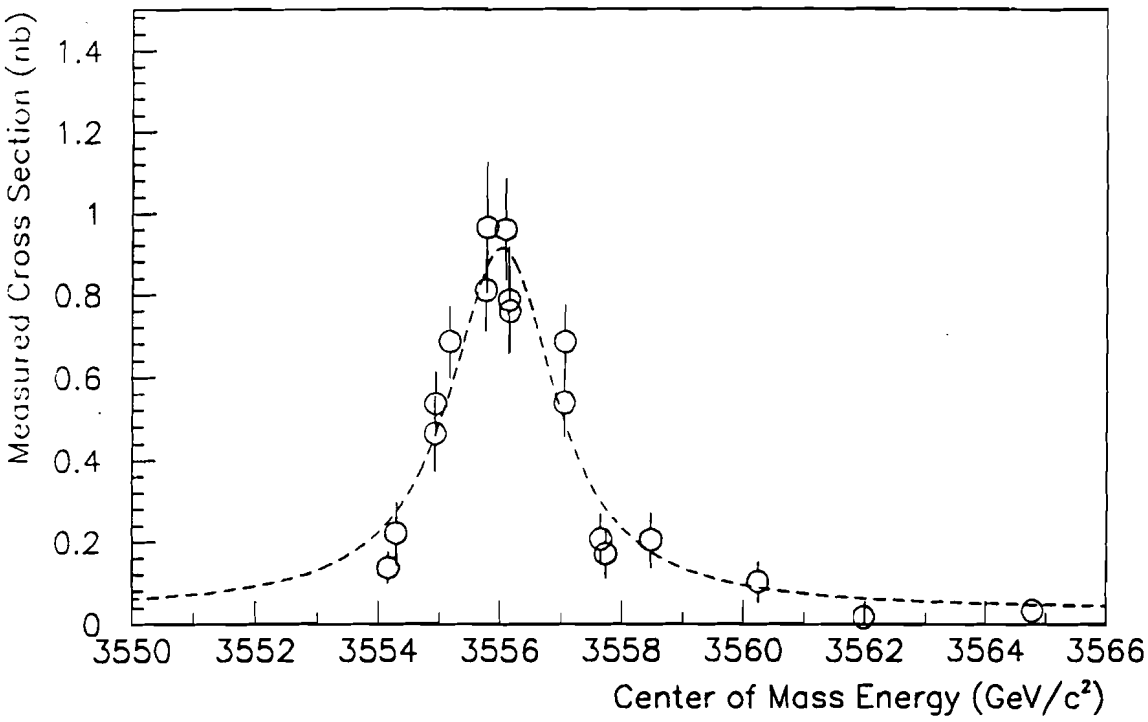

Figure 6.8: Measured cross section for the χ_2. The dashed line represents the best fit to the data.

the resonance and adding the resulting shifts in quadrature. The systematic error in the total width Γ_R is calculated in the same way as above except that one has to also include the errors in the beam width $\sigma(E_{beam_j})$. The systematic error in the mass depends only on our knowledge of the absolute beam energy scale (see discussion 2.1.2). The final results for the $\chi_{1,2}$ resonance parameters is summarized in the table 6.8.

Parameters	χ_1	χ_2
M_R (MeV/c^2)	$3510.51 \pm 0.04 \pm 0.12$	$3556.03 \pm 0.07 \pm 0.12$
Γ_R (MeV)	$0.86 \pm 0.11 \pm 0.08$	$2.01 \pm 0.17 \pm 0.07$
A_R (eV)	$1.22 \pm 0.08 \pm 0.13$	$1.68 \pm 0.10 \pm 0.12$

Table 6.8: Final results for $\chi_{1,2}$ resonance parameters. The first errors are statistical and the second are systematic.

Chapter 7

Conclusions

7.1 Branching Ratios and Partial Widths

The branching ratios $BR(R \to \bar{p}p)$ can be extracted from the measured branching ratio product (see table 6.8) and the branching ratios $BR(R \to J/\psi\gamma)$ and $BR(J/\psi \to e^+e^-)$. Similarly a precise estimate of the partial width $\Gamma(R \to J/\psi\gamma)$ can be obtained from the measured value of the total width and the $BR(R \to J/\psi\gamma)$. Using the appropriate combination of results reported in this dissertation and the previously published [49] values listed below:

- $BR(\chi_1 \to J/\psi\gamma) = 0.273 \pm 0.016$
- $BR(\chi_2 \to J/\psi\gamma) = 0.135 \pm 0.011$
- $BR(J/\psi \to e^+e^-) = 0.0627 \pm 0.0020$

one obtains the results tabulated in table 7.1 where the errors are from the uncertainties in the measured quantities plus the uncertainty in the published values given above.

Parameters	χ_1	χ_2
$BR(R \to \bar{p}p) \times 10^{-4}$	0.78 ± 0.21	0.91 ± 0.22
$\Gamma(R \to J/\psi\gamma)$ (keV)	240 ± 40	267 ± 33

Table 7.1: Calculated branching ratios and partial widths for the $\chi_{1,2}$.

7.1.1 Branching Ratio to $\bar{p}p$

At large momentum transfers, exclusive reactions can be analyzed in the framework of QCD by using the factorization theorem [50,51] which separates the dynamics of hard scattering quark gluon amplitudes (T_h) from process independent quark momentum distribution amplitudes. For the charmonium system where $Q^2 \sim 10\ GeV^2$, T_h can be evaluated perturbatively. Several authors [52,53,54] have applied this method to calculate the relative magnitude of the process $\bar{c}c \to \bar{p}p$ for various charmonium states. By using the quark distribution amplitude determined from an analysis of the process $J/\psi \to \bar{p}p$ [55] as a normalization, one can predict the branching ratio to $\bar{p}p$ for charmonium resonances. Predictions of the branching ratio $BR(\chi_2 \to \bar{p}p)$ by various authors are given in table 7.2 and are found to be in reasonable agreement with the experimental value reported here. No predictions using this method are avaliable for the χ_1.

Estimates of the branching ratio $BR(\chi \to \bar{p}p)$ have also been obtained by applying the quark-diquark model [56] of the nucleon to a perturbative QCD description of charmonium [57]. In the diquark model, the diquarks can have both scalar (J=0) and vector (J=1) components, this allows for a finite rate in the reaction $\eta_c \to \bar{p}p$ which is forbidden in massless QCD calculations [53]. In the recent calculation by Ane-

selmino et al., an estimate of $BR(\chi_1 \to \bar{p}p)$ is obtained by using the $BR(\chi_2 \to \bar{p}p)$ as input to fix the model parameters. Their result for the χ_1 is given in table 7.2. The diquark model suffers a great deal from a lack of high precision experimental data to fix the model parameters. The results presented in this dissertation should be helpful in the prediction of the $\bar{p}p$ branching ratio for other charmonium states using the diquark model.

State	Predicted Ref. [54]	Predicted Ref. [52]	Predicted Ref. [53]	Predicted Ref. [57]	Experimental[a]
χ_1	—	—	—	0.8	0.75 ± 0.15
χ_2	0.8-1.2	~ 1.0	2.0-2.1	—	0.87 ± 0.15
[a] Experimental result from table 7.1.					

Table 7.2: Comparison of predicted and measured $BR(\chi_{1,2} \to \bar{p}p)$ in units of 10^{-4}.

7.1.2 Radiative Widths

The radiative widths of the $\chi_{1,2}$ have been calculated within the context of potential models by many authors. The predictions for the radiative transitions in the charmonium system are very model dependent. The model dependance of the predicted radiative rates arises from the fact that the radiative transitions are, in general, sensitive to the details of the wave function at large inter-quark separations (r).

Perhaps the simplest result that one could investigate is the dipole approximation from atomic physics. In the dipole approximation, simple quantum mechanics leads

to the result

$$\Gamma(^3P_J \rightarrow ^3S_1 + \gamma) = \frac{4\alpha e_c^2 E_\gamma^3}{9} |\langle f|r|i\rangle|^2 \tag{7.1}$$

where the matrix element involves normalized radial wave functions and e_c is the electric charge of the charm quark in units $|e|$. From the above, one might expect that the ratio of the radiative width to E_γ^3 to be roughly constant for both the χ_1 and χ_2. Using the results from table 7.1 for the χ_1 and χ_2 and the published results [49] for the χ_0 one finds the expected scaling:

$$(\Gamma_\gamma/E_\gamma^3) \times 10^9 = 2.77 \pm 1.70 \quad for\ \chi_0$$

$$(\Gamma_\gamma/E_\gamma^3) \times 10^9 = 4.08 \pm 0.70 \quad for\ \chi_1$$

$$(\Gamma_\gamma/E_\gamma^3) \times 10^9 = 3.36 \pm 0.42 \quad for\ \chi_2$$

Predictions of the radiative widths for charmonium have been calculated using the Cornell Model (see chapter 1). The calculation by Eichten et al. [7] includes the effect of the $\bar{c}c$ system coupling to virtual decay channels (coupled channel effects) while a more recent effort by McClary and Byers [13] extends the calculation to include relativistic corrections to order v^2/c^2. The relativistic corrections to the Cornell Model are obtained by constructing a Breit-Fermi Hamiltonian that contains correction terms to order v^2/c^2. In the non-relativistic limit, the Breit-Fermi Hamiltonian used reduces to the one gluon exchange plus linear confinement form of the Cornell Model. The results of this calculation are detailed in table 7.3.

The results from table 7.3 show that the observed radiative widths can be completely explained by the Cornell Model when relativistic and coupled channel effects

State	Nonrel.[a] rates (keV)	Rel.[b] rates (keV)	CC[c] and Rel. rates (keV)	κ_c [d] corrections (keV)	Experimental[e] values (keV)
χ_1	250	270	240	1-0.11κ_c	240 ± 40
χ_2	362	347	305	1+0.12κ_c	267 ± 30

[a] Nonrelativistic rate.
[b] Rate with relativistic corrections.
[c] Rate with relativistic and coupled channel corrections.
[d] First order correction due to anomalous magnetic moment of the charm quark.
[e] Experimental result from table 7.1.

Table 7.3: $\chi_{1,2}$ E1 transition rates calculated from Cornell Model.

are included. These results suggest that the anomalous magnetic moment of the charm quark (κ_c) should be small. A small κ_c is also consistent with the observed M1 decay rate of $\psi' \to \chi_J + \gamma$ which is very sensitive to κ_c [14,15].

7.2 Production Helicities

As discussed in chapter 1, only the χ_2 angular distribution is sensitive to the formation helicity. Helicity conservation in massless perturbative QCD [55,58,59] forbids helicity 0 (B_0) in the annihilation process. The basic assumption of massless QCD requires that the proton consist of massless collinear quarks. This approximation is not good in the case of charmonium where the mass of the proton is of the same order as the mass of charmonium. Examples of violations of the QCD helicity selection rule in charmonium include observations of $\eta_c \to \bar{p}p$ and ${}^1P_1 \to \bar{p}p$, which are both forbidden by massless QCD.

A straightforward way of taking the non-zero proton mass into account is a

calculation using the effective Lagrangian approach [60], which predicts $B_0^2/B_1^2 = \frac{64}{27}m_p^2/m_\chi^2$ or $B_0^2 = 0.16$. Another prediction without the $m_q = 0$ assumption comes from a QCD based calculation, which uses the quark-diquark model of the proton [61,62]. It predicts $B_0^2 = 0.16$ in the scalar diquark limit and approximately 0.08 in the vector diquark limit.

The measured value for the helicity 0 amplitude ($B_0^2 = 0.02^{+0.13}_{-0.02}$) is consistent with the massless QCD prediction as well as the models incorporating non-zero quark masses.

7.3 Multipole Amplitudes

As discussed in chapter 1, the nonrelativistic transition operator for the radiative decay is almost a pure E1 operator which gives rise to the characteristic electric dipole angular distribution. For a simple multipole transition, the angular distribution depends on initial and final angular momentum states and is independent of the particular potential used. When first order relativistic corrections (order E_γ/m_c) to the transition operator are introduced, the transition operator becomes a coherent mixture of E1, M2, and E3 amplitudes [63]. In general, the relative strengths of these M2 and E3 amplitudes depend on the particular potential used.

In a recent relativistic (to order E_γ/m_c) calculation by Sebastian, Grotch, and Ridener [64], it has been found that if one assumes that there is no D-state mixing for the J/ψ then the multipole amplitudes for the process $\chi_{1,2} \to J/\psi + \gamma \to e^+e^- + \gamma$ become independent of the particular potential used. The M2 amplitudes depend

on the mass of the charm quark (m_c), the anomalous magnetic moment of the charm quark (κ_c) and the energy of the radiative photon (E_γ):

$$a_2(\chi_1) = -\frac{E_\gamma}{4m_c}(1+\kappa_c) \tag{7.2}$$

and

$$a_2(\chi_2) = -\frac{3}{\sqrt{5}}\frac{E_\gamma}{4m_c}(1+\kappa_c). \tag{7.3}$$

If one assumes that $\kappa_c = 0$ and takes the charm quark mass to be $m_c = 1.5 \pm 0.3\ GeV$ then one can compare the potential independent predictions for the amplitudes with the measured values (see table 7.4). The calculation by Sebastian et al. also finds that the E3 amplitude for the χ_2 vanishes in the limit of no D-state mixing for the J/ψ [64], so $a_3(\chi_2) = 0$. Another estimate of the E3 amplitude has been made by M.G. Olsson et al. [18] where they assume that one of the charm quarks in the χ_2 emits the radiative photon while the other is a spectator. Under this assumption known as the "single-quark radiation" hypothesis, a non-zero E3 amplitude is forbidden.

Amplitude	Measured	Predicted
$a_2(\chi_1)$	-0.14 ± 0.06	-0.07 ± 0.01
$a_2(\chi_2)$	-0.15 ± 0.06	-0.10 ± 0.02
$a_3(\chi_2)$	0.00 ± 0.05	0.0

Table 7.4: Comparison between measured and predicted multipole amplitudes. The error on the predicted amplitudes comes from the uncertainty in the charm quark mass.

7.3.1 The Charm Quark Magnetic Moment

As discussed in the section above, the quadrupole amplitude a_2 for both the χ_1 and χ_2 have been calculated to first order in E_γ/m_c and are independent of the potential. Equations 7.2 and 7.3 are solved for the anomalous magnetic moment κ_c of the charm quark:

$$\kappa_c(\chi_1) = -\left(1 + \frac{4m_c}{E_\gamma} a_2(\chi_1)\right) \tag{7.4}$$

and

$$\kappa_c(\chi_2) = -\left(1 + \frac{\sqrt{5}}{3}\frac{4m_c}{E_\gamma} a_2(\chi_2)\right). \tag{7.5}$$

Although κ_c is expected to be small, it has been speculated that nonperturbative QCD effects [65] may lead to large values. So if we use the measured results from table 5.6 and $m_c = 1.5 \pm 0.3\ GeV$ one obtains:

$$\kappa_c(\chi_1) = 1.05 \pm 0.87 \pm 0.41 \tag{7.6}$$

and,

$$\kappa_c(\chi_2) = 0.46 \pm 0.58 \pm 0.29 \tag{7.7}$$

where the first error is statistical and the second is due to the uncertainty of m_c. A large value of the anomalous magnetic moment would have a significant impact on the theoretical predictions for the radiative widths [64] of other charmonium resonances.

7.4 Hadronic Widths

The hadronic width of the $\chi_{1,2}$ has been calculated to lowest order [66] in α_s and to first order in α_s for the χ_2 in a recent paper by Kwong et al. [67]. These widths are given by

$$\Gamma(\chi_1 \to q\bar{q}g) \simeq \left(\frac{24}{9\pi}\alpha_s^3|R_p'(0)|^2/m_c^4\right) \times \ln\left(m_c\langle r\rangle\right) \tag{7.8}$$

and

$$\Gamma(\chi_2 \to gg) \simeq \left(\frac{8}{5}\alpha_s^2|R_p'(0)|^2/m_c^4\right) \times (1 - [2.2\alpha_s/\pi]) \tag{7.9}$$

where $\alpha_s \equiv \alpha_s(m_c)$ is the running QCD coupling constant, m_c is the mass of the charm quark ($m_c = 1.5\ GeV/c^2$), $\langle r\rangle$ is the confinement radius ($\langle r\rangle = 3.17\ GeV^{-1}$), and $|R_p'(0)|$ is the first derivative of the radial wave function at the origin of the P-wave $\bar{c}c$ system. The first order correction $(1 - [2.2\alpha_s/\pi])$ in equation 7.9 is rather large (about 20%) suggesting that further substantial corrections may be required. However, it is a useful exercise to compare the results of equations 7.8 and 7.9 to experiment.

The radial wave function has been estimated by solving the Schrödinger equation with a variety of phenomenological central potentials [68]. Although the value of $|R_p'(0)|^2$ is sensitive to the exact form of the potential, most reasonable potentials (i.e. those that qualitatively reproduce the observed charmonium spectrum) give values between 0.057 and 0.11 GeV^5. If one uses this range for $|R_p'(0)|$ and takes $\alpha_s = 0.32$ (see section 7.4.1), then the hadronic widths can be computed and are given in table 7.5. The experimental values for the hadronic widths can be estimated

as:

$$\Gamma_{hadronic} \simeq \Gamma_R - \Gamma(R \rightarrow J/\psi + \gamma) = \Gamma_R(1 - BR(R \rightarrow J/\psi + \gamma)) \qquad (7.10)$$

where one can use the known values of the radiative decay branching ratios given in table 7.1 and the measured total widths (Γ_R) from table 6.8. A comparison between the measured and predicted hadronic widths is made in table 7.5. If the uncertainties in the mass of the charm quark could be reduced, then the measurements of the hadronic widths could be a sensitive test to differentiate among the various phenomenological models.

State	Measured MeV	Predicted MeV
χ_1	0.64 ± 0.11	0.49 *to* 0.94
χ_2	1.71 ± 0.21	1.43 *to* 2.76

Table 7.5: Comparison between measured and predicted hadronic widths for the $\chi_{1,2}$.

7.4.1 Determination of α_s

For the χ_2, the annihilation rate to two photons has been calculated by Kwong et al. [67] to first order and is given by

$$\Gamma(\chi_2 \rightarrow \gamma\gamma) \simeq \left(\frac{36}{5} e_c^4 \alpha^2 |R_p'(0)|^2 / m_c^4\right) \times (1 - [16\alpha_s/3\pi]) \qquad (7.11)$$

where e_c is the electric charge of the charm quark in units of $|e|$. By taking the ratio of equations 7.9 and 7.11, the dependence of the derivative at the origin of the radial wave function drops out (to first order). If one uses the measured value for

the χ_2 to hadrons from above and the value of χ_2 to $\gamma\gamma$ from a recent determination by the E760 collaboration [40], then the ratio of equations 7.9 and 7.11 can be used to determine the value of $\alpha_s(m_c)$. The value of $\alpha_s(m_c)$ obtained in this way is:

$$\alpha_s(m_c) = 0.37^{+0.04}_{-0.03}. \tag{7.12}$$

This result can be compared with the value obtained by "running" down the value of α_s at the Z-pole to that at the charm quark mass m_c. The world average value for $\alpha_s(m_Z) = 0.1134 \pm 0.0035$; by "running" this value down to the charm quark mass using the prescription found in the particle data book [49], one obtains the value

$$\alpha_s(m_c) = 0.32^{+0.01}_{-0.03} \tag{7.13}$$

which agrees reasonably well with the value obtained from the E760 measurements considering the uncertainties in equations 7.9 and 7.11.

7.5 Final Comments

The results presented in this dissertation represent a substantial improvement over previous results (see section 1.1). The error in the masses M_R of the $\chi_{1,2}$ have been reduced by a factor of 2. The error in the total width Γ_R for the χ_2 has been improved by a factor of 4 while Γ_R for the χ_1 has been measured for the first time. The results for the angular distributions represent a factor of 3 improvement over the best previous results for the decay multipole amplitudes and provide the first statistically significant measurement of $\bar{p}p \rightarrow \chi_2$ formation helicity.

Precision measurements like the ones presented in this dissertation may yet allow the charmonium system to fulfill its promise as the test-bed of QCD. I wish good fortune to the future E760 collaborators and hope that they will be able to further improve on the results presented here.

Bibliography

[1] M. Oreglia et al. *Phys. Rev.*, D25:2259, 1982.

[2] Baglin et al. *Phys. Let.*, B172:455, 1986.

[3] V.A. Novilov et al. *Phys. Rep.*, C41:1, 1977.

[4] L. Bugge. Report 86-20, Dept. of Physics, University of Oslo, 1986.

[5] W. Kwong et al. *Ann. Rev. Nucl. Part. Sci.*, 37:325, 1987.

[6] C. Quigg. *Acta Physica Polonica*, B15:53, 1984.

[7] E. Eichten et al. *Phys. Rev.*, D21:203, 1980.

[8] C. Quigg and J.L. Rosner. *Phys. Rep.*, 56:167, 1979.

[9] W. Buchmüller and S.-H.H Tye. *Phys. Rev.*, D24:132, 1981.

[10] C.O. Bib et al. *Phys. Rev.*, D37:735, 1988.

[11] K.J. Sebastian. *Phys. Rev.*, D26:2295, 1982.

[12] P. Moxhay and J.L. Rosner. *Phys. Rev.*, D28:1132, 1983.

[13] R. McClary and N. Byers. *Phys. Rev.*, D28:1692, 1983.

[14] S.N. Gupta et al. *Phys. Rev.*, D39:974, 1989.

[15] X. Zhang. *Phys. Rev.*, D30:1606, 1991.

[16] Y. Ding et al. *Phys. Rev.*, D44:3562, 1991.

[17] M. Jacob and G.C. Wick. *Annals of Physics*, 7:404, 1959.

[18] M.G. Olsson et al. *Phys. Rev.*, D31:1759, 1985.

[19] M.G. Olsson et al. *Phys. Rev.*, D34:2043, 1986.

[20] F.L. Ridener, Jr. et al. *Phys. Rev.*, D45:3173, 1992.

[21] M.E. Rose. *Elementary Theory of Angular Momentum.* Wiley, New York, 1957.

[22] A.D. Martin and T.D. Spearman. *Elementary Particle Theory.* North-Holland, Amsterdam, 1970.

[23] Design Report: Tevatron 1 Project, Fermi National Accelerator Laboratory. Batavia, IL, (unplublished), September 1984.

[24] CERN Accelerator School. *Antiprotons for Colliding Beam Facilities, October 1983*, Cern Report CERN84-15, 1984.

[25] E-760 collaboration. Mearsurement of the J/ψ and ψ' resonance parameters in $\bar{p}p$ annihilation. To be published.

[26] V. Bharadwaj. *Preceedings of the European Partical Accelerator Conference.* World Scientific Publishing Co., Singapore, 1989.

[27] E.D. Courant and H.S. Snyder. *Annals of Physics*, 3:1, 1958.

[28] D. Boussard. Cern Accelerator School 1985. *Advanced Accelerator Physics*, CERN 87-03 vol. II:416–452, 1987.

[29] T. Bagwell et al. Fermilab Technical Memo 1254, Fermi National Accelerator Laboratory, 1984.

[30] E.D. Courant and H.S. Snyder. *Ann. Phys. (N.Y.)*, 3:1, 1958.

[31] M. Macri. Gas Jet Targets. *CERN Accelerator Summer School 1983*, CERN 85-15, 1985.

[32] M.M. Block and R.N. Cahn. *Review of Modern Physics*, 57(No.2), 1985.

[33] C. Biino et al. *Nucl. Instrum Methods*, A271:417, 1988.

[34] R. Calabrese et al. *Nucl. Instrum Methods*, A277:116, 1989.

[35] G. Barisone et al. Report A.E./89-6, I.N.F.N., 1989.

[36] C. Biino et al. *Nucl. Instrum Methods*, A317:135, 1992.

[37] L. Bartosek et al. *Nucl. Instrum Methods*, A301:47, 1991.

[38] M.A. Hasan et al. *Nucl. Instrum Methods*, A295:73, 1990.

[39] A.V. Inyakin et al. *Nucl. Instrum Methods*, 215:103, 1983.

[40] T.A. Armstrong et al. Measurement of the $\gamma\gamma$ partial width of the χ_2 charmonium resonance. *Phys. Rev. Lett.*, submitted 1992.

[41] G.A. Akopdjanov et al. *Nucl. Instrum Methods*, A140:441, 1977.

[42] R. Ray et al. *Nucl. Instr. and Meth.*, A307:254, 1991.

[43] I. Gaines et al. *Computer Physics Communications*, 45:323, 1987.

[44] C. Gay et al. *IEEE Trans. on Nucl. Sci.*, 34:870, 1987.

[45] S. Hansen et al. *IEEE Trans. on Nucl. Sci.*, 34:1003, 1987.

[46] F. James and M. Roos. CERN Computer Center Program Library MINUIT, D-506, CERN, 1992.

[47] The Particle Data Group. *Phys. Rev.*, D48:III.38–39, 1992.

[48] T.A. Armstrong et al. *Phys. Rev. Lett.*, 69:2337, 1992.

[49] The Particle Data Group. *Phys. Rev.*, D48, 1992.

[50] A. Duncan and A.H. Mueller. *Phys. Rev.*, D21:1636, 1980.

[51] S.J. Brodsky and G.P. Lepage. *Phys. Rev.*, D22:2157, 1980.

[52] V.L. Chernyak and I.R. Zhitnitsky. *Nucl. Phys.*, B52:246, 1984.

[53] A. Andrikopoulou. *Z. Phys.*, C22:63, 1984.

[54] E.L. Berger et al. QCD Prdictions for Charmonium Production in $\bar{p}p$ Collisions. *Preceedings of the VIIth European Symposium on Antiproton Interactions*, Durham, UK, July 9-13, 1984.

[55] S.J. Brodsky and G.P. Lepage. *Phys. Rev.*, D24:2848, 1981.

[56] M. Anselmino et al., editor. *Preceedings of the Diquark Workshop, Torino, Italy, 1988.* Wrold Scientific, Singapore, 1989.

[57] M. Anselmino. *Phys. Rev.*. D44:1438, 1991.

[58] A. Andrikopoulou. *Z. Phys.*, C22:63, 1984.

[59] V.L. Chernıak et al. *Z. Phys.*, C42:583, 1989.

[60] W. Buchmüller. Production and Decays of Quarkonia in $p\bar{p}$ Collisions. *Physics with Antiprotons at LEAR in the Acol Era*, Tignes:327, 1985.

[61] M. Anselmino et al. *Phys. Rev.*, D44:1438, 1991.

[62] M. Anselmino et al. *Phys. Rev.*, D45:4340, 1992.

[63] M.A. Doncheski et al. *Phys. Rev.*, D42:2293, 1990.

[64] K.J. Sebastian et al. *Phys. Rev.*, D45:3163, 1992.

[65] D.A. Geffen and W.J. Wilson. *Phys. Rev. Lett.*, 44:370, 1980.

[66] R. Barbieri et al. *Nucl. Phys.*, B162:61, 1981.

[67] W. Kwong et al. *Phys. Rev.*, D37:3210, 1988.

[68] M.G. Olsson et al. *Phys. Rev.*, D31:81, 1985.